FROM: AFIT/CI

11 July 1989

SUBJECT: Review of Thesis/Dissertation for Public Release

TO: PA

1. Request you review the attached for public release prior to being sent to DTIC.

2. Reply by indorsement to CI NLT _____.

ERNEST A. HAYGOOD, 1st Lt, USAF
Executive Officer
Civilian Institution Programs

1 Atch
THESIS 89-064
ROBERTS

1st Ind, AFIT/PA

0 8 FEB 1990

TO: CI

Approved/~~Disapproved~~ for public release.
Log Number: 89-10-115

HARRIET D. MOULTRIE, Capt, USAF
Director, Office of Public Affairs

AD-A218 285

# REPORT DOCUMENTATION PAGE

Form Approved
OMB No. 0704-0188

| 1a. REPORT SECURITY CLASSIFICATION UNCLASSIFIED | 1b. RESTRICTIVE MARKINGS NONE |
|---|---|
| 2a. SECURITY CLASSIFICATION AUTHORITY | 3. DISTRIBUTION / AVAILABILITY OF REPORT |
| 2b. DECLASSIFICATION / DOWNGRADING SCHEDULE | APPROVED FOR PUBLIC RELEASE; DISTRIBUTION UNLIMITED. |

| 4. PERFORMING ORGANIZATION REPORT NUMBER(S) | 5. MONITORING ORGANIZATION REPORT NUMBER(S) AFIT/CI/CIA-89-064 |
|---|---|

| 6a. NAME OF PERFORMING ORGANIZATION AFIT STUDENT AT UTAH STATE UNIVERSITY | 6b. OFFICE SYMBOL (If applicable) | 7a. NAME OF MONITORING ORGANIZATION AFIT/CIA |
|---|---|---|
| 6c. ADDRESS (City, State, and ZIP Code) | | 7b. ADDRESS (City, State, and ZIP Code) Wright-Patterson AFB OH 45433-6583 |

| 8a. NAME OF FUNDING / SPONSORING ORGANIZATION | 8b. OFFICE SYMBOL (If applicable) | 9. PROCUREMENT INSTRUMENT IDENTIFICATION NUMBER |
|---|---|---|

| 8c. ADDRESS (City, State, and ZIP Code) | 10. SOURCE OF FUNDING NUMBERS | | | |
|---|---|---|---|---|
| | PROGRAM ELEMENT NO. | PROJECT NO. | TASK NO | WORK UNIT ACCESSION NO. |
| | | | | |

11. TITLE (Include Security Classification) (UNCLASSIFIED)
Measurements of the Interaction of High-Voltage Biassed Conductors with the Ionosphere

12. PERSONAL AUTHOR(S)
Jon A. Roberts

| 13a. TYPE OF REPORT THESIS/DISSERTATION | 13b. TIME COVERED FROM _____ TO _____ | 14. DATE OF REPORT (Year, Month, Day) 1989 | 15. PAGE COUNT 110 |
|---|---|---|---|

16. SUPPLEMENTARY NOTATION APPROVED FOR PUBLIC RELEASE IAW AFR 190-1
ERNEST A. HAYGOOD, 1st Lt, USAF
Executive Officer, Civilian Institution Programs

| 17. COSATI CODES | | | 18. SUBJECT TERMS (Continue on reverse if necessary and identify by block number) |
|---|---|---|---|
| FIELD | GROUP | SUB-GROUP | |
| | | | |
| | | | |

19. ABSTRACT (Continue on reverse if necessary and identify by block number)

| 20. DISTRIBUTION / AVAILABILITY OF ABSTRACT ☒ UNCLASSIFIED/UNLIMITED ☐ SAME AS RPT. ☐ DTIC USERS | 21. ABSTRACT SECURITY CLASSIFICATION UNCLASSIFIED |
|---|---|
| 22a. NAME OF RESPONSIBLE INDIVIDUAL ERNEST A. HAYGOOD, 1st Lt, USAF | 22b. TELEPHONE (Include Area Code) (513) 255-2259  22c. OFFICE SYMBOL AFIT/CI |

DD Form 1473, JUN 86          Previous editions are obsolete.          SECURITY CLASSIFICATION OF THIS PAGE

AFIT/CI "OVERPRINT"

# ABSTRACT

Measurements of the Interaction of High-Voltage Biassed

Conductors with the Ionosphere

by

Jon A. Roberts, Captain, USAF

Master of Science

Utah State University, 1989

Major Professor: Dr. W. John Raitt
Department: Soil Science and Biometeorology

The Space Power Experiments Aboard Rockets program was developed to study the interaction of high-voltage biassed conductors with the low earth orbit environment. The experiment utilized two spherical conductors, which were biassed to potentials as high as 45,000 volts, and the steady-state current-voltage characteristics were analyzed. The spheres were flown in three different orientations with respect to the earth's magnetic field. At times, only one sphere was biassed so that the current collection characteristics of a single spherical conductor could be studied. At other times, both spheres were biassed to approximately the same voltage, or to greatly differing voltages so that the interactions between charge sheaths could be studied. The failure of the plasma contactor allowed the rocket body to charge to up to several kilovolts negative during sphere biassing, resulting in the establishment of an unplanned positive ion sheath around the rocket body, thereby complicating the interpretation of the current-voltage characteristics of the spheres. Specifically, the following areas were studied: current-voltage characteristics with respect to altitude, magnetic field orientation, and attitude control

system activity. In addition, the characteristics of a possible volume breakdown were analyzed, along with the charging of the rocket body and interactions between charge sheaths. Finally, these results were compared with analytical and numerical models.

(120 pages)

# REFERENCES

Banks, P. M. and G. Kockarts, Aeronomy (Parts A and B), 785 pp, Academic Press, New York, 1973.

Bauer, S. J., Physics of Planetary Ionospheres, 230 pp, Springer-Verlag, New York, 1973.

Beard, D. B. and F. S. Johnson, Charge and magnetic field interaction with satellites, J. Geophys. Res., 65, 1-7, 1960.

Beard, D. B., and F. S. Johnson, Ionospheric limitations on attainable satellite potential, J. Geophys. Res., 66, 4113-4122, 1961.

Bunshah, R. F., The history of electron beam technology, in Introduction to Electron Beam Technology, edited by R. Bakish, pp 1-20, John Wiley and Sons, New York, 1962.

Cauffman, D. P. and N. C. Maynard, Model of the effect of the satellite photosheath on a double floating probe system, J. Geophys. Res., 79, 2427-2438, 1974.

Coffey, H. E., Geomagnetic and solar data, J. Geophys. Res., 93, pp 1028, 2016, and 2768, 1988.

DeForest, S. E., Spacecraft charging at synchronous orbit, J. Geophys. Res., 77, 651-659, 1972.

Dietz, L. A. and J. C. Sheffield, Secondary electron emission induced by 5-30 keV monatomic ions striking thin oxide films, J. Appl. Phys., 46, 4361-4370, 1975.

Dunbar, W. G., Large space systems technology electronics-data and power distribution, in Large Space Systems Technology-1979, NASA CP-2118, pp 423-442, 1980.

Feuerbacher B. and B. Fitton, Experimental investigation of photoemission from satellite surface materials, J. Appl. Phys., 43, 1563-1572, 1972.

Finke, R. C., I. T. Myers, F. F. Terdan, and N. J. Stevens, Power management and control for space systems, in Future Orbital Power Systems Technology Requirements, NASA CP-2058, pp 195-207, 1978.

Garrett, H. B., Spacecraft charging: a review, Prog. Astronaut. Aeronaut., 71, 167-226, 1980.

Gussenhoven, M. S. and E. G. Mullen, Geosynchronous environment for severe spacecraft charging, J. Space. Rockets, 20, 26-31, 1983.

Halliday, D., and R. Resnick, Fundamentals of Physics, 827 pp, John Wiley and Sons, New York, 1974.

Hedin, A. E., MSIS-86 thermospheric model, J. Geophys. Res., 92, 4649-4662, 1987.

Hok, G., H. S. Sicinski, and N. W. Spencer, Temperature and electron density measurements in the ionosphere by a Langmuir probe, in Scientific Uses of Earth Satellites, edited by J. A. Van Allen, pp 263-267, Univ. of Michigan Press, Ann Arbor, 1956.

Katz, I., J. J. Cassidy, M. J. Mandel, G. W. Schnuelle, P. G. Steen, and J. C. Roche, The capabilities of the NASA charging analyzer program, in Spacecraft Charging Technology-1978, NASA CP-2071, AFGL-TR-79-0082, pp 101-108, 1979.

Katz, I., M. J. Mandell, G. W. Schnuelle, D. E. Parks, and P. G. Steen, Plasma collection by high voltage spacecraft at low earth orbit, J. Space. Rockets, 18, 79-82, 1981.

Katz, I. and D. L. Cooke, Preliminary documentation for the POLAR code, AFGL-TR-83-0194, 256pp, Air Force Geophys. Lab., Bedford, Mass., 1984.

Katz, I., G. A. Jongward, V. A. Davis, M. J. Mandell, R. A. Kuharski, J. R. Lilley, Jr., W. J. Raitt, D. L. Cooke, R. B. Torbet, G. Larson, and D. Rau, Structure of the bipolar plasma sheath generated by SPEAR-1, J. Geophys. Res., 94, 1450-1458, 1989.

Kawashima, N., S. Sasaki, K. Oyama, K. Akai, and Y. Nakai, Floating potential and return current measurements in a rocket-borne electron beam experiment, Geophys. Res. Lett., 9, 1061-1063, 1982.

Knott, K., The equilibrium potential of a magnetospheric satellite in an eclipse situation, Planet. Space Sci., 20, 1137-1146, 1972.

Laframboise, J. G. and L. W. Parker, Spacecraft charging in the auroral plasma: progress toward understanding the physical effects involved, in The Aerospace Environment at High Altitudes and its Implications for Spacecraft Charging and Communications, AGARD Conference Proceedings #406, pp 13.1-13.10, 1987.

Langmuir, I., The effect of space charge and residual gases on thermionic currents in high vacuum, Phys. Rev., 2, 450-486, 1913.

Langmuir, I. and K. Blodgett, Currents limited by space charge between coaxial cylinders, Phys. Rev., 22, 347-356, 1923.

Langmuir, I., and K. Blodgett, Currents limited by space charge between concentric spheres, Phys. Rev., 23, 49-59, 1924.

Leonard, L. H., Electron gun design, in Introduction to Electron Beam Technology, edited by R. Bakish, pp 70-95, John Wiley and Sons, New York, 1962.

Linson, L. M., Current-voltage characteristics of an electron-emitting satellite in the ionosphere, J. Geophys. Res., 74, 2368-2375, 1969.

McPherson, D. A., and W. R. Schober, Spacecraft charging at high altitudes: the SCATHA satellite program, Prog. Astronaut. Aeronaut., 47, 15-30, 1976.

Montgomery, M. D., J. R. Asbridge, S. J. Bane, and E. W. Hones, Jr., Low energy measurements and spacecraft potential: Vela 5 and Vela 6, in Photon and Particle Interactions with Surfaces in Space, D. Reidel, Dordrecht, Holland, 1973.

Mott-Smith, H. M., and I. Langmuir, The theory of collectors in gaseous discharges, Phys. Rev., 28, 727-763, 1926.

Mullen, E. G., M. S. Gussenhoven, D. A. Hardy, T. A. Aggson, and B. G. Ledley, SCATHA survey of high-level spacecraft charging in sunlight, J. Geophys. Res., 91, 1474-1490, 1986.

Olsen, R. C., Modification of spacecraft potentials by thermal electron emission on ATS-5, J. Space. Rockets, 18, 527-532, 1981.

Olsen, R. C., A threshold effect for spacecraft charging, J. Geophys. Res., 88, 493-503, 1983.

Olsen, R. C., Experiments in charge control at geosynchronous orbit - ATS-5 and ATS-6, J. Space. Rockets, 22, 254-264, 1985.

Olsen, R. C. and C. K. Purvis, Observations of charging dynamics, J. Geophys. Res., 88, 5657-5667, 1983.

Parker, L. W. and B. L. Murphy, Potential buildup on an electron emitting ionospheric satellite, J. Geophys. Res., 72, 1631-1636, 1967.

Parks, D. E. and I. Katz, Charging of a large object in low earth polar orbit, in Spacecraft Charging Technology-1980, NASA-CP-2182, AFGL-TR-81-0270, pp 979-986, 1981.

Purvis, C. K. and R. O. Bartlett, Active control of spacecraft charging, Prog. Astronaut. Aeronaut., 71, 299-317, 1980.

Raitt, W. J., SPEAR-1: Space Power Experiments Aboard Rockets, Final Report to the Defense Nuclear Agency, Utah State University, Center for Atmospheric and Space Sciences, 95pp., 1988.

Raitt, W. J., J. V. Eccles, N. B. Myers, D. C. Thompson, P. M. Banks, P. R. Williamson, R. I. Bush, J. Hawkins, S. Sasaki, K. I. Oyama, N. Kawashima, and W. F. Sharp, Active vehicle charging measurements in sounding rocket and space shuttle orbiter environments at low earth (LEO) altitude, in The Aerospace Environment at High Altitudes and its Implications for Spacecraft Charging and Communications, AGARD Conference Proceedings #406, pp 9.1-9.16, 1987.

Rawer, K., S. Ramakrishnan, and D. Bilitza, International reference ionosphere 1978, U.R.S.I. Brussels and World Data Center, Report UAG-82, Boulder, Colo., 1981.

Reagan, J. B., R. W. Nightingale, E. E. Gaines, R. E. Meyerott, and W. L. Imhof, Role of energetic particles in charging/discharging of spacecraft dielectrics, in Spacecraft Charging Technology-1980, NASA-CP-2182, AFGL-TR-81-0270, pp 74-82, 1981.

Redhead, P. A., The magnetron gauge: a cold cathode vacuum gauge, Canadian J. Phys., 37, 1260-1271, 1959.

Richmond, A. D., Thermospheric dynamics and electrodynamics, in <u>Solar-Terrestrial Physics</u>, edited by R. L. Carovillano and J. M. Forbes, pp 523-607, D. Reidel, Dordrecht, Holland, 1982.

Roche, J. C., and C. K. Purvis, Comparison of NASCAP predictions with experimental data, in <u>Spacecraft Charging Technology, 1978</u>, NASA CP-2071, AFGL-TR-79-0082, 144-151, 1979.

Sasaki, S., K. I. Oyama, N. Kawashima, Y. Watanabe, T. Obayashi, W. J. Raitt, A. B. White, P. M. Banks, P. R. Williamson, W. F. Sharp, T. Yokota, and K. Hirao, Results from a series of tethered rocket experiments, <u>J. Space. Rockets</u>, <u>24</u>, 444-453, 1987.

Thiemann, I., R. W. Schunk, N. Singh, R. Grard, GIOTTO spacecraft charging due to impact generated plasma in the presence of dielectric materials, in <u>The Aerospace Environment at High Altitudes and its Implications for Spacecraft Charging and Communications</u>, AGARD Conference Proceedings #406, pp 11.1-11.7, 1987.

Whipple, E. C., Observation of photoelectrons and secondary electrons reflected from a potential barrier in the vicinity of ATS-6, <u>J. Geophys. Res.</u>, <u>81</u>, 715-719, 1976.

Whipple, E. C., Potential of surfaces in space, <u>Rep. Prog. Phys.</u>, <u>44</u>, 74-1250, 1981.

Winckler, J. R., The application of artificial electron beams to magnetospheric research, <u>Rev. Geophys. Space Phys.</u>, <u>18</u>, 659-682, 1980.

MEASUREMENTS OF THE INTERACTION OF HIGH-VOLTAGE

BIASSED CONDUCTORS WITH THE IONOSPHERE

by

Jon Alan Roberts

A thesis submitted in partial fulfillment
of the requirements for the degree

of

MASTER OF SCIENCE

in

Soil Science and Biometeorology

Approved:

_____
Major Professor

_____
Committee Member

_____
Committee Member

_____
Dean of Graduate Studies

UTAH STATE UNIVERSITY
Logan, Utah

1989

# ACKNOWLEDGEMENTS

I would first like to thank our Lord and Savior, Jesus Christ who taught that we should have faith in God and that "what things soever ye desire...believe that ye receive them, and ye shall have them" (Mark 11:22, 24 KJV). Without His help, this thesis would never have been possible.

I would also like to thank my beloved wife, Trina, who continually helped me to keep my faith that I would finish this project. I apologize to her for the time I had to spend away from home and for the many times I came home seemingly upset at her. Trina, you have always had a special place in my heart, and I hope you know that the sacrifices you have made and the love you have shown so I could pursue my degree have not gone unnoticed. Thank you to my children, David and Justin. You kids are the best kids a father could ask for. I apologize for the many times my temper was short with you while I was working on this thesis and for the time I didn't have to spend with you. I love you both very much.

I would like to thank Don Thompson and Neil Myers for their patience and their time in answering the many questions I had while I was working on my degree. You were a tremendous help. Good luck in your work.

Finally, I thank Dr. John Raitt and my other committee members for their time taken during the preparation and review of my thesis and for their many suggestions.

<div align="right">Jon Alan Roberts</div>

# TABLE OF CONTENTS

LIST OF TABLES

LIST OF FIGURES

# ABSTRACT

Measurements of the Interaction of High-Voltage Biassed

Conductors with the Ionosphere

by

Jon A. Roberts, Master of Science

Utah State University, 1989

Major Professor: Dr. W. John Raitt
Department: Soil Science and Biometeorology

The Space Power Experiments Aboard Rockets program was developed to study the interaction of high-voltage biassed conductors with the low earth orbit environment. The experiment utilized two spherical conductors, which were biassed to potentials as high as 45,000 volts, and the steady-state current-voltage characteristics were analyzed. The spheres were flown in three different orientations with respect to the earth's magnetic field. At times, only one sphere was biassed so that the current collection characteristics of a single spherical conductor could be studied. At other times, both spheres were biassed to approximately the same voltage, or to greatly differing voltages so that the interactions between charge sheaths could be studied. The failure of the plasma contactor allowed the rocket body to charge to up to several kilovolts negative during sphere biassing, resulting in the establishment of an unplanned positive ion sheath around the rocket body, thereby complicating the interpretation of the current-voltage characteristics of the spheres. Specifically, the following areas were studied: current-voltage characteristics with respect to altitude, magnetic field orientation, and attitude control system activity. In addition, the characteristics of a possible volume breakdown were

analyzed, along with the charging of the rocket body and interactions between charge sheaths. Finally, these results were compared with analytical and numerical models.

(120 pages)

# CHAPTER I

## INTRODUCTION

From now into the next century, quantum leaps will be made in the utilization of space; in particular, the near Earth space environment. Spacecraft power levels will steadily increase to 20 MW by the end of the 20th century and will reach $10^4$ MW during the 21st century [Dunbar, 1980]. As space platforms become larger and more complex, these large amounts of electrical power must be distributed throughout the platform, and there are good reasons why this may be best accomplished at potentials of 10's of kilovolts. Power transmission lines contribute to total system weight in three ways: weight of the transmission line itself, weight of the power system needed to generate the extra power required to make up for power loss in the transmission line, and the weight of the heat elimination system needed to dissipate the heat generated by the power loss through the transmission line [Finke et al., 1978]. On a large platform, such as the space station, high voltages will reduce the size and weight of the power distribution system.

Electrical power can be determined from:

$$P = VI = V^2/R$$

where P is the power in watts,

V is the applied voltage in volts,

I is the current in amps, and

R is the resistance in ohms.

A large space system will require long transmission lines to deliver power throughout the system. As a result, the total resistance in the transmission lines will increase as the transmission lines increase in length. Therefore, higher voltages will be required to deliver a given amount of power to the load. But, for a given amount of power, higher

voltages will require less current, thus reducing the size and weight of the transmission lines carrying the current.

High-voltage electrical conductors must be well insulated to prevent current breakdown, which can have devastating effects on the safety of the platform and the crew. At the least, a breakdown can result in a drainage of electrical currents from the desired load, while more significant and serious problems can result if a breakdown results in critical circuit overloads and upsets. Carrying sufficient insulating material into low Earth orbit (LEO) aboard the platform can be extremely costly, thus the ability of the ambient low Earth orbit environment to provide the required insulation must first be studied. The neutral atmospheric pressure of the LEO environment is low enough to provide good insulation but contains free electrons and positive ions, the effects of which must be considered when applying high voltages to a conductor. The Space Power Experiments Aboard Rockets (SPEAR) program was designed to study the interactions of high-voltage biassed conductors with the LEO ionosphere. SPEAR-1 was the first of two such experiments.

## Review of Literature

Numerous space missions have either intentionally or unintentionally recorded effects from electrical charging due to the conditions present in the ambient environment. Other experiments have electrically charged space platforms by the emission of charge particle beams, with the resulting modification of the environment in the vicinity of the platform. SPEAR-1 is the first experiment flown that was designed specifically to study how a conductor biassed to 10's of kilovolts interacts with the LEO space environment without additional charge contamination of the environment.

Many articles have been published on the problem of vehicle charging by both artificial means and due to conditions in the ambient environment--both at high and low

altitudes. Two review papers that discuss the processes involved in charge build-up on an object in outer space are by Garrett [1980] and Whipple [1981]. Garrett's article is mainly concerned with the electrical charging of spacecraft in Earth orbit. His paper includes a discussion of current sources and the ambient environment, and he also discusses some of the various spacecraft-charging models. He concludes his article with a discussion of interactions between a charged spacecraft and its environment by mainly focusing on extreme charging events and satellite anomalies and methods used to prevent vehicle charging, from simple design considerations to more active methods such as charged particle beams. Whipple's work is similar to Garrett's except he also provides a survey of early works on charging. He also looks at the charging of such objects as interplanetary and magnetospheric dust, the lunar surface and other bodies in the solar system, and interstellar dust.

Studies of environmentally induced vehicle charging have been underway since the early 1970s when system disruptions of geostationary satellites were first determined to be environmentally induced. Since that time, electron and positive ion beams have been utilized to artificially charge space vehicles and to control environmentally induced charging. Only recently have experiments been performed that biassed conductors to high voltages without the use of artificial beams.

Most of the literature on environmentally induced vehicle charging is concerned with charging on geosynchronous satellites, since this is where the environmental conditions produce most of the significant vehicle charging. Knott [1972] proposed that for a magnetospheric satellite, the equilibrium potential is strongly dependent on the energy distribution of the particles and that secondary electron emission can help reduce a highly negative equilibrium potential of a satellite. Since that time, many authors have published data showing the energy of the particles that caused large negative potentials to build up on geosynchronous satellites. Reagan et al. [1981] showed that differential charging between Kapton and Teflon dielectric materials on the SCATHA satellite during

eclipse was caused by electrons with energies less than 30 keV. Olsen [1983] analyzed data from both the ATS-6 and SCATHA satellites and showed that significant negative charging required plasmasheet electron fluxes to have energies of at least 10 to 20 keV. This threshold was a result of the effect of secondary electron emissions. Above this range, secondary electron yield drops below 1 emitted electron per incident electron, allowing high levels of charging to take place. Gussenhoven and Mullen [1983] studied SCATHA data from a different charging event than that studied by Reagan et al. and found the satellite charged to -8 kV in eclipse and -340 V in sunlight due to an injection of electrons in the 30 to 335 keV range. McPherson and Schober [1976] showed that most geosynchronous satellite anomalies occurred during the vehicle's passage through eclipse in the midnight-to-dawn sector. They suggested one possible reason for these anomalies is that high-energy electrons can penetrate fairly deeply into satellite dielectrics, resulting in the establishment of electric fields inside the material. When the field strength exceeds the dielectric strength of the material, breakdown occurs. Mullen et al. [1986] showed that daylight potentials on SCATHA of -340 V to -740 V was a result of a charged particle flux of greater than 30 keV, with lower energy fluxes being balanced by backscattered and secondary electrons. These few examples alone show that the ambient environment plays a significant role in determining the equilibrium potential of geosynchronous satellites. In fact, environmentally induced charging events of -10 kV have been reported [DeForest, 1972].

Because of the high negative potentials possible at geosynchronous altitudes, methods that could reduce these potentials were studied. Olsen [1981] showed that emission of thermal electrons on ATS-5 reduced potentials to hundreds of volts negative for short periods but that differential charging on solar arrays prevented a complete discharging of the vehicle and allowed the vehicle to recharge in spite of the electron emission. Purvis and Bartlett [1980] and Olsen [1985] also showed that charged particle emission could reduce high negative potentials on ATS-5 and ATS-6.

The formation of potential barriers also has a significant effect on vehicle charging. Olsen and Purvis [1983] showed that during eclipse, ATS-6 reached a high negative equilibrium potential in a matter of seconds after energetic particle injection, while in sunlight, approximately 50 minutes was required for the vehicle to decrease to a few hundred volts negative. This time delay was a result of potential barrier formation due to differential charging between sunlit and shadowed surfaces. This potential barrier was first described operationally by Whipple [1976]. A potential barrier can also result from energetic particles striking different materials on the satellite, resulting in differential charging and the establishment of strong electric fields [Knott, 1972].

Cauffman and Maynard [1974], using Explorer 45 data, first showed a shift from a plasma dominated potential distribution to a photoelectric-dominated distribution with increasing altitudes. Since the LEO environment is dominated by a cold, dense plasma, significant environmentally induced vehicle charging events have not been reported by equatorial-orbiting or polar-orbiting vehicles because the vehicle can easily attract a current from the dense ambient plasma to offset any significant environmentally induced charging. In fact, the floating potential of a vehicle in LEO is typically only -0.5 to -1 volt. Many experiments have been performed in LEO by ejecting electron beams, but since these experiments were designed mainly to study the magnetosphere little conclusive data on the amount of vehicle charging can be determined. Winckler [1980] provides an excellent review of many electron beam experiments. Recently, however, a series of tethered sounding rocket experiments have been performed to study the charging of a vehicle in LEO due to electron beam emission. The experiments basically consist of a daughter payload separated by a wire tether from the mother payload. The daughter acts as the reference potential, and the electron beam is emitted from the mother. Sasaki et al. [1987] summarized three tethered payload experiments (TPE) in which 1 keV electron beams were emitted with currents of up to 80 mA. In these three experiments, the maximum amount of charging of the mother payload was only on the order of 10 volts at

an altitude of 150 to 200 km. This low amount of charging cannot be explained simply by the return current from the ambient ionosphere. It was found that the electron beam itself produced plasma during beam collisions with neutral atmospheric gases and that these electrons were the major current source to the mother payload, thus minimizing vehicle charging. Kawashima et al. [1982] showed during one of these three TPEs that the beam direction played an important part in determining the amount of vehicle charging. He found that electron beams emitted perpendicular to the Earth's magnetic field produced the least amount of charging because the beam electrons were deflected back to the rocket body, resulting in a suppression of charging. Raitt et al. [1987] showed that at $F_2$ region, mid-latitude altitudes, charging via electron beams is determined by a balance between the electron beam flux and the return current from the ionosphere. They showed that the space shuttle will typically charge to only about 10 volts during a 1 keV, 100 mA beam emission but can charge to up to 100 to 200 volts when the engine nozzles are in the vehicle wake (the engine nozzles are the only conductors on the shuttle exposed to the environment). In a LEO environment, the only significant environmentally induced charging events occur in polar-orbiting vehicles during their passage through the auroral zones where magnetic field lines have direct access to the solar and energetic magnetospheric plasmas and where there are regions of reduced ionospheric plasma density (troughs). In a polar environment, the most important charging parameter to consider is the ratio of high energy electrons to all ions [Laframboise and Parker, 1987]. Parks and Katz [1981] showed that in polar orbit with a field-aligned flux of 5 to 10 keV electrons, the shuttle could charge to potentials as high as 1 kV.

Only two experiments have been performed to date in which conductors were deliberately biassed to high positive potentials without the use of artificial means such as electron guns. The CHARGE-2 sounding rocket was the first [N. B. Myers et al., A comparison of current-voltage relationships of collectors in the Earth's ionosphere with

and without electron beam emission, in press Geophys. Res. Lett., 1989], and SPEAR-1 is the second and is the subject of this thesis.

Some of the earliest experiments involved in the analytic study of a high voltage object immersed in a plasma were performed by Langmuir and associates in the first quarter of the 20th century. Langmuir [1913] first studied the problem of space-charge-limited currents between flat parallel planes. He then studied the problem of current flow between coaxial cylinders [Langmuir and Blodgett, 1923] and concentric spheres [Langmuir and Blodgett, 1924] where the cathode was outside the anode and vice versa. In all of these papers, he derived the maximum space-charge-limited current that can flow for a given potential between the anode and cathode. Since the equations were developed for use in vacuum tube technology, they neglected the effects of the magnetic field and so represent an upper limit to the amount of current that can be collected. They found that the current collected for spherical conductors was proportional to $V^{6/7}$ (were V is the potential in volts). Nevertheless, these equations can still be useful in studying what effects are important in the current collection capability of high-voltage objects exposed to the ionosphere. Beard and Johnson [1961] first applied Langmuir and Blodgett's spherical space-charge-limited work to the LEO ionosphere.

Parker and Murphy [1967] included the effects of the Earth's magnetic field. They showed that under the constraints of conservation of canonical angular momentum and energy, some electrons can drift across magnetic field lines and be collected by a high voltage conductor. Any electrons originating outside a critical radius $r_0$ are dynamically forbidden from reaching the collector. In the Parker-Murphy model, the current collected by a high voltage conductor is proportional to $V^{1/2}$. Because this model forces single particle constants of motion, it represents a lower limit to the current that can be collected by a high voltage object.

Linson [1969] went one step further than Parker-Murphy by assuming that high voltages will result in plasma turbulence, so that single particle constants of motion are

not conserved and electrons can cross magnetic field lines. Thus, Linson's model is an intermediate model between Langmuir-Blodgett and Parker-Murphy, and the current collected is proportional to V/ln V.

This thesis is a detailed analysis of the data returned from the SPEAR-1 sounding rocket flight in which two spherical conductors were biassed to potentials as high as 45 kV so that the interactions between the conductors and the LEO ionosphere could be studied. The thesis begins with a review of the diurnal, seasonal, and solar cycle variations in the LEO atmosphere. Next, the physics of charging by an object immersed in a plasma is presented, along with a review of the analytical and numerical models of current collection by high voltage conductors. A brief description of the SPEAR-1 vehicle follows. Finally, an analysis of the SPEAR-1 data is presented, concluding with a discussion of possible future work which should be pursued to better understand the interactions between a high voltage conductor and the LEO ionosphere.

# CHAPTER II

## DESCRIPTION OF THE LEO ENVIRONMENT

The low Earth orbit environment will be defined as the region of the atmosphere between 100 km and 1000 km above mean sea level. The lower limit is the approximate altitude above which molecular diffusion processes begin to dominate the atmospheric composition, and the upper limit is the approximate altitude limit of manned orbiting vehicles. The Space Shuttle, and soon the space station, fly exclusively in the LEO environment in an approximately circular orbit between 200 and 400 km, while other satellites fly elliptical orbits that often bring them into the LEO environment for large amounts of time. Thus, it is necessary to be familiar with the environment in which these vehicles are flying. This environment can show large variations with solar activity, time of year, time of day, and latitude.

### Neutral Atmosphere

The Mass Spectrometer Incoherent Scatter (MSIS-86) model [Hedin, 1987] provides information on the total neutral density; the densities of H, He, N, O, $N_2$, $O_2$, and Ar; neutral temperature; neutral pressure; and the mean free path of atomic oxygen for any given location and altitude range when the previous day's $F_{10.7}$ flux, the three month average $F_{10.7}$ flux, and the daily $A_p$ index are input. The $F_{10.7}$ flux is the solar energy flux at the 10.7 cm wavelength and is proportional to the amount of ultraviolet and extreme ultraviolet energy streaming from the sun. The $A_p$ index indicates the amount of disturbance in the geomagnetic field. Figure 2.1 shows the neutral LEO composition for mid-latitude, daytime, solar minimum conditions from the MSIS model. One can see that at Shuttle/space station altitudes, the primary neutral constituents are O (atomic oxygen)

and $N_2$ (molecular nitrogen). Only at higher altitudes do the lighter gases (H and He) become dominate.

Figure 2.2 shows diurnal variations of neutral pressure and temperature. In this example, daytime temperatures are about $200^\circ$ K warmer than nighttime temperatures due to neutral ionization and the resulting heating during the day, and the daytime pressures are greater than nighttime pressures. To a first approximation, the atmosphere is in hydrostatic equilibrium. As a result, pressure falls off exponentially with height such that:

$$p(z) = p_o \exp\left( -\int_{z_o}^{z} \frac{dz}{H} \right) \qquad (2.1)$$

where $H = kT / mg$ is the scale height, $p_o$ is the pressure at a reference level $z_o$, k is the Stefan-Boltzmann constant, T is the temperature, m is the mass, and g is gravity. Since daytime temperatures are greater than nighttime temperatures, one can see from Equation (2.1) that the pressure must fall off more slowly during the day than at night to maintain hydrostatic equilibrium. Temperatures become nearly isothermal at an altitude where the pressure (or density) of the neutrals becomes low enough that the mean free path between collisions is very long, resulting in a large thermal conductivity and little temperature gradient with height.

Figure 2.3 shows the seasonal variations of pressure and temperature. Maximum LEO temperatures show seasonal variations due to the differing amounts of solar heat input present during the seasons, with summertime pressures falling off more rapidly with altitude than in any of the other seasons. During the summer months, $N_2$ density is greater at a given altitude in LEO than in the winter. This is a result of larger amounts of heat input into the atmosphere arising from larger ionization rates due to lower solar zenith angles. The result is increased upward vertical motion advecting $N_2$ upward from below [Richmond, 1982]. Since there is an increase in the heavier $N_2$ molecules during

the summer at a given altitude, the pressure must fall off more rapidly with altitude to maintain hydrostatic equilibrium, by Equation (2.1).

Figure 2.4 shows the solar cycle variations in pressure and temperature. Neutral temperatures are near $1500^\circ$ K during solar maximum due to the large amounts of atmospheric heating resulting from the influx of energetic particles and the increased solar x-ray output during flares. The neutral pressure drops off more slowly than during solar minimum because of the increased atmospheric temperature and changes in the meridional circulation patterns seen with increased solar activity [Richmond, 1982].

## Ionosphere

The International Reference Ionosphere (IRI) model [Rawer et al., 1981] provides information on the electron density; the ratio between electron density and density at the $F_2$ peak; neutral, electron, and ion temperatures; the ratio between electron and ion temperatures; and relative percentage densities for $O^+$, $H^+$, $He^+$, $O_2^+$, and $NO^+$ for any location and altitude range when the 12 month running mean of the Zurich sunspot number is input along with the local time. Figure 2.5 shows the ionospheric relative percentage density for the various IRI output constituents. At current operational LEO altitudes, which is near the $F_2$ peak, $O^+$ is the dominate ion present, arising from the photoionization of atomic oxygen, while at the upper limit of LEO, $O^+$ and $H^+$ are present in equal concentrations. In lower portions of LEO, $NO^+$ is the dominate ion. The ionosphere is imbedded in a magnetic field with a strength on the order of 0.3 to 0.4 gauss. The solar flux is nearly unattenuated in the important x-ray and ultraviolet wavelengths, with a total solar energy flux of about 1400 W m$^{-2}$.

Figure 2.6 shows the day-night variations in electron temperatures and densities for a mid-latitude location. Electron density shows a strong diurnal variation below about 300 km, and only a weak diurnal variation above that altitude. Below 300 km, ionization

is mainly influenced by solar radiation because of the higher neutral densities, so that during the day, ionization readily increases the electron density, while at night, recombination rapidly decreases electron density. Above 300 km many effects, which are always present, influence the electron density. The most important of these effects is diffusion from below. As a result, there is less variation in the electron density in this region. Electron temperature shows a strong diurnal variation, with temperature generally increasing with altitude. The daytime temperature profile is primarily a result of heating by photoionization, and the nighttime ionospheric temperature is maintained by large downward heat fluxes from the magnetosphere, resulting in conduction of heat to the F-region and below [Banks and Kockarts, 1973].

Figure 2.7 shows the seasonal variations in electron density and temperature. The most significant feature is the greater electron density in the fall and winter months at the $F_2$ peak than in the spring and summer, even though a lower solar zenith angle would suggest a lower ionization rate. This feature is called the 'winter anomaly' and results from atmospheric composition changes across the seasons. In the F-region, the following chemical reactions are important:

$$N_2 + O^+ \rightarrow NO^+ + N$$
$$NO^+ + e^- \rightarrow N + O$$
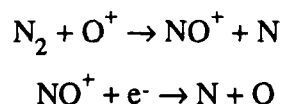
As described earlier, the molecular nitrogen density $[N_2]$ is higher during the summer months than winter, yet $[O^+]$ remains approximately constant throughout the year. Therefore, during the summer, a greater $NO^+$ production is realized by the first reaction, but yields no additional ionization. By the second reaction then, electrons are lost at a greater rate during the summer so that resulting electron densities are lower [Richmond, 1982]. Electron temperatures tend to be highest in the summer due to the greater amounts of solar radiation present.

Figure 2.8 shows the solar cycle variation in electron densities and temperatures. Electron densities are greatest during solar maximum due to the increased energy output from the sun during solar flares. Electron temperatures during solar maximum are lower than in solar minimum due to the fact that the electron heating rate is proportional to electron number density ($N_e$), while the electron cooling rate is proportional to the square of the electron density [Bauer, 1973]. Figure 2.9 shows a comparison between neutral and electron densities for LEO altitudes for mid-latitude, daytime, solar minimum conditions.

IRI density predictions for the conditions present during the SPEAR-1 flight ranged from $10^{10}$ $m^{-3}$ at about 185 km to 9 x $10^{10}$ $m^{-3}$ at apogee, with a peak density of $10^{11}$ $m^{-3}$ at about 270 km. Temperature predictions increased from about $600^\circ$ K at 185 km to $1200^\circ$ K at about 300 km, and nearly isothermal above. The MSIS model predicted neutral pressures to decrease from $10^{-6}$ torr at 185 km to about 8 x $10^{-9}$ torr at apogee, and neutral temperatures to increase from about $700^\circ$ K at 185 km to $760^\circ$ K at 300 km, and isothermal above.
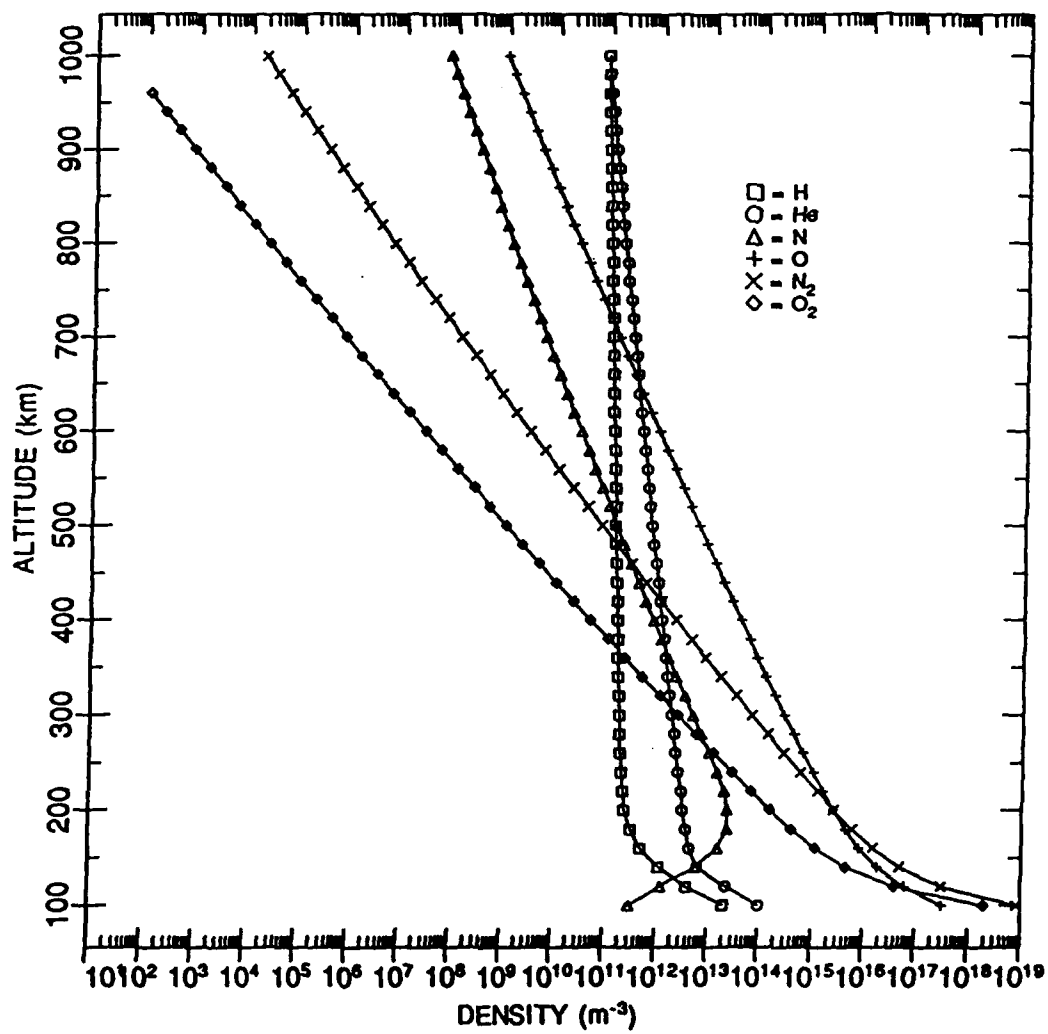
Fig. 2.1. MSIS-86 model showing the neutral composition of the atmosphere for mid-latitude, daytime, solar minimum conditions.
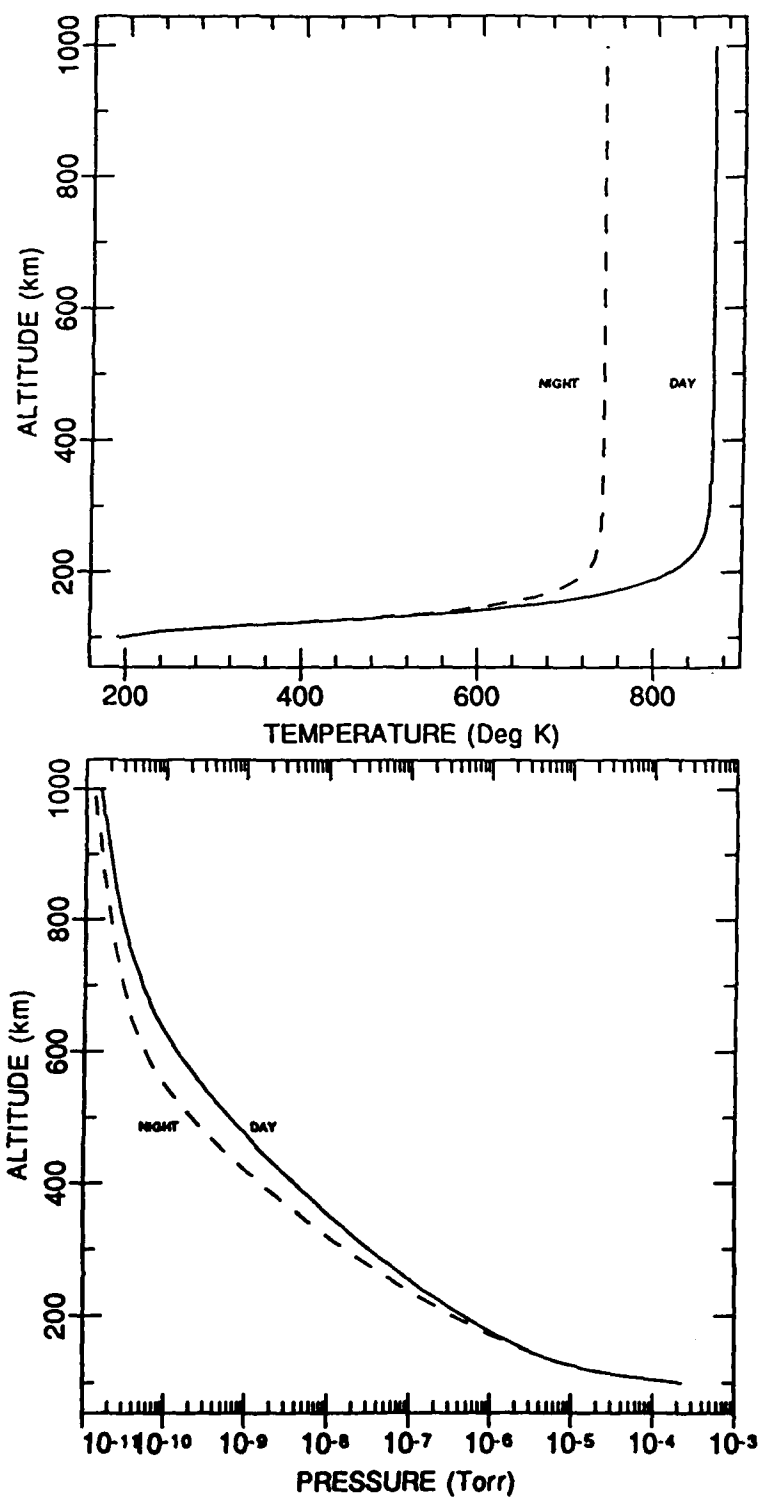
Fig. 2.2.  MSIS-86 comparison of the mid-latitude diurnal variations in
neutral pressure and temperature.
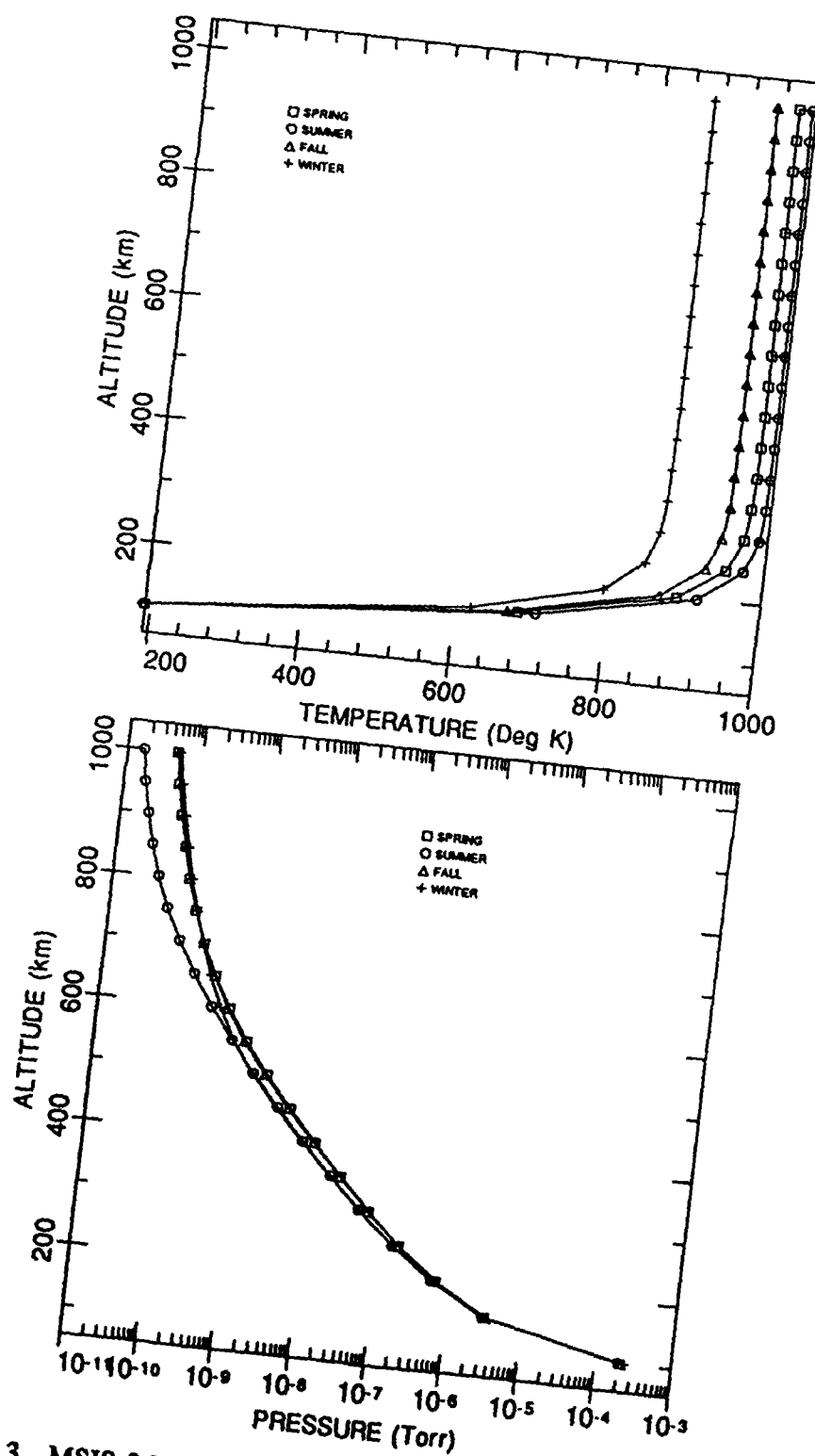
Fig. 2.3. MSIS-86 comparison of the mid-latitude seasonal variation in neutral pressure and temperature.
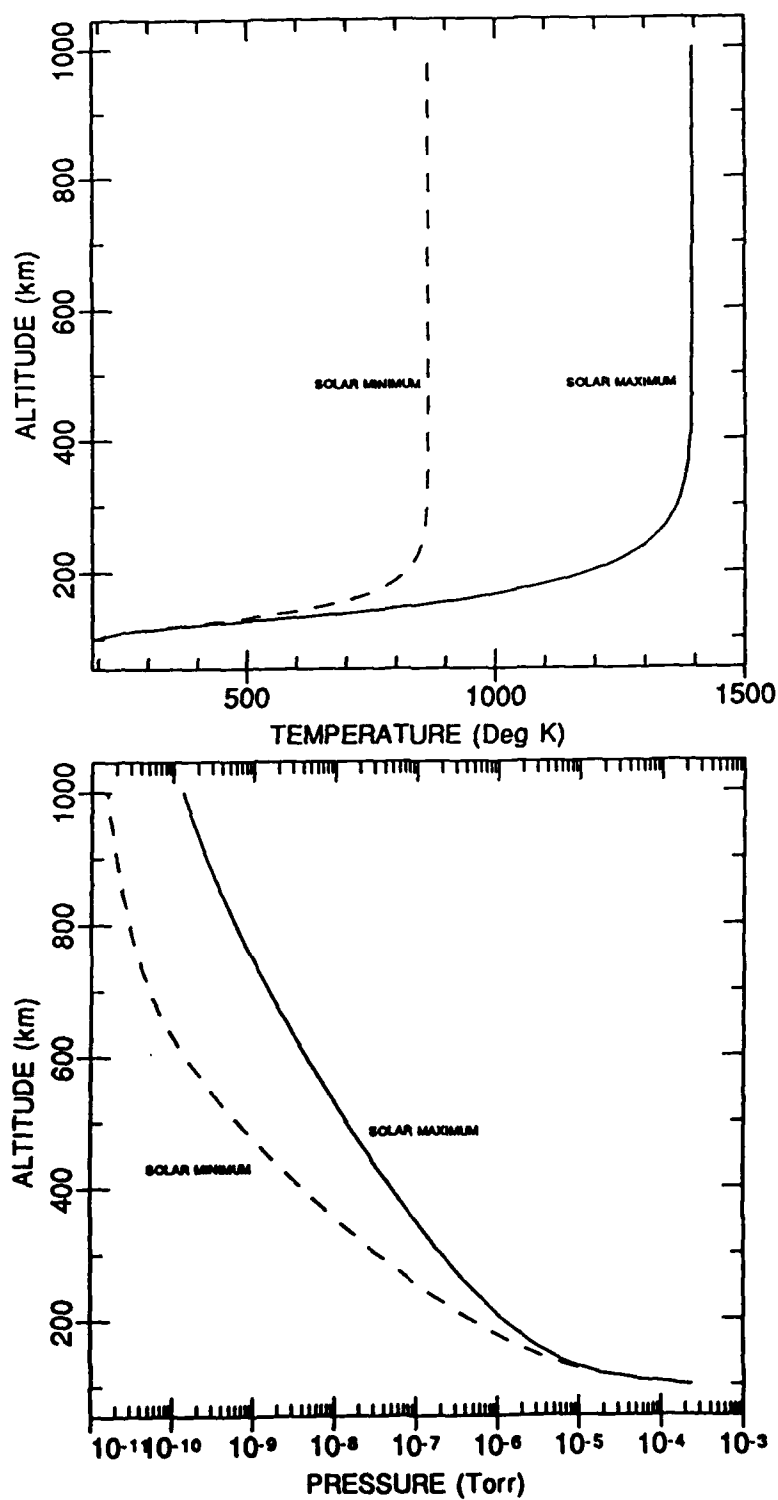
Fig. 2.4.  MSIS-86 comparison of the mid-latitude solar cycle variations in neutral pressure and temperature.
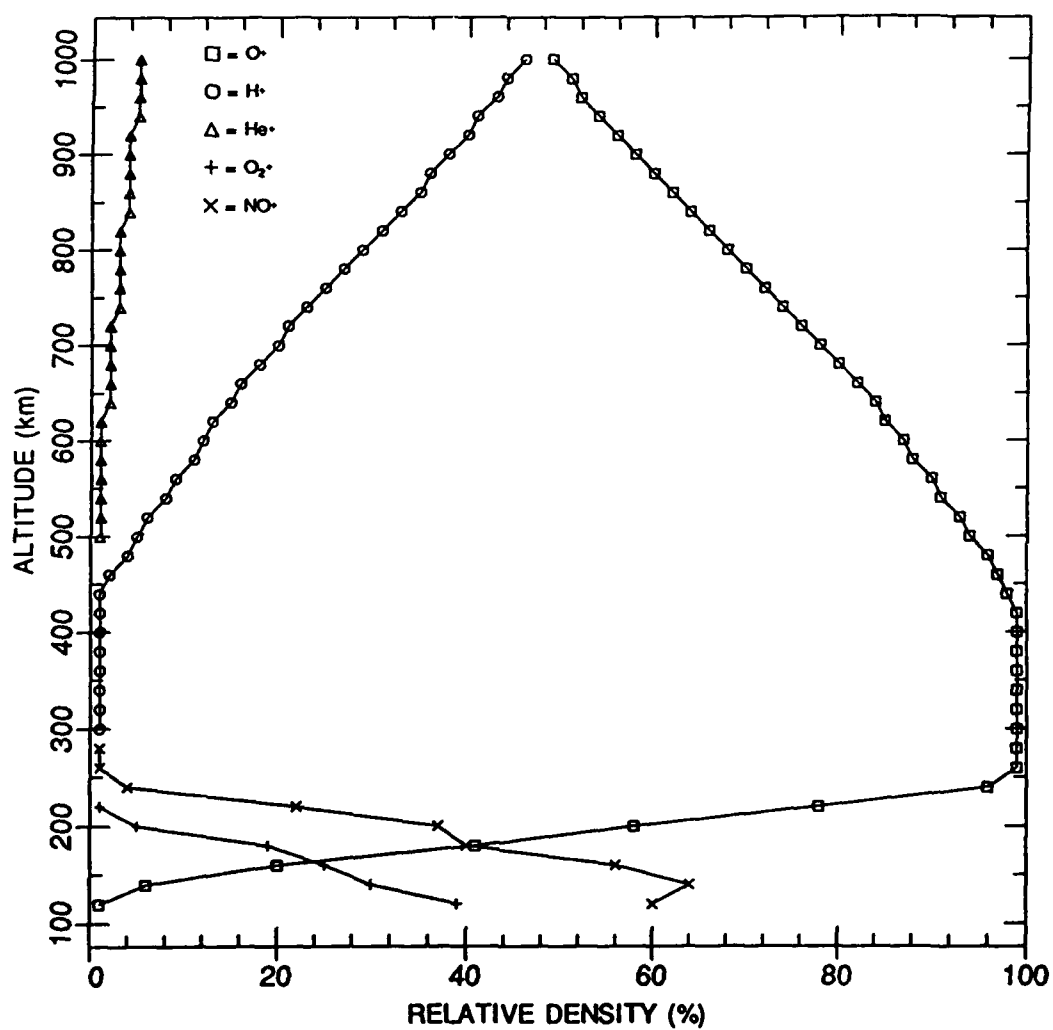
Fig. 2.5. IRI model showing the relative percentage density of the various model output components of the atmosphere for mid-latitude, daytime, solar minimum conditions.
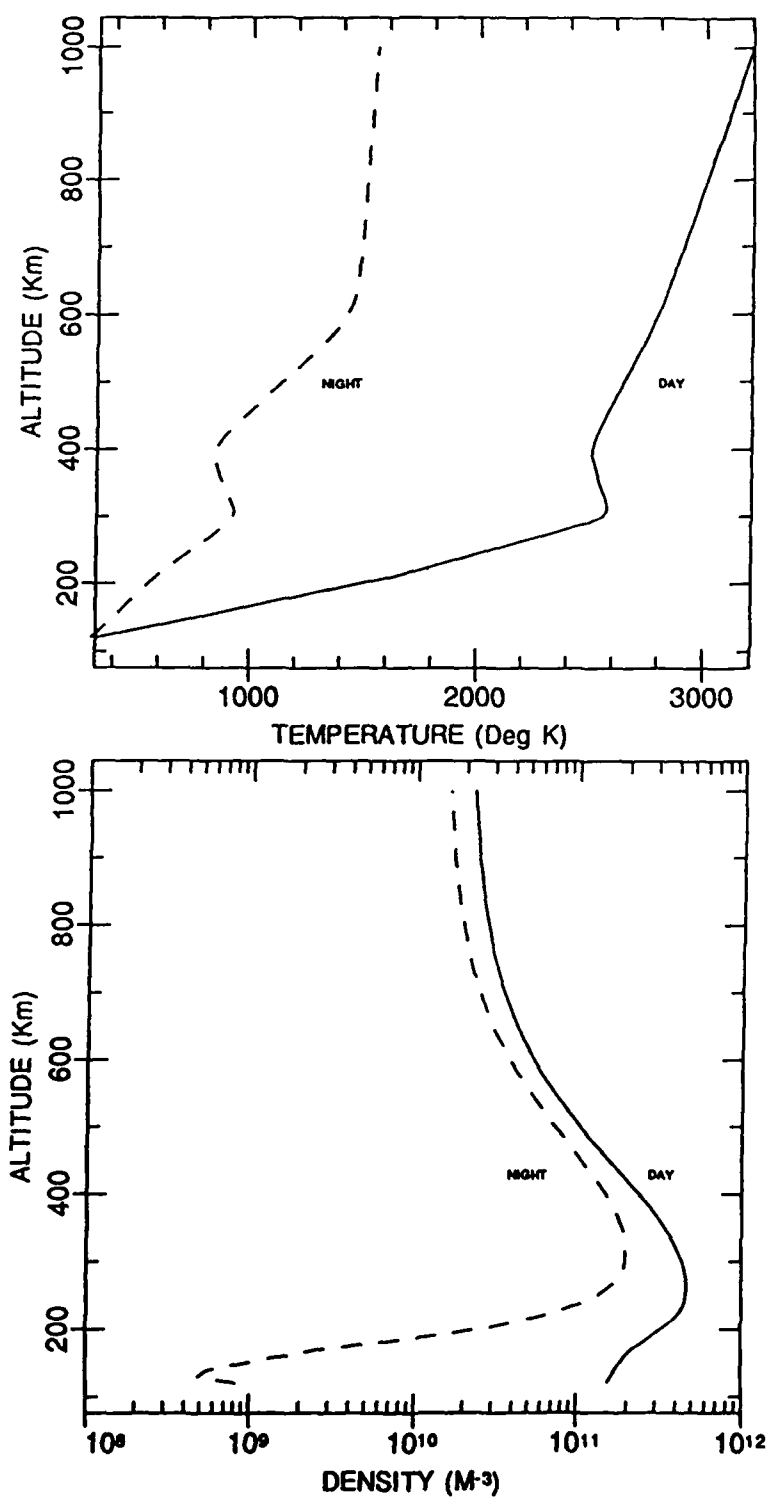
Fig. 2.6. IRI comparison of the mid-latitude diurnal variation of electron temperature and density.
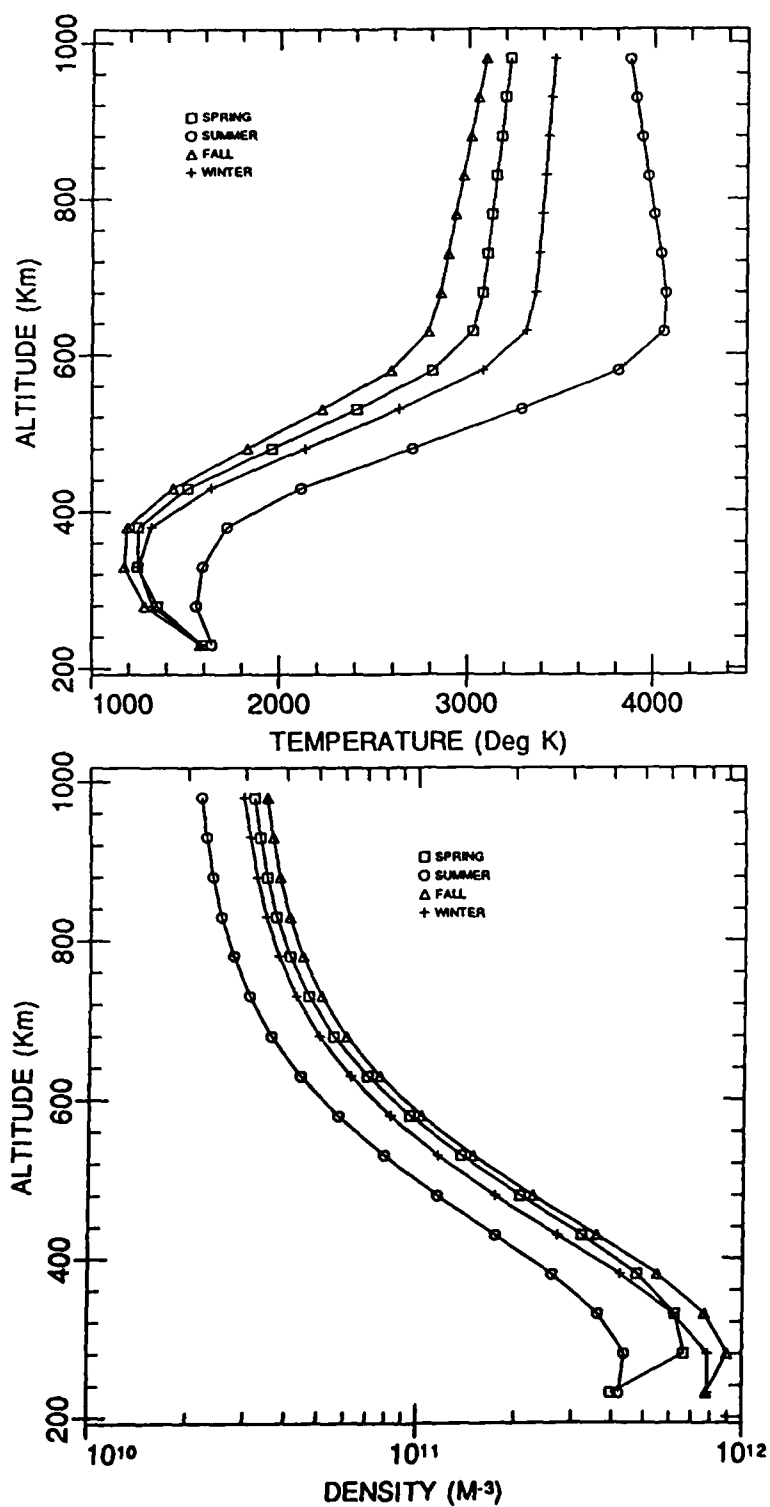
Fig. 2.7. IRI comparison of the seasonal mid-latitude variation of electron temperature and density.
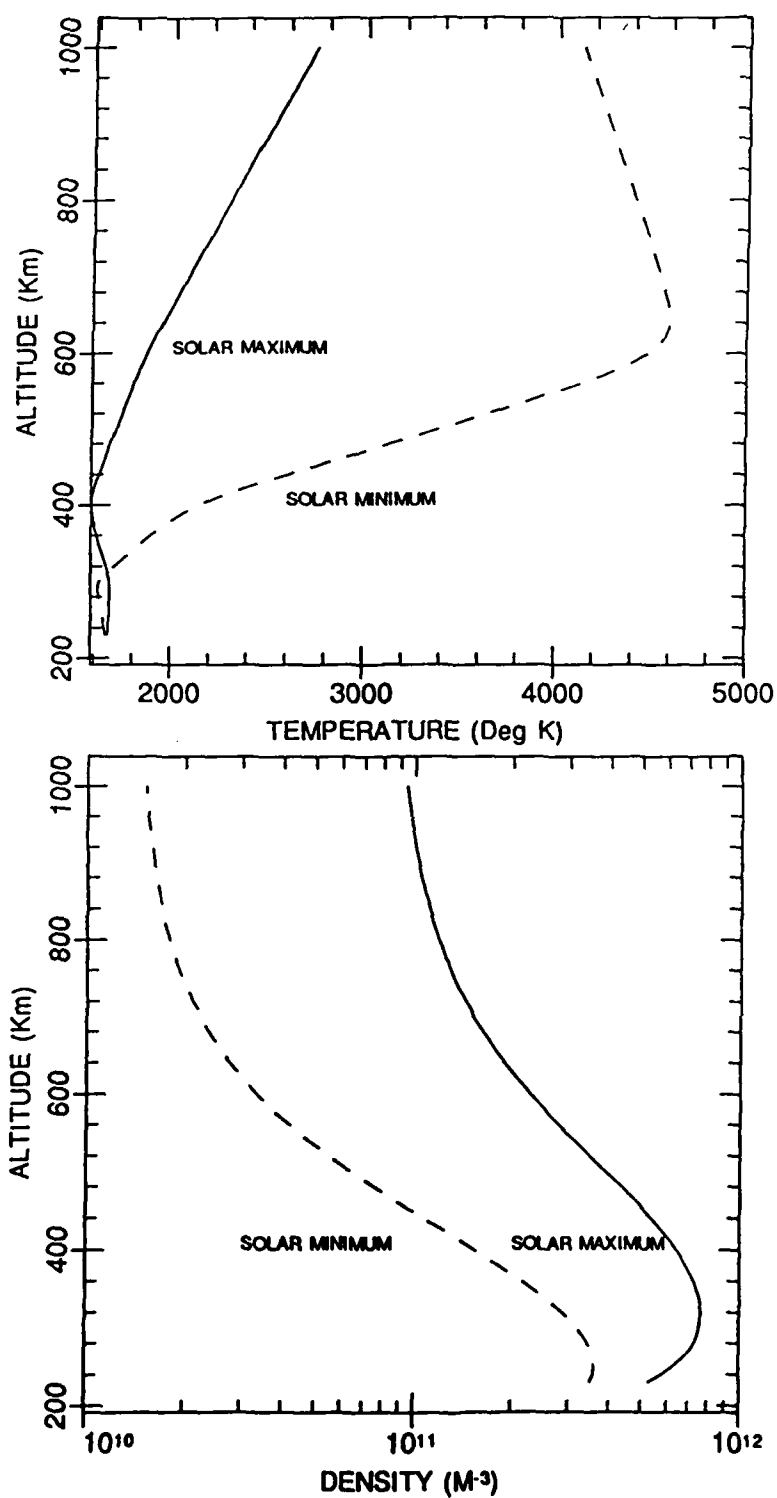
Fig. 2.8. IRI comparison of the mid-latitude solar cycle variation of electron temperature and density.
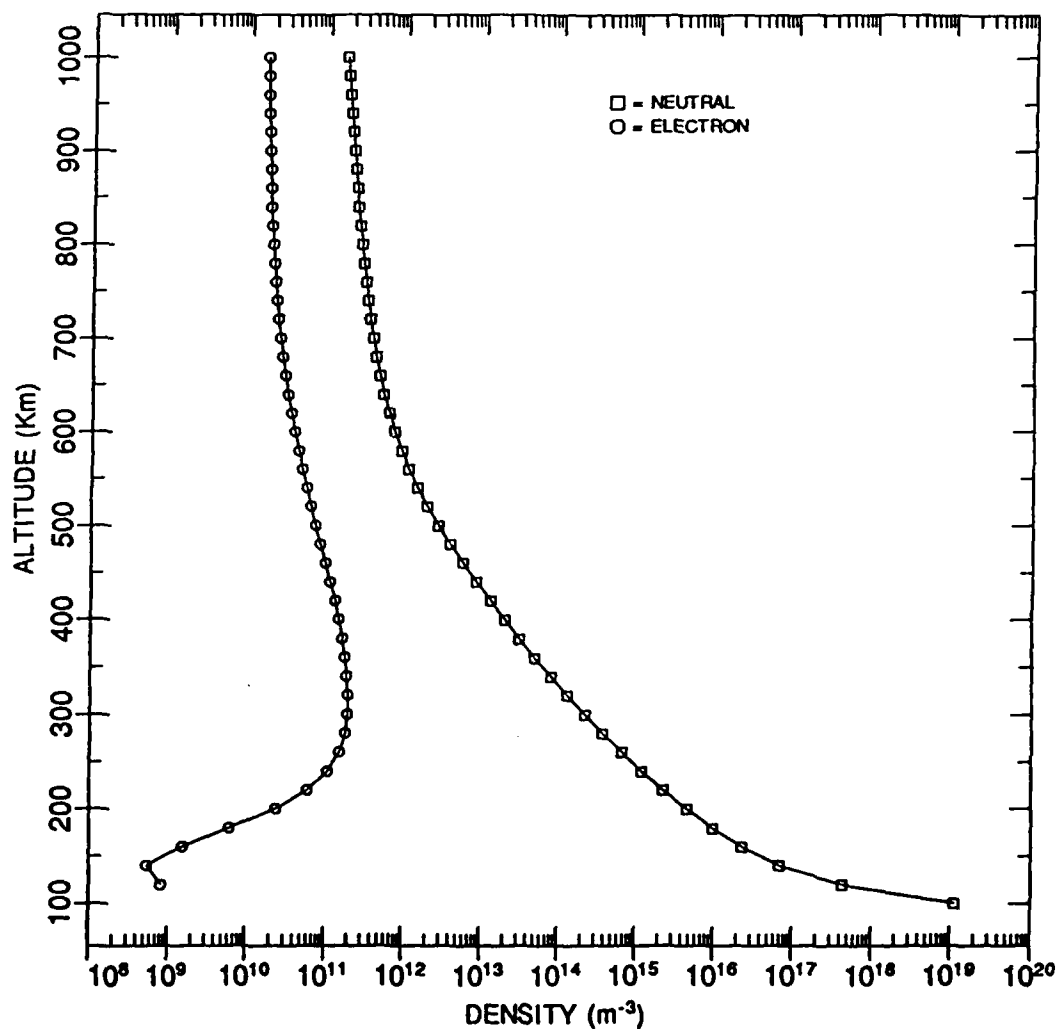
Fig. 2.9. Comparison between neutral (from MSIS-86 model) and electron (from IRI model) densities for mid-latitude, daytime, solar minimum conditions.

# CHAPTER III

## MECHANISMS AND MODELS OF CURRENT COLLECTION
## BY OBJECTS EXPOSED TO A SPACE PLASMA

An object either stationary or in planetary orbit has the possibility of passively developing a charge imbalance on its surface merely by the presence of free electric charge carriers or active:, as the result of processes occurring on the vehicle. This charge imbalance results from the movement of charge carriers, or currents, into or out of the object. Once the charge imbalance occurs, a charge density $\rho$ will be established on the vehicle's surface resulting in the establishment of an electric field between the vehicle and the ambient plasma according to Gauss' Law:

$$\nabla \cdot \mathbf{E} = \frac{\rho}{\varepsilon_o} \qquad (3.1)$$

This electric field can be described in terms of a potential distribution V given by:

$$\mathbf{E} = -\nabla V \qquad (3.2)$$

Combining Equations (3.1) and (3.2) yields Poisson's Equation:

$$\nabla^2 V = -\frac{\rho}{\varepsilon_o} \qquad (3.3)$$

which describes the potential distribution in terms of the charge density.

Once the electric field is established, the charge carriers in the plasma will begin to rearrange themselves in response to the electric field. In the case of an imbalance of positive charge carriers on the object, electrons will be attracted to the object and positive ions will be repelled, resulting in the establishment of a negative space charge, or sheath, around the positively charged object. Similarly, a negative charge carrier imbalance will

result in the establishment of a positive charge sheath around the object. The effect of the charge sheath is to shield the remaining plasma from the charged object. The electrical potential at the sheath's edge is zero and the total charge within the sheath is equal to the charge on the object. At altitudes where collisions in the sheath can be ignored, this rearrangement of the plasma charge carriers creates a distribution function which satisfies the collisionless Boltzmann equation:

$$\frac{\partial f}{\partial t} + \frac{\partial f}{\partial x_i} + \frac{qE_i}{m}\frac{\partial f}{\partial v_i} = 0$$

The thickness of the charge sheath at small potentials is related to the Debye length:

$$L = \left(\frac{\varepsilon_0 kT}{nq^2}\right)^{1/2}$$

by a potential distribution $\Phi = \Phi_0 \exp(-r/L)$ where r is the radial distance from the object's surface.

Several processes can contribute to charge transfer between the object and its environment:

a. Electron or ion currents from the ambient plasma;

b. Photo-electron currents;

c. Secondary electron currents;

d. Induced currents arising from motion through a magnetic field;

e. Artificially enhanced currents.

This movement of charge carriers will continue until the net current to the vehicle is zero and an equilibrium potential is reached. This chapter will discuss these processes and examine the analytical and numerical models that describe the current collection capabilities of high-voltage conductors.

Mechanisms of Current Collection in a

Space Plasma

## Plasma Currents

Plasma currents represent the primary current source to an uncharged vehicle in LEO. The ambient ionospheric plasma can be assumed to be Maxwellian. Therefore, the average particle speed is given by:

$$c = \left(\frac{8kT}{\pi m}\right)^{1/2}$$

where   k is the Stefan-Boltzmann constant,

T is the particle temperature, and

m is the particle mass.

For an $O^+$ dominated ionosphere with $T_e = T_i = 1000^oK$, the mean electron speed ($c_e$) is ~200 km/sec and the mean ion speed ($c_i$) is ~1 km/sec. For a vehicle moving at suborbital speeds, the electrons are moving much faster than the vehicle, and the vehicle is nearly stationary with respect to the ions, resulting in an electron flux to the vehicle much greater than the ion flux. As a result, there will be a net accumulation of negative charge carriers to the vehicle. The vehicle will become negatively charged in order to repel electrons and attract ions, so that the net current to the vehicle will be zero.

The electron current density to a vehicle moving at a speed $v_s \ll c_e$ is given by:

$$j_e = \frac{1}{4}n_e q c_e$$

and the ion current density to the same vehicle moving at a speed $v_s \gg c_i$ is given by:

$$j_i = n_i q v_s$$

where $n_e$ and $n_i$ are the electron and ion densities, respectively,

q is the elementary charge,

$c_e$ is the average electron speed, and

$c_i$ is the average ion speed. q will be positive for positive ions and negative for electrons, indicating the direction of current flow.

Thus, current densities at LEO altitudes (where $n_e = n_i = 10^{12} \text{ m}^{-3}$) are:

$$j_e = -8 \times 10^{-3} \text{ A m}^{-2}$$
$$j_i = 1.6 \times 10^{-4} \text{ A m}^{-2}$$

One of the most striking examples of charging due to energetic plasma currents occurred on ATS-5, a geostationary satellite launched on August 12, 1969 [DeForest, 1972]. This satellite was seen to charge to typical potentials of 3000 - 4000 volts negative, and on one occasion, to 10 kV negative during passage through eclipse. This charging resulted from an injection of energetic particles into the plasmasheet during a substorm, and because the vehicle was in eclipse, no photo-electric emissions were present to neutralize the plasma currents. It is interesting to note that most satellite anomalies at geostationary orbits occur during the satellite's passage through eclipse when satellite charging by energetic particles cannot be overcome by photo-emission [McPherson and Schober, 1976].

## Photo-electron Currents

Photo-electron currents result when energetic solar photons, with wavelengths in the ultraviolet, strike the surface of the vehicle and are absorbed. In the process of absorption, the photon releases its energy, which is then absorbed by the outer electrons in the first few angstroms of the material. If the photon energy exceeds the work function of the material, electrons can be ejected. The work function is an empirical relation determining how much energy is required to remove an electron far enough from the surface to overcome the electric field established by the removal of the electron.

Photo-emission decreases for energies in excess of 20eV. These higher energy photons can penetrate deeper into the material before releasing their energy, thus reducing the ability of an electron to reach the surface and escape. Typical photo-electron currents are ~5 x $10^{-5}$ A $m^{-2}$, which is very small compared to the electron plasma current. The Lyman-alpha emission has been shown to be responsible for up to 30% of the emitted photo-electrons for some materials [Whipple, 1981]. Photo-emission is strongly material dependent. Feuerbacher and Fitton [1972] tested the photo-emission properties of several materials and showed typical maximum yields of ~$10^{-1}$ electrons/photon at photon energies of 15 to 20 eV. They measured a photo-emission current of 2.9 x $10^{-5}$ A $m^{-2}$ for gold exposed to solar radiation. The spheres for SPEAR-1 were gold plated.

At LEO altitudes, photo-electron currents are generally of no consequence in comparison to plasma currents, and do not come into play until near geosynchronous altitudes where the plasma density is too low to provide enough return current to the vehicle to overcome the effects of photo-emission. Photo-electron currents successfully reduced ATS-5 charging to ~200 volts negative when the vehicle came out of eclipse [DeForest, 1972], while the VELA satellites, orbiting at approximately 111,000 km, were seen to charge to potentials near 100 volts positive [Montgomery et al., 1973].

Secondary Emission

In LEO, secondary emission occurs when electrons are emitted from a surface due to bombardment of the surface by energetic ions or electrons. As the electrons or ions are absorbed by the surface, they lose energy in the process of slowing down and some of this energy is transferred to the outer electrons, exciting them. Some of these excited electrons can then escape the surface. As in the case of photo-emission, secondary emission is strongly material dependent, and is also particle energy dependent. Maximum secondary electron yields occur for electron energies of ~1keV and become less than one for energies of only a few keV. A particle too low in energy will either be reflected or

absorbed by the material, but will not release enough energy to eject secondary electrons. If the energy is too high, the cross section for absorption will be too low, and the particle will penetrate too deeply before giving up its energy. The electrons released will encounter too much resistance in migrating to the surface and will not escape. In fact, the amount of secondary emission decreases exponentially with the depth of penetration of the incident particle [Whipple, 1981].

Secondary emission is most important in geosynchronous orbits where there is little ambient plasma to neutralize the secondary emissions; however, it can be important at LEO altitudes where there is an increased flux of energetic electrons, especially during solar events. Secondary emission resulting from positive ion impact produces the largest amount of charging, due to the positive charge created on the vehicle from the collection of positive ions combined with the ejection of electrons. Although not related to any processes occurring in Earth orbit, it is interesting to note that electrical charging due to secondary emission of both positive ions and electrons resulted when the GIOTTO spacecraft was bombarded by neutral particles travelling at speeds of 69 km/sec when it passed near Halley's Comet in March, 1986 [Thiemann et al., 1987].

## Induced EMF

In 1831, Michael Faraday discovered that with a closed circuit, a conductor moving relative to a magnetic field produces a current that is established by an induced electromotive force (emf) flowing through the conductor [Halliday and Resnick, 1974]. As a conductor moves through a magnetic field, Faraday's Law of Induction states that an electric field will be established. This electric field can be determined by:

$$E = -v \times B$$

where $v$ is the velocity vector

**B** is the magnetic field vector and

**E** is the electric field vector.

The potential difference between any two points separated by a distance **L** is given by:

$$V = -(v \times B) \cdot L$$

Beard and Johnson [1960] first studied this induced emf for objects in Earth orbit and found that satellites will develop potentials on the order of 0.2 V/m due to motion across geomagnetic field lines.

## Artificial Current Enhancement

Methods are possible for the artificial enhancement of currents between an object and its environment. One of the most common methods is by the intentional emission of charged particles through an electron or ion gun. Charged particle beams have been used extensively since the early days of space flight mainly to study electric and magnetic fields in the ionosphere and magnetosphere, but only recently have been used to alter the charging characteristics of space vehicles.

The basic physics of an electron gun have been known since 1881 when Thomas Edison discovered that an incandescent wire, in the presence of an external electric field and heated to high temperatures, will emit electrons [Bunshah, 1962]. An electron gun operates by heating a cathode to a high temperature so that the electrons acquire sufficient energy to overcome the work function of the material. That is, they acquire enough energy to be removed far enough from the material to overcome the potential that is established by the removal of the electrons [Leonard, 1962]. The electrons are then accelerated from the cathode by electric fields. These electrons can be focused and ejected from a space vehicle to alter its charging characteristics. Several recent experiments have been performed to assess vehicle charging characteristics during electron beam emission.

Raitt et al. [1987] showed that for LEO altitudes and electron beam currents up to 100 mA, vehicle charging is determined by a balance between emitted electron beam currents and the return current from the ionosphere. Purvis and Bartlett [1980] showed that electron beams were successfully utilized to reduce the potential on ATS-5 and ATS-6 from several thousand volts negative to several hundred volts. Below the $F_2$ region, beam-plasma interactions are important during electron beam emissions, while within the $F_2$ region and above, space-charge-limited currents are the important return currents to the vehicle during electron beam emissions [N. B. Myers et al., Vehicle charging effects during electron beam emission from the CHARGE-2 experiment, in press J. Space. Rockets, 1989]. They also showed that electron beams can successfully clamp vehicle potentials to near the ambient potential during deliberate vehicle biassing experiments.

Another device used to artificially change the magnitude of currents to a vehicle in the ionosphere is called a plasma contactor. This device causes gas to flow through a heated, hollow cathode at temperatures high enough to cause thermionic emission from the cathode surface. The electrons are then accelerated toward a keeper electrode to energies of 30 to 60 eV. These high energy electrons then ionize the relatively dense gas, and a glow discharge develops between the keeper and the cathode. This glow discharge is affected by the potential between the cathode and the undisturbed ionosphere and expands to the vehicle sheath, providing a low impedance path the the ambient ionosphere. Thus, the vehicle potential will be maintained at near zero potential relative to the environment.

Analytic Models of Current Collection by

High-Voltage Conductors

Three analytic models have been developed to study the interactions between high-voltage conductors immersed in a plasma. The earliest work in this type of study was performed by Langmuir [1913] and Langmuir and Blodgett [1923, 1924]. Their work was concerned with the study of these interactions within vacuum tubes, but with certain modifications, can be applied to present day activities in space. Since then, two other analytic models have been proposed to explain situations not addressed by the Langmuir-Blodgett model and have increased the complexity of the problem.

## Langmuir-Blodgett Model

Langmuir and Blodgett [1924] developed what has become the basis of analytic studies of high-voltage, spherical conductors exposed to a plasma. This model assumes no magnetic field is present so that electrons are free to move toward the collector from all directions. Thus, this model represents an upper limit to the current which can be collected by a high-voltage conductor immersed in a plasma. The following derivation is summarized from their paper.

In spherical coordinates, Poisson's equation (3.1) becomes:

$$\frac{1}{r^2} \frac{d}{dr}\left(r^2 \frac{dV}{dr}\right) = \frac{\rho}{\varepsilon_0} \tag{3.4}$$

where V is the potential at a distance r from the center of the sphere and

$\rho$ is the space charge density.

The total current to the sphere is given by:

$$i = 4\pi r^2 \rho v \tag{3.5}$$

where v is the electron velocity.

Neglecting initial velocities of the electrons arriving at the sheath edge, the entire kinetic energy of the electrons arises from moving through the potential field so that:

$$\frac{1}{2}mv^2 = qV \qquad (3.6)$$

where m is the electron mass and

     q is the electron charge,

or

$$v = \left(\frac{2qV}{m}\right)^{1/2} \qquad (3.7)$$

Substituting (3.7 ) into (3.5) yields:

$$\rho = \frac{i}{4\pi r^2}\left(\frac{m}{2qV}\right)^{1/2} \qquad (3.8)$$

and Equation (3.4) becomes:

$$\frac{1}{r^2}\frac{d}{dr}\left(r^2\frac{dV}{dr}\right) = \frac{i}{4\pi\varepsilon_0 r^2}\left(\frac{m}{2qV}\right)^{1/2} \qquad (3.9)$$

Langmuir and Blodgett then used a series expansion to show the final solution is of the form:

$$i = 4\pi\varepsilon_0 \frac{4\sqrt{2}}{9}\sqrt{\frac{q}{m}}\frac{V^{3/2}}{\alpha^2} \qquad (3.10)$$

where $\alpha$ is a function of the ratio of the probe radius $r_p$ to the sheath radius $r_s$.

For values of $r_s/r_p \geq 7$, they found:

$$\alpha^2 = \left(1.11 \frac{r_s}{r_p} - 1.64\right)^{3/2}$$

$$(3.11)$$

Under the assumption all particles crossing the sheath boundary are collected, then:

$$\frac{i}{i_0} = \left(\frac{r_s}{r_p}\right)^2$$

$$(3.12)$$

where $i$ is the current to the probe and

$i_0$ is the current to the probe at zero potential relative to the ambient plasma

($i_0 = 1/4 \, nqc_e A$ and $A$ is the surface area of the sphere).

Substituting (3.12) and (3.11) into (3.10), one can determine sheath size for a given potential. Then, by use of (3.12), one can determine the electron current to the probe and see that the electron current is proportional to $V^{6/7}$. The application of the Langmuir-Blodgett theory to charging of space platforms has been discussed by Beard and Johnson [1961].

## Parker-Murphy Model

Parker and Murphy [1967] went one step farther in their analysis of high-voltage, spherical conductors immersed in a plasma by taking into consideration the Earth's magnetic field.

Electrons are allowed to drift across magnetic field lines under the constraints of conservation of canonical angular momentum and particle energy. The electrons experience an $E \times B$ drift across field lines, but the drift varies as the electrons move toward the collector. They then defined a quantity $r_0$ as the maximum radial distance from the sphere that the electrons can be collected. Electrons originating at a radial distance greater than $r_0$ are dynamically forbidden from reaching the surface of the sphere

to be collected, due to the momentum and energy constraints. For a given sphere potential V, $r_0$ is defined by:

$$\left(\frac{r_0}{r_p}\right)^2 = 1 + \left(\frac{4V}{V_0}\right)^{1/2}$$ (3.13)

where V is the sphere potential in volts and

$V_0 = (m\omega^2 r_p^2) / 2q$, and $\omega = qB / m$ is the electron cyclotron frequency.

At a given potential V, the current collected will by the flux of electrons through a projected area of radius $r_0$ so that:

$$\frac{i}{i_0} = \left(\frac{r_0}{r_p}\right)^2$$ (3.14)

Equation (3.14) represents a lower limit on the current that can be collected for a given potential because the electron collection ability of the sphere is affected by the magnetic field.

## Linson Model

Linson [1969] added one additional piece of complexity to the Parker-Murphy model. For a high-voltage object, he suggests that the electron sheath surrounding the object may be sufficiently turbulent such that angular momentum and energy are not conserved, as in the Parker-Murphy model. The result is relatively easy movement of electrons across magnetic field lines to the object. He defined a quantity $q = (\omega_p/\omega_c)^2$, where $\omega_p$ is the plasma frequency and $\omega_c$ is the electron cyclotron frequency, as the critical determination of whether turbulence will be important or not. As q approaches 1, plasma waves grow fast enough to affect electron collection because the electric fields associated with the plasma waves are large enough to interact with the electrons around

the probe causing the electrons to deviate their motion. Thus, the electron collection region in the Linson model has a radius greater than $r_o$ defined by Parker-Murphy. Since q is a function of the plasma frequency, high electron densities would result in maximizing q, indicating greater turbulence and a larger current collected. Similarly, low densities result in minimizing q, leading to reduced turbulence and a smaller current.

Since the Langmuir-Blodgett model allows for no magnetic field and represents an upper limit on the current collected, and the Parker-Murphy model allows for a magnetic field but no turbulence and represents a lower limit on the current collected, one can see the Linson model is an intermediate model, with currents somewhere between Langmuir-Blodgett and Parker-Murphy. Figure 2 from Linson's paper shows the relationship between the collection areas of his model and the Parker-Murphy model. Figure 3.1 shows currents predicted by each model for potentials $\leq 45$ kV (the largest potentials used on SPEAR-1) where $n_e = 10^{12}$ m$^{-3}$, $T_e = 1000^\circ$ K, and B = 0.4 gauss.

Numerical Models of Current Collection by

High-Voltage Conductors

Numerical modelling of charged object-environment interactions is an extremely complex task requiring a considerable amount of computer memory and time. It is essential to accurately model these interactions before any deployment of an expensive, high-voltage object, such as the space station, in the LEO ionosphere.

## NASCAP - NASCAP/LEO Models

The NASA Charging Analyzer Program (NASCAP) is a three-dimensional finite element model developed to study high-voltage charging due to magnetospheric substorms [Katz et al., 1979 and Roche and Purvis, 1979]. The ambient environment is limited to those whose Debye lengths are large compared to the object dimensions, and is thus a high altitude model. The model assumes charge is collected on, rather than deposited within, dielectric surfaces. High voltages are defined as those where the potential energy (eV) is much larger than the plasma energy (kT). The NASCAP model uses a multi- step process to determine the vehicle charging:

1. The plasma environment is specified at the outer boundary. This environment can be either Maxwellian, or any user specified distribution. The direction and magnitude of incident solar radiation is specified.

2. The object is defined using a series of geometric shapes: a cube and various slices through the cube, planar square, and cylinder. The object and the space immediately around the object are divided into volume cells. Surface cells can be either bare or dielectric coated. Space around the object is set up as a series of nested grids within grids. The object is contained within the innermost grid, but protrusions from the object can extend to outer grids.

3. Particle trajectories are calculated using a known particle flux at the outer boundary and an assumed initial potential. From this, the particle flux to each surface cell is computed.

4. Solar illumination on each surface cell is determined from the known incident solar radiation.

5. The flux of backscattered, secondary, and photoemitted electrons are calculated for each surface cell from the particle and photon fluxes.

6. The net current to each surface cell is determined by the algebraic sum of the incident fluxes and the backscattered, secondary, and photoemitted electrons.

7. The potential at each grid point is calculated by solving Poisson's equation in three dimensions.

The NASCAP/LEO model [Katz et al., 1981] is an adaptation of the NASCAP model for low Earth orbit and is more approximate than the POLAR model due to the elimination of magnetic field effects. The basic workings of the model are the same as for NASCAP except that in NASCAP/LEO, the plasma Debye length is much smaller than the object size so that the model is within the space-charge-limited current regime. Also, the sheath boundary for each surface element is determined by a user defined sheath boundary potential contour, normally defined by the contour where $V = kT/q$ (V is the potential, k is the Stefan-Boltzmann constant, T is the plasma temperature, and q is the charge on an electron) and therefore uses a sharp edge sheath approximation.

## POLAR Model

The POLAR model is a three dimensional model to predict the electrical interaction between a polar-orbiting spacecraft and the ambient environment. POLAR can model vehicle charging due to the ambient plasma, energetic electrons, secondary electrons from both ion and electron impact, and photo-electrons. The model uses a circuit analogy

where the plasma around the vehicle is the current source, and the vehicle is a network of capacitors, resistors, and voltage sources [Katz and Cooke, 1984].

One major assumption of this model is that particles near the vehicle see time independent fields, so that plasma waves are neglected. The model contains several other assumptions which should be noted:

a. The ambient ions and protons are assumed to be cool, isotropic, and Maxwellian with a power law energy distribution, or hot Maxwellian with a Gaussian energy distribution, and the environment is assumed to be quasi-neutral.

b. Static electric fields and the Earth's magnetic field are the only fields of major importance, while $v \times B$ drift of electrons through conducting surfaces is the only velocity dependent field allowed. Plasma potentials are obtained from Poisson's equation with the plasma at infinity set to zero potential. Backscattered electrons and hot auroral electrons are neglected.

c. Electron densities are assumed Maxwellian with no potential barriers in the vehicle wake resulting in a wake with the maximum negative space charge possible.

d. Pre-sheath ion densities are assumed to be unaffected by electric fields so that ion motion is approximated by neutral particle motion. Thus, only collisions with other particles will alter the ion motion--there are no long range coulomb interactions with ions. The POLAR model assumes a sharp sheath edge at the 0.47 kT potential contour. Fluxes from outside the sheath are calculated analytically using orbit-limited theory. At the sheath edge, the particles are assigned trajectories which are followed through the sheath. Thermal effects within the sheath are neglected, so that all particles entering the sheath at the same point will have the same trajectories.

Since POLAR is a three dimensional model, space is divided into cubic volumes of equal size. The model solves Poisson's equation (3.3) with integrations conducted over both the surface of the object and appropriate boundaries by dividing the space into cubic volume elements, where each element contains several of the cubic volumes.

Potentials are determined at each of the eight corners of the elements and the potential

distribution within the element is trilinearly interpolated from these eight values.
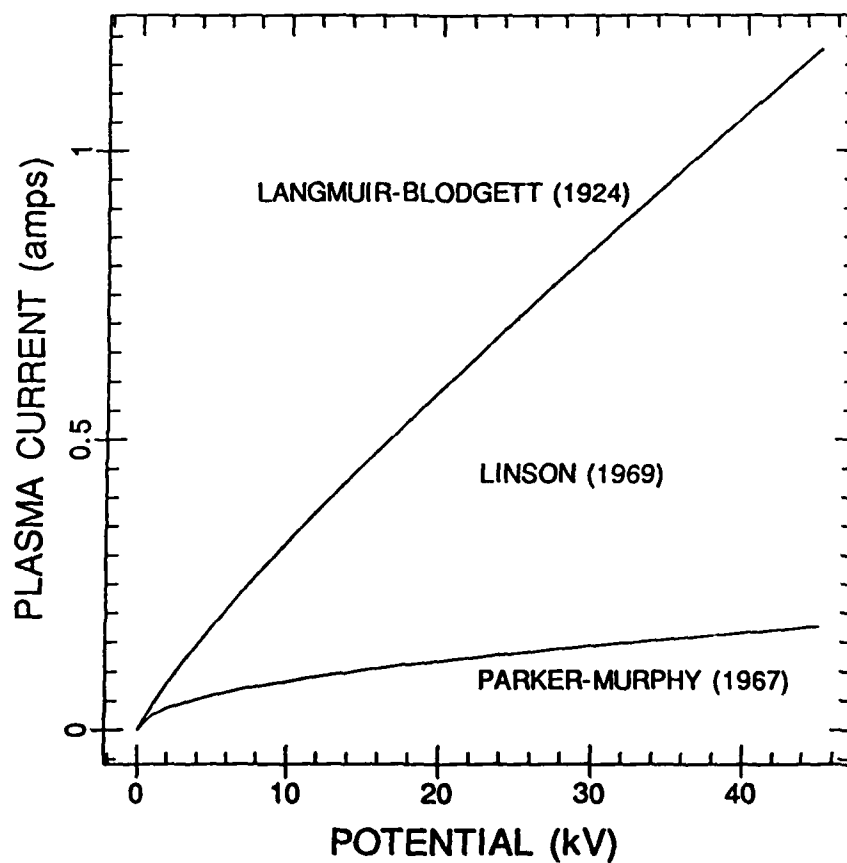
Fig. 3.1. Comparison of the three analytical models of current collection by high voltage conductors.

CHAPTER IV

THE SPEAR-1 EXPERIMENT

Much of the following preliminary information is contained in Raitt [1988] and is included here for completeness. SPEAR-1 was designed as a short time scale mission to provide measurements on the high voltage - space environment interactions. Model predictions ranged from very low current collection similar to the Parker-Murphy model to possible heavy current discharges between parts of the vehicle or to the ambient environment.

Objectives

SPEAR-1 had five specific scientific objectives:

1. "To study the altitude dependence of the current-voltage characteristics of a metallic conductor exposed to the space environment and biassed up to 10's of kV.

2. "To study the interaction of high-voltage biassed conductors within each other's charge sheaths.

3. "To make diagnostic measurements to aid the development of theoretical models to predict the current collection by conductors biassed to high voltages in the ionosphere.

4. "To study the effectiveness of a plasma contactor in grounding the power platform to the ambient ionosphere.

5. "To obtain this data in a timely fashion to be useful in the SPEAR-2 program." [Raitt, 1988, p. 1].

Relevance of SPEAR-1 to Other Platforms

The spherical geometry of the current collectors utilized on SPEAR-1 is not directly applicable to practical systems on present or planned space platforms, but was chosen because models which now predict current collection by high-voltage conductors are based on simple geometric shapes. Thus, in light of the first three objectives, these

results can be used to determine what physical processes are important in this type of interaction and be incorporated into models which can deal with more complex shapes.

## Description of Vehicle and Payload

The SPEAR-1 experiment utilized two spherical conductors biassed to potentials as high as 45 kV. The spheres were separated from the main rocket body by a fiberglass boom, with the upper portion of the boom utilizing a grading ring structure. The upper portion of the rocket body contained photometers, a low light level TV camera (LLLTV), and a neutral pressure gauge. The rest of the rocket body contained the hardware necessary to generate the high voltages, several other sensors, telemetry systems and attitude control systems (ACS), and a plasma contactor. Figure 4.1 is a schematic diagram of the SPEAR-1 payload. Figure 4.2 shows the orientation of the three instruments in the upper portion of the rocket body and the orientation of the Langmuir probe, particle detectors, and wave receivers on the vehicle. The views are both looking up the rocket body toward the spheres.

## Mission Profile

SPEAR-1 was launched on December 13, 1987 from NASA Wallops Flight Facility at 20:45 EST during conditions of fairly low solar activity. The vehicle reached an apogee of 369 km at 351 seconds into the flight. A total of 24 high voltage discharges were applied to the spheres beginning at 191.927 seconds and ending at 622.452 seconds during reentry. High-voltage biassing of the spheres was applied with the spheres in three different orientations with respect to the magnetic field. In the first orientation, beginning at 151.5 seconds, the plane of the V-shaped connecting booms to the spheres was oriented perpendicular to the magnetic field. Twelve high voltage discharges

occurred in this orientation. The second orientation, beginning at 406.6 seconds, was such that the V-shaped plane was parallel to the magnetic field and six high voltage discharges occurred in this orientation. In the third orientation, beginning at 520.2 seconds, the boom attached to sphere 1 was parallel to the magnetic field and the final six high voltage discharges took place in this orientation. Figure 4.3 shows the three vehicle attitudes with respect to the magnetic field.

## Spherical Current Collectors and Grading Rings

Two spherical conductors were utilized to study the interactions between overlapping charge sheaths. The spheres were made from aluminum, and gold plated over nickel, having a diameter of 0.2 m. The grading rings consisted of a series of shallow, saucer-shaped rings, spun from aluminum and nickel plated. The grading rings were utilized to uniformly distribute the voltage away from the spheres so that the bottom grading ring was at vehicle potential and the top grading ring was at sphere potential. The potential grading was ensured by connecting resistors between adjacent rings. The rings were oriented so that no electron fluxes accelerated toward the spheres could strike the fiberglass boom and result in additional secondary electrons being accelerated to the spheres, or result in local charging of the boom. The sphere potential was applied through a cable passing through the center of the grading ring boom and solidly potted. The grading rings for sphere 1 provided a total resistance of 1.1 $M\Omega$, and for sphere 2, a total resistance of 980 $k\Omega$. The difference in the grading ring resistance is due to the sphere 2 boom being shorter than the sphere 1 boom so that the spheres could be accommodated inside the nose cone in their stowed configuration.

## Photometers

The photometers were oriented to view the region between the two spheres with a field of view of 5° full width - half maximum. The photometers used filters with bandpasses at wavelengths of 476.5 nm, 441.5 nm, and 391.4 nm, which correspond to emissions of $Ar^+$, $O^+$, and $N_2^+$, respectively. $O^+$ and $N_2^+$ were chosen because these are the dominate atmospheric species present at flight altitude. $Ar^+$ was chosen to study possible gas buildup near the spheres from the gas released by the plasma contactor.

## Low-Light-Level TV Camera

A low-light-level TV camera (LLLTV) using a wide angle lens was mounted to view both the spheres and their charge sheaths simultaneously, and an area extending about 5 m either side of the spheres. Two light emitting diodes (LED) directed toward the spheres provided illumination during the time between high-voltage discharges. One guiding rod, attached to the vehicle to protect the spheres during nose cone ejection, blocked the view of sphere 2 during most of the flight.

## Neutral Pressure Gauge

A cold cathode ionization gauge provided measurements of neutral pressure in the pressure range of $10^{-3}$ to $10^{-7}$ torr. This type of neutral pressure gauge (NPG) works on the principle of a linear variation in a discharge current in a transverse magnetic field, which depends on the pressure. The SPEAR-1 NPG was similar in configuration to that described by Redhead [1959]. An internal power converter provided a potential difference of 2300 volts between the gauge cathode and anode, with the anode at ground potential. A magnet within the sensor traps electrons radially, while the electrons follow a hypocycloidal path around the cathode, and at the same time, oscillate in the axial direction. Electrons liberated from the cathode surface will return to the cathode unless they collide with a gas molecule. The electron will then begin its hypocycloidal orbit again and continue to have several inelastic collisions with gas molecules. After each collision, the electron will begin its motion closer to the anode. The ions created by the collision between the electrons and the gas molecules move directly to the cathode. This ion current to the cathode varies linearly with gas pressure, so that neutral gas pressure can be determined.

## High-Voltage Supply and Capacitors

The high voltages were applied to the spheres using 2.5μF capacitors charged to voltages between 6 kV and 45 kV. The capacitor voltage was determined by timing the charge-up period. During single sphere biassing, the charge-up period for sphere 2 was zero, resulting in no charge on the sphere 2 capacitor. At the end of the charging time, a discharge command was sent to both capacitors and the respective voltage was connected to the spheres, with the sphere 2 voltage being zero during single sphere biassing. The capacitors had fixed leakage resistors in parallel to ensure they were nearly completely discharged within five seconds. A circuit diagram for sphere 1 is shown in Figure 4.4. The broken line indicates those portions of the circuit which were not exposed to the space environment. All known resistances shown in Figure 4.4 were the same for both spheres except for the grading ring resistance. Figure 4.5 shows the voltage distribution between the rocket body, spheres, and the undisturbed ionosphere. Once the capacitor voltage is connected to the sphere, the three potentials will automatically adjust so that their algebraic sum will be zero, and the net current to the entire vehicle is zero.

## Langmuir Probe

SPEAR-1 utilized a cylindrical Langmuir probe deployed radially from the rocket body, with a total collection area of about 0.001 $m^2$, to measure the ambient plasma environment. The probe swept from +5 volts to -1 volt and back again over a one second period which repeated every 2.3 seconds. Electron currents to the probe could be measured between $10^{-10}$ amps and $5 \times 10^{-5}$ amps. Probe data was only available between high-voltage discharges.

## Wave Receivers

Electric field measurements up to 30 kHz were measured on a single axis by two spheres deployed radially one meter from the payload. Sphere to skin and sphere to

sphere voltages were monitored with varying bandwidths up to 20 kHz, while the full VLF signal was monitored from 20 Hz to 30 Hz.

## Particle Detectors

Four imaging ion and electron detectors monitored charged particle fluxes in the energy ranges 2 eV to 5 keV and 10 eV to 30 keV in several different view directions with a 32 ms time resolution. Higher energy bandwidths were about 11% while lower energy bandwidths were approximately 20%. The particle detectors were utilized to determine the ion flux to the rocket body. The low energy detectors were used to measure ion fluxes while the plasma contactor was operational, and the high energy detectors were used to measure ion fluxes should the plasma contactor fail.

### Plasma contactor

A hollow cathode plasma contactor was utilized to clamp the vehicle potential to 100 to 150 volts negative when the high voltage was applied to the spheres. The operating gas was argon. The plasma contactor failed due to the failure of the cover plate to be ejected at third stage separation. Had the plasma contactor worked properly, V(2) in Figure 4.5 would have been approximately zero so that the full charged capacitor potential would have been applied to the sphere. Because the plasma source was never exposed to the ambient environment, the rocket body charged to potentials as high as several thousand volts negative during the high voltage discharges.
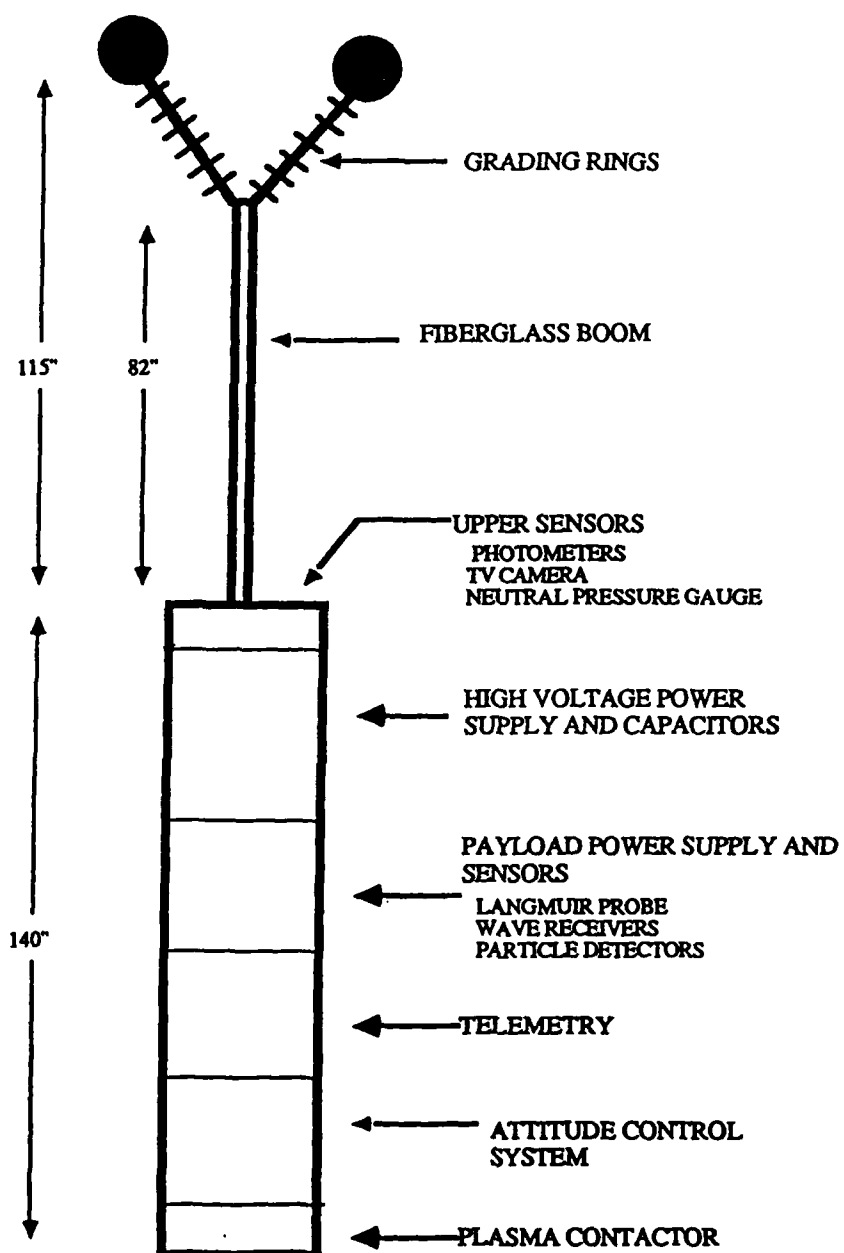
Fig. 4.1. Schematic diagram of the vehicle payload showing the locations of the instruments used on SPEAR-1.
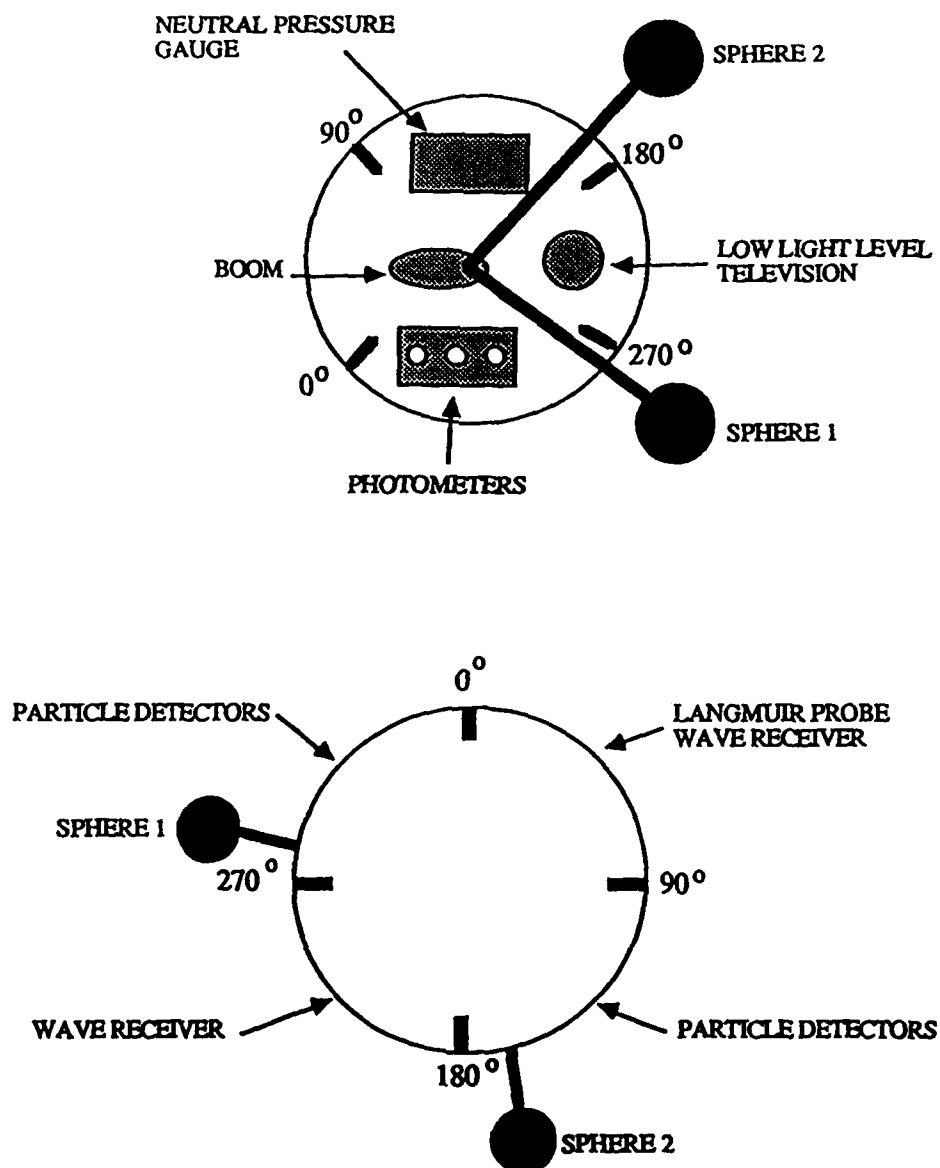
Fig. 4.2. Schematic cross section diagram of the SPEAR-1 vehicle showing the locations of the three instruments in the upper portion of the rocket body (upper diagram) and the locations of the other instruments on the rear portion of the rocket body (lower diagram).
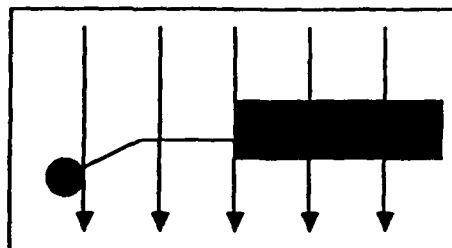
V-PLANE PERPENDICULAR
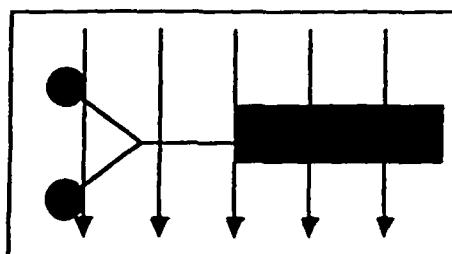


V-PLANE PARALLEL
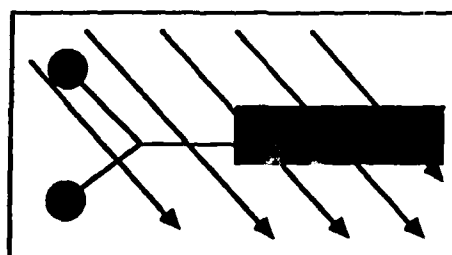


SPHERE 1 BOOM PARALLEL

Fig. 4.3. Schematic diagrams of the three vehicle orientations with respect to the earth's magnetic field.

Fig. 4.4. Circuit diagram for sphere 1.

■ = EXPOSED TO UNDISTURBED IONOSPHERE

CHARGED CAPACITOR
VOLTAGE V(1)

VOLTAGE BETWEEN PAYLOAD
AND UNDISTURBED
IONOSPHERE V(2)

VOLTAGE BETWEEN SPHERE
AND UNDISTURBED
IONOSPHERE V(3)

UNDISTURBED IONOSPHERE
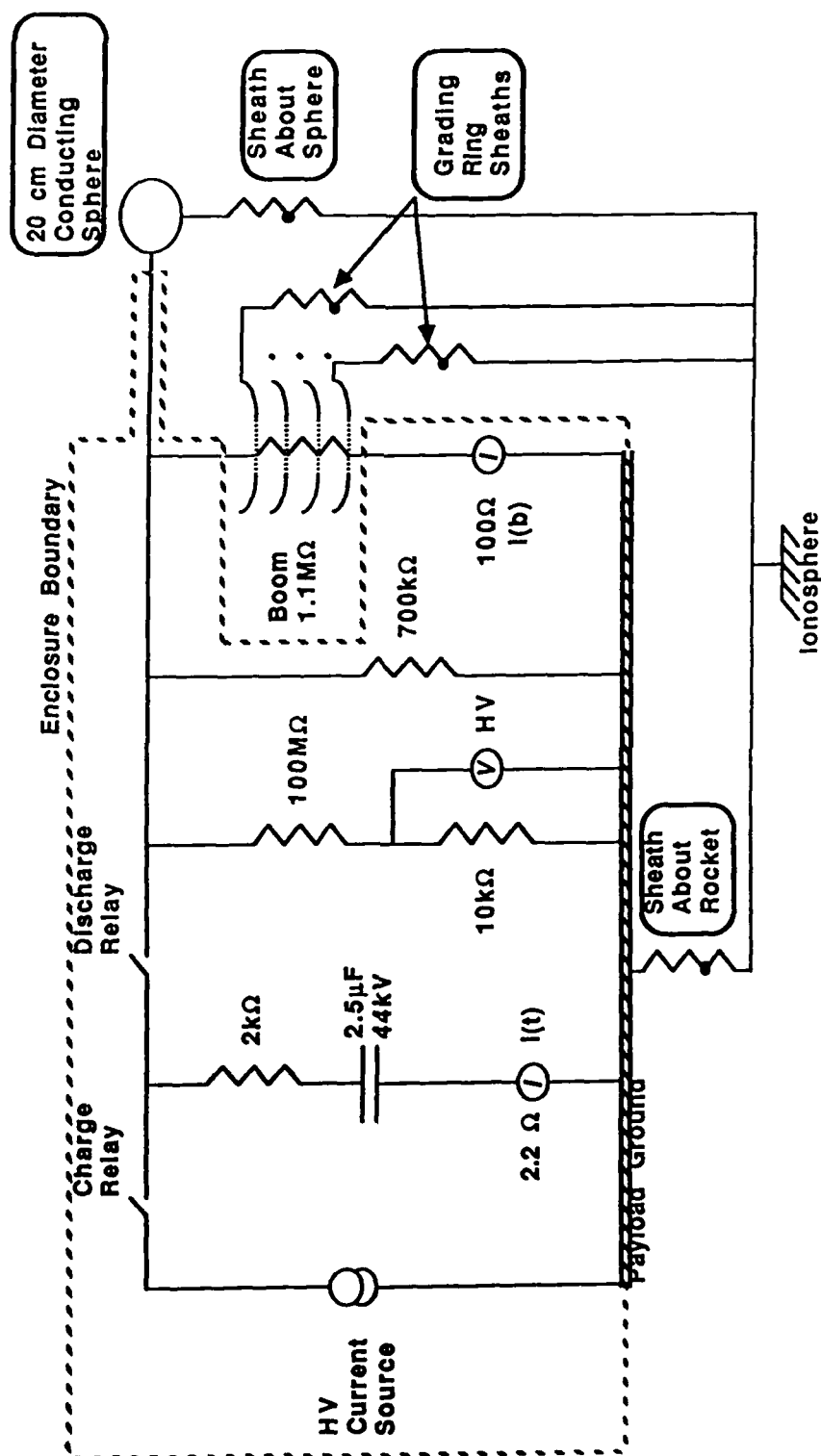
VOLTAGE DISTRIBUTION WILL BE SUCH
THAT V(1) + V(2) + V(3) = 0
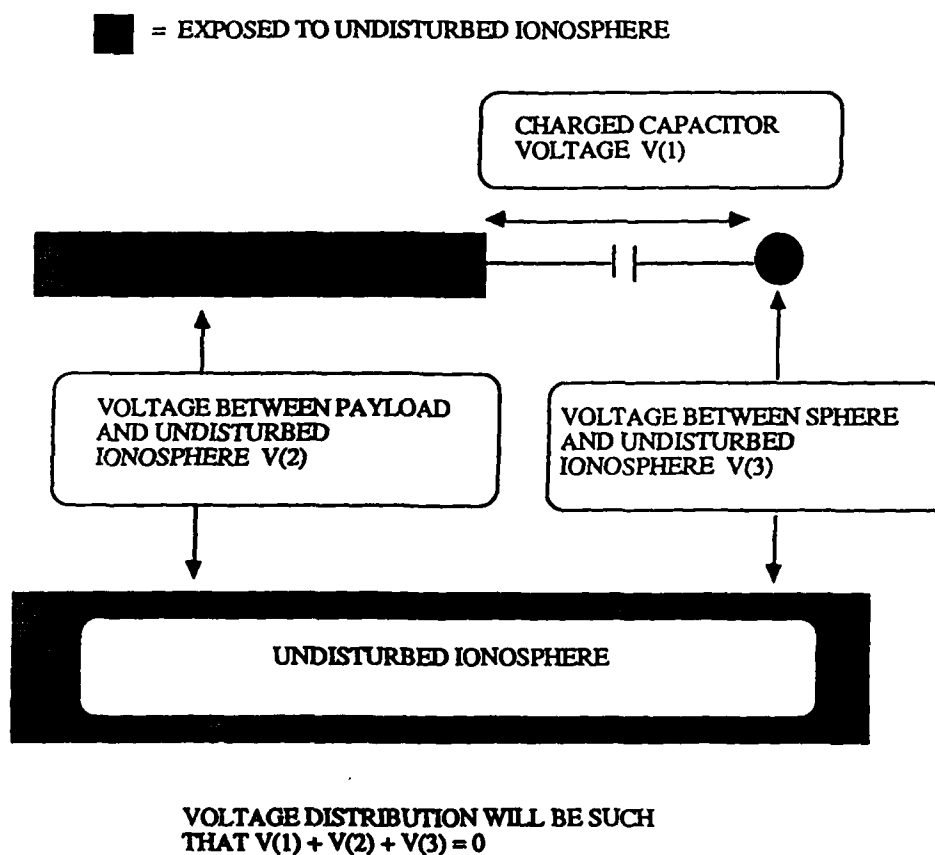
Fig. 4.5.  Schematic diagram showing the voltage distributions across the SPEAR-1 vehicle.

# CHAPTER V

## EXPERIMENT TO STUDY HIGH-VOLTAGE INTERACTIONS IN THE IONOSPHERE

### Measured vs. Modelled Ambient Neutral Environment

When applying high voltages to the ambient LEO environment, there is the possibility for unwanted discharges resulting from the establishment of electric fields. The most important parameters to consider as a result of this possibility are the neutral pressure, the plasma density, and the geomagnetic field. As stated earlier, SPEAR-1 utilized a cold cathode ionization gauge to determine the neutral pressure at the instrument location. Figure 5.1 shows a comparison between the measured neutral pressure and the pressure predicted by the MSIS-86 model [Pickett, private communication 1988]. The input parameters for the MSIS model were: previous day's $F_{10.7}$ flux = 91.5; average $F_{10.7}$ flux for the previous three months = 93.6; and the daily $A_p$ index = 4 [Coffey, 1988]. The most important feature to note is that the measured pressures are three to four orders of magnitude above the model pressures. This difference can be attributed to outgassing from the instrument, the rocket body, and the fiberglass boom due to the instrument location inside the forward portion of the rocket body, adjacent to the fiberglass boom. The initial decrease in the gauge pressure resulted from outgassing of the ionization chamber initiating the cold cathode discharge. At approximately 300 seconds, the pressure decreases with an approximate $t^{-1}$ time dependence, which is characteristic of an outgassing object. Late in the flight, the atmospheric pressure became greater than the outgas pressure and the detector then recorded the ambient atmospheric pressure.

In order to use these measured pressures to estimate the pressure at the spheres, we can assume the pressure at the spheres is reduced by an inverse square relationship from the measured pressure, since the mean free path of the outgas is much greater than the size of the payload. Since the spheres are separated approximately 3 m from the rocket body , this assumption would yield ambient pressures at the spheres on the order of $5 \times 10^{-8}$ torr, which is consistent with the MSIS model predictions [Raitt, 1988].

## Measured vs. Modelled Ambient Plasma
## Environment

Figure 5.2 shows a comparison between the measured and modelled electron density and Figure 5.3 shows a comparison for the electron temperature. Langmuir probe data was unavailable during high-voltage biassing of the spheres due to the failure of the plasma contactor and the resulting high negative potentials of the rocket body. Gaps in the temperature and density profiles occur where probe data was eliminated for this reason. The electron densities can be divided into an upleg and downleg portion. Because of the ACS maneuvers necessary in the downleg portion, the Langmuir probe was in the vehicle wake. Thus, the upleg data is probably more representative of the actual conditions. The modelled parameters were derived from the IRI model, with the 12-month running mean of the Zurich sunspot number equal to 26 [Hand, private communication 1988]. Figure 5.4c shows a typical current-voltage sweep for the cylindrical Langmuir probe used on SPEAR-1. An idealized Langmuir probe sweep can be divided into four regions. In the first region, the electron current collected is negligible because the probe is biassed negative, preventing almost all electron current from reaching the probe. The second region begins to show a transition to a measurable electron current. The third region shows an exponential increase in the electron current collected with increasing voltage. This region is used to determine the electron

temperature. The fourth region shows an electron current saturation and is used to determine electron density [Hok et al., 1956]. These four regions have been indicated on Figure 5.4c.

The electron temperature measurements were first determined for each probe sweep which was not within one second before to ten seconds after a high-voltage discharge. This was to prevent any possibility of data contamination due to the high-voltage discharge. The linear portion of the sweep was isolated (Figure 5.4b), and the slope of the best fit line was determined using a least squares fit to the data. The temperature was then calculated from:

$$T = \frac{q}{kS}$$

where q is the electron charge,

    k is the *Stefan-Boltzmann constant*, and

    S is the slope of the line

[Mott-Smith and Langmuir, 1926].

Once the temperature for each sweep was determined, then the electron density could be determined from the saturation current. One can readily see from Figure 5.4c that in reality, the electron current never saturated for this sweep and in fact, never did so for any sweep. Therefore, to determine the saturation current, the average of the currents for probe potentials greater than +4.5 volts was taken, and this value was used as the saturation current (Figure 5.4a). The electron density could then be calculated from:

$$Ne = \frac{4\,i}{qcA}$$

where i is the saturation current,

q is the electron charge,

c is the mean electron speed for a Maxwellian distribution, and

A is the probe collection area.

Not all Langmuir probe sweeps were as smooth as that shown in Figure 5.4. Figure 5.5 shows two probe sweeps which will result in a larger density and temperature errors than that shown in Figure 5.4. The Langmuir probe data show a peak electron density of approximately $6 \times 10^{11}$ m$^{-3}$ at about 240 km altitude, while the electron temperature remains at about 500 - 600° K throughout most of the flight. The mean density error is $10^{11}$ m$^{-3}$ and the mean temperature error is 164° K.

Though the measured electron temperature is much lower than the IRI model predictions, the temperatures are consistent with the fact that the measured electron densities are higher than the model densities. The high electron temperatures measured below about 200 km are completely unexpected when compared to the nearly isothermal temperatures measured above 200 km. There must be some mechanism dumping energy into the lower altitudes of the ionosphere to account for the unexpectedly high temperatures. There was a solar flare recorded the day before the SPEAR-1 flight, but the effects from a flare would not be expected to be seen except in the auroral regions. The temperatures could be explained by Joule heating due to the electrojets, but the SPEAR-1 flight was at too low a latitude for the auroral electrojet and too high a latitude for the equatorial electrojet. Instrumental errors can be ruled out because the measured errors are totally consistent with the errors measured throughout the rest of the flight, and the probe sweeps were as smooth as the sweep shown in Figure 5.4. No definitive explanation can be provided for these unexpected temperatures.

Measured Current-Voltage Characteristics

Figure 5.6 shows a comparison between the currents measured directly on SPEAR-1 (total current and boom current) and the derived plasma current. The voltage is the potential difference between the rocket body and the sphere. The total current is the sum of the current flowing through all fixed resistors in Figure 4.4, the electron current to the spheres and grading rings, and the ion current to the rocket body. The boom current is the current flowing through the boom connecting the sphere to the main boom, and the plasma current is the total plasma current collected by the representative sphere and the rocket body. Had the plasma contactor worked properly, the rocket body would have been near the ambient potential, and the full charged capacitor potential would have been applied to the sphere. However, due to the failure of the plasma contactor and the resulting negative charging of the rocket body, the actual voltage applied to a sphere is up to several kilovolts less than the charged capacitor voltage. In single sphere biassing operations, the measured potential on sphere 2 was zero, indicating that sphere 2 had charged to up to several kilovolts negative along with the rocket body.

The total plasma current was derived by taking the measured total current ($I(t)$ in Figure 4.4) and subtracting all known currents, with any remaining current being the plasma current collected. For sphere 1 the plasma current was determined in the following manner: the total resistance between the charged capacitor and the sphere was determined by:

$$\frac{1}{R_t} = \frac{1}{100\ \text{M}\Omega + 10\ \text{k}\Omega} + \frac{1}{700\ \text{k}\Omega} + \frac{1}{1.1\ \text{M}\Omega}$$

so that $R_t = 426\ \text{k}\Omega$ for sphere 1. For sphere 2, $R_t = 407\ \text{k}\Omega$. Therefore, the known current at any charged capacitor voltage $V$ is given by:

$$I_{known} = \frac{V}{R_t}$$

and the plasma current is given by:

$$I_{plasma} = I(t) - I_{known}$$

## Discussion of Results

All high-voltage discharges to the spheres were accompanied by a glow enveloping a significant portion of the grading rings. This glow decayed from the lower grading ring, in the direction of the spheres, so that all glow had disappeared within a few hundredths of a second after the discharge. Figures 5.7a, 5.7b, and 5.7c all show a video image acquired just before, or during, a high-voltage discharge. In Figure 5.7a, the spheres were illuminated by the LEDs. In Figure5.7b, the LEDs had switched off just prior to a discharge. In Figure 5.7c, the high voltage had been applied to sphere 1, and the glow around the grading rings is readily apparent. The lack of any other glow except in the vicinity of the grading rings suggests a local ionization effect, rather than a large volume breakdown. This glow is probably the result of ionization resulting from outgassing of the grading rings, as the glow was not seen except in the immediate vicinity of the grading rings.

### General Discussion of Current-Voltage Curves

Figures 5.8 through 5.15 show the current-voltage characteristics for all 24 discharges. The equation shown with each figure is the equation of the best fit line through the data using a least squares fit. One can readily see from Figures 5.8 through 5.15 that nearly all current-voltage curves are approximately linear, indicating that in

most cases, sheath resistance is fairly constant with voltage. However, there are some notable exceptions which must be addressed.

1. Discharge 1 shows three current enhancements. These three enhancements appeared on the video images as brief bursts of light around the grading rings after the initial glow had disappeared. This enhancement is presumably the result of grading ring outgassing increasing the local pressure enough to result in ionization of the neutral gas by the electrons streaming in toward the grading rings.

2. Discharge 3 shows a dramatic example of a non-constant sheath resistance as the voltage drops below approximately 10 kV. A close inspection of the current-voltage plots shows that during most of the discharges, the sheath resistance changes below approximately 10 kV, as evidenced by a slight curvature in the current-voltage plot. This curvature is most pronounced on sphere 2 during discharges 3, 5, 9, and 11, when the spheres were in the V-plane perpendicular orientation and both spheres were biassed. Note also that little effect was seen on sphere 1 in these three cases. A possible mechanism for this curvature will be discussed in a later section.

3. Discharges 6, 12, and 18 all exhibit a current enhancement near the maximum capacitor voltage, which corresponds to the beginning of the discharge. These cases will also be discussed in a later section.

4. Discharges 13 and 19 are examples when ACS activity was occurring at the same time the spheres were biassed. These cases will be discussed in a later section.

## Current-Voltage Characteristics with respect to Altitude and Electron Density

Figure 5.16 shows a plot of sheath resistance versus altitude and electron density for those high voltage discharges where only sphere 1 was biassed, and applied potentials were greater than about 15 kV. Single sphere biassing was chosen to eliminate any sphere 1-sphere 2 sheath interactions from contaminating the data. Potentials greater

than 15 kV were chosen because sphere potentials less than this value were all in the curvature portion of the current-voltage plot described earlier and resulted in sheath resistance anomalies. Over the altitude range shown in the figure, the electron density remained fairly uniform. One would expect that as the electron density increased, the sheath resistance would decrease because the sheath size necessary to collect enough electrons to balance the potential on the sphere would also decrease. As a result of the uniformity of the electron densities; therefore, no definante trend can be seen in the sheath resistance in either plot. The lowest sheath resistance of about 610 k$\Omega$ occurred at 263 km altitude, which is also the altitude of maximum electron density for these seven discharges. However, with only very limited data over this limited range of electron densities, no conclusive results can be made as to how the current-voltage characteristics vary with altitude and electron density. High-voltage discharges need to be made over a larger density range.

## Current-Voltage Characteristics with respect to Magnetic Field Orientation

Table 5.1 shows a comparison between the sheath resistances in the V-plane perpendicular orientation and the V-plane parallel orientation for those discharges where the applied potential and altitude were approximately equal. All sphere 1 sheath resistances were less in the parallel orientation anywhere from about 100 k$\Omega$ to 1000 k$\Omega$. Discharge 13 occurred during ACS activity, so that the measured sheath resistances are probably significantly less than what would have occurred had ACS activity not been occurring. Eliminating discharge 7 and 13, the sphere 1 sheath resistances are between 100 k$\Omega$ and 250 k$\Omega$ less in the V-plane parallel orientation. The sphere 2 sheath resistance is less in the parallel orientation only during discharge 13. Again, part of this is the result of ACS activity. The sphere 2 sheath resistance is significantly larger in the parallel orientation during discharge 15 than during either discharge 3 or 9. Due to this

TABLE 5.1. Comparison of Sheath Resistances for Sphere 1 and 2 ($R_1$ and $R_2$) between the V-plane Perpendicular to B and V-plane Parallel to B Cases. $R_1$ and $R_2$ are in k$\Omega$.

| Perpendicular | | | | Parallel | | | |
|---|---|---|---|---|---|---|---|
| ALT | Discharge | $R_1$ | $R_2$ | ALT | Discharge | $R_1$ | $R_2$ |
| 303 | 3 | 927 | 5915 | 325 | 15 | 676 | 19877 |
| 321 | 4 | 977 | | 307 | 16 | 866 | |
| 359 | 7 | 2116 | 2611 | 352 | 13 | 1153 | 1797 (ACS) |
| 365 | 9 | 852 | 5530 | 325 | 15 | 676 | 19877 |

significant difference, it is difficult to explain what is causing the much larger sphere 2 sheath resistances during discharge 15 without a numerical model to determine the three-dimensional shape of the respective charge sheaths.

It is clear from these data that there is a magnetic field orientation dependence on the current collection capabilities of SPEAR-1, with the V-plane parallel orientation providing the easiest current collection. With no numerical model output available to precisely predict the shape of the charge sheaths, one can only speculate as to the cause of the difference. Under conditions of no magnetic field with both spheres charged simultaneously, there should be a slight elongation of the total sheath around both spheres along the axis between the spheres. Upon introduction of a magnetic field, this elongation would be greater if the axis between the spheres was parallel to the magnetic field, making the axis of elongation of the total charge sheath parallel to the magnetic field, also. As a result, there would be less **E x B** drifting across field lines and the spheres could collect more current from directly parallel to the field lines.

Since a single sphere does not change orientation with respect to the magnetic field, the resistances during single sphere biassing should be equal. However, there must be some interaction occurring between the single sphere and the rocket body/sphere 2 sheaths to provide a lower current collection capability in the V-plane parallel

62

orientation. To explain the reduced single sheath resistances in this orientation, a numerical analysis of the sheaths would be required.

Current-Voltage Characteristics during ACS Activity

During two instances in the flight, considerable ACS activity occurred when a vehicle reorientation maneuver was not quite completed before the high-voltage discharges were sent to the spheres. This resulted in a significant enhancement of the collected plasma current . At times, minor ACS activity occurred during a discharge to maintain the vehicle in the proper orientation which also resulted in current enhancements. On one instance, the enhanced current collected was approximately 0.16 amps--10 to 15 times greater than the current collected when the ACS jets were not firing. Figure 5.17 shows a comparison between capacitor voltage versus time, and plasma current versus time both for a non-ACS case and an ACS case. In both cases, the exponential decay in voltage, characteristic of a discharging capacitor, is readily apparent. The non-ACS case also shows the expected exponential decay in the plasma current. However, the plasma current for the ACS case shows a large number of current spikes, each occurring at the time of an ACS gas release.

Figure 5.18 shows a comparison between ACS activity (represented as NOZZLE FIRE voltages) and enhanced plasma currents for discharges 13 and 19. It is apparent from these diagrams that there is a strong correlation between ACS activity and enhanced current collection. As an example of the mechanism resulting in the reduced impedance between the SPEAR-1 active system and the ambient ionosphere, focus on the first ACS jet firing illustrated in the lower two panels of Figure 5.18. This ACS gas release corresponds to the 0.16 amp current enhancement.

The NOZZLE FIRE voltage output obtained from the ACS telemetry indicates which ACS jet or combination of jets was firing at a particular time. The 2 volt output indicated a yaw jet was firing, but not which yaw jet was operating. Figure 5.19 is a

schematic diagram looking up the rocket body toward the spheres, showing the orientation of the ACS jets with respect to the spheres and the main fiberglass boom. Analysis of the video data indicated that it was the yaw jet indicated in bold face that was firing at the time of the 0.16 amp current enhancement. Figure 5.20a is a picture from the LLLTV just prior to the ACS jet firing. The glow distributed down the grading rings is present at the beginning of all high voltage discharges to the spheres. Note that the main fiberglass boom is only dimly lit by ambient light from the ground and the airglow layer. Figure 5.20b is an image obtained during the firing of the ACS jet. It is readily apparent that there is an enhanced glow distributed down the grading rings, indicating that a higher voltage and therefore more ionization is present. Note that the boom is now brightly lit, with the light source coming from above, as evidenced by the lower portion of the boom appearing to be in shadow. This is consistent with the yaw jet identified in Figure 5.19 as being the active jet at the time the image was acquired.

As noted previously, the plasma contactor failed, with the result that the rocket body charged to up to several kilovolts negative during the high voltage biassing of the spheres. Therefore, one can conclude that this glow is the result of ionization of the neutral gas emitted by the ACS jets, by the energetic positive ions streaming toward the rocket body. This ionization then acts as a plasma contactor in providing the low impedance path to the ambient ionosphere. Thus, the sheath resistance of the rocket body fell from hundreds of kilo-ohms to near zero, resulting in a corresponding increase in the electron current collected. Results from the CHARGE-2 sounding rocket flight also show a strong correlation between ACS activity and enhanced current collection during biassing operations [N. B. Myers et al., Vehicle charging effects during electron beam emission from the CHARGE 2 experiment, in press J. Space. Rockets, 1989].

Characteristics of a Possible Volume Breakdown

Discharges 6, 12, and 18 all exhibit characteristics of a volume breakdown of the neutral gas in the vicinity of the sphere 1. The characteristic feature is a current enhancement at the beginning of the discharges when the applied potentials were maximized. In each of these cases, the video images showed a diffuse glow moving from the grading rings toward the connection point between the sphere booms and the primary support boom. The glow corresponding to discharge 6 was very dim, and nearly undetectable. Each subsequent glow was brighter, with the final glow being relatively bright and easily detected in the images. The current-voltage curve for discharge 6 showed only a minimal, short duration enhancement, with the curve for the final glow (discharge 18) showing the largest and longest duration enhancement. Figure 5.21a shows a LLLTV image just prior to the appearance of the diffuse glow on discharge 18, and Figure 5.21b shows the glow near the connecting point of the sphere booms to the main boom. This type of glow and current enhancement only appeared during single sphere biassing at potentials greater than 40kV, suggesting a minimal volume breakdown in the vicinity of the spheres caused by ionization of the neutral gases by the incoming electrons. The third event occurred at an altitude of 263 km, which is near the maximum in electron density.

Charged-Particle Flux and Vehicle Charging

Figure 5.22 shows two plots of ion energy versus ion flux measured approximately one second apart during discharge 12 [Torbert and Larson, private communication 1988]. The view of the ion spectrometer was $34°$ from the geomagnetic field direction. The ion energy cutoff has moved to a lower energy during this time, consistent with the capacitor discharge. Although the energy cutoff has a fairly broad peak, it is clear the rocket body must have been at a potential of several kilovolts negative in order to achieve current balance between the ion current collected by the rocket body

and the electron current collected by the sphere/grading rings. The energy flux above the cutoff energy is the result of secondary ion emission caused by the primary ions striking the rocket body.

Figure 5.23 shows the relationship between the capacitor potential and sphere potential as a function of time for discharge 12, and the sphere current - sphere voltage diagram for sphere 1. Sphere 1 potential was determined by subtracting the rocket body potential from the charged capacitor potential. This potential clearly shows the same decay time constant as the capacitor, indicating no other charging mechanisms occurred on the rocket body other than that due to the failure of the plasma contactor.

The upper panel clearly shows a linear variation in the sphere current as the sphere potential decreases, consistent with the data already presented. The sheath resistance around sphere 1 was 628 k$\Omega$, which is a large percentage of the 713 k$\Omega$ total sheath resistance shown in the current-voltage plot for discharge 12. This result would be expected if the rocket body sheath had nearly enclosed the sphere sheath.

Characteristics of Charge Sheath Interactions

Apparent interactions, or lack thereof, between the charge sheaths when both spheres are biassed can be seen on most current-voltage diagrams. When the sphere 1 potential was greater than the sphere 2 potential, an inflection in the sphere 2 diagram occurs at a potential of approximately 4000 volts on discharges 3, 5, 9, 11, and 21. This inflection indicates the occurrence of a possible decoupling of both the sphere charge sheaths and the sphere 2/rocket body charge sheaths. As a result, the current collection ability of sphere 2 is no longer affected by the sheath on sphere 1 or the rocket body. Therefore, sphere 2 can collect larger amounts of current for a given potential. The charge sheath coupling is evidenced by a much smaller sheath resistance for sphere 1 than for sphere 2, over the range from 1400 k$\Omega$ to 5000 k$\Omega$. This would indicate that the

sheaths around sphere 1 and the rocket body have possibly partially encircled sphere 2, so that the sphere 2 sheath is not as well exposed to the ambient environment.

When the sphere 2 potential was greater than the sphere 1 potential, as in discharges 1 and 7, the difference in the sheath resistance is 400 k$\Omega$ to 500 k$\Omega$, obviously much smaller than during discharges 3, 5, 9, 11, and 21. Since it has been shown that in general, the current collected varies linearly with potential, i.e. sheath resistance is constant with increasing potential, charge sheaths which are not coupled should show approximately the same sheath resistance. Thus, one can conclude that the charge sheaths in these cases were only weakly coupled; each operated nearly independently of the other. A numerical analysis of the charge sheaths is necessary to accurately predict the three dimensional shape of the sheaths. Such an analysis would determine the reason for the weakly coupled sheaths in a sphere 2 potential greater than sphere 1 potential configuration.

In cases where only sphere 1 was biassed, a pronounced curvature in the current-voltage plot below about 10 kV occurs during discharges 6, 12, 14, and 18. This is presumably a result of the decoupling of the charge sheath around the rocket and sphere 2, and the sheath around sphere 1. At a capacitor potential of approximately 10kV, the rocket body potential should be only on the order of -2 kV, leaving 8 kV of potential on the sphere. Thus, it is possible the charge sheath around the rocket body and sphere 2 is of a negligible size, when compared to the sphere 1 sheath, and what is being seen is an actual current-voltage plot of the sphere potential to the sphere current. This would represent a nearly unipolar model, similar to the analytical models discussed previoulsy.

## Current-Voltage Characteristics Compared with Analytical Models

The three analytical models presented earlier are valid only for cases in which there is a single, simple geometrically shaped conductor at high voltages, so that the

charge sheath around the object will have a simple geometric shape. Had the plasma contactor worked properly, the negative potential around the vehicle body would have been negligible, when compared to the potential on the spheres, so that the rocket body charge sheath could be ignored. In that case, the experiment would have been nearly unipolar during all two sphere biassing operations, and completely unipolar during all single sphere biassing operations. This would have allowed more direct comparisons with the analytical models. However, since the plasma contactor failed and the rocket body charged to up to several kilovolts negative during biassing operations, a unipolar experiment was not achieved, except during some ACS activity. Therefore, a direct comparison between the analytical models and the actual results cannot be made except in the ACS cases. However, making some comparison during the non-ACS cases with these limitations in mind will provide some important information.

Figure 5.24 shows discharge number 12 compared with the Langmuir-Blodgett and Parker-Murphy models. It is apparent that below 18 to 20 kV, the plasma currents collected are at, or just below, the Parker-Murphy predicted currents. Above this potential range, the plasma currents collected lie between the Langmuir-Blodgett and Parker-Murphy predictions, as would be predicted by the Linson model. The Linson parameter q is determined by:

$$q = \frac{n_c m_e}{\epsilon_0 B^2}$$

where $n_e$ is the electron density in the electron sheath around the object,

$\epsilon_0$ is the electrical permitivity constant,

$m_e$ is the electron mass, and

B is the magnetic field strength.

By inserting the constants and assuming a magnetic field of 0.4 gauss, the Linson parameter can be determined by:

$$q = 6.4 \times 10^{-11} \, n_e$$

Next, making the assumption that the electron density inside the charge sheath is equal to the ambient density, one finds that $q = 18.6$ for discharge 12. This indicates that plasma turbulence should provide more cross magnetic field motion than only the $\mathbf{E} \times \mathbf{B}$ drift motion invoked by the Parker-Murphy model (in reality, the electron density in the charge sheath will be somewhat lower than the ambient density, but this should provide an approximate estimate of the value for q). That this is indeed the case is indicated by the larger amounts of current collected. In fact, in all instances of single sphere biassing, the Linson parameter was $\gg 1$, indicating plasma turbulence is important in determining the current-voltage characteristics. In almost all single sphere biassing cases, the data lies between the Langmuir-Blodgett and Parker-Murphy models, as would be predicted by the Linson model.

Figure 5.25 shows the variation of the Linson parameter as a function of sheath resistance, normalized by the Langmuir-Blodgett sheath resistance. The latter being determined by a straight line fit through the Langmuir-Blodgett data. The data show a trend of a larger Linson parameter (indicating more turbulence) yielding larger sheath resistances (Langmuir-Blodgett becoming less and less accurate as a predictor and Parker-Murphy becoming more accurate). This is exactly the opposite of what would be predicted by the Linson model. More turbulence should yield a lower sheath resistance, as electrons are easily collected across magnetic field lines--in other words, more turbulence should yield predictions closer to the Langmuir-Blodgett model. Therefore, there must be effects not addressed by the Linson model which are important in determining the current collection characteristics of high voltage conductors. It would be interesting to see if the data exhibit the same trends during an actual unipolar case, or if this is the result only in this bipolar case when there are interactions between charge sheaths.

As stated earlier, only during ACS activity was a near unipolar experiment achieved which would allow a more direct comparison with the analytical models. Figure 5.26a shows the ACS enhanced currents for discharge 13 (sphere 2) relative to the Langmuir-Blodgett and Parker-Murphy models. Except for the larger enhancement at about 4000 volts, it is apparent that these current enhancements closely follow the Parker-Murphy model. Figure 5.26b shows the same comparison during discharge 19. Below about 11 kV, the data closely follow the Parker-Murphy model while at higher potentials, the data approach the Langmuir-Blodgett model. In both of these cases, spheres 1 and 2 were biassed, resulting in a more complicated shape to the charge sheath. However, since the sphere 2 potential was much larger than the sphere 1 potential, the sphere 2 charge sheath should dominate the current collection, and these results are probably fairly reasonable.

On four other occasions, ACS activity resulted in current enhancements: discharge 4 at about 12 kV, discharge 8 at about 7 kV, discharge 9 at about 4 kV, and discharge 15 at about 14.5 kV. These ACS firings were short duration firings to maintain the vehicle in the proper orientation. A scatter plot of sphere potential versus sphere current, normalized by the Parker-Murphy predictions, is shown in Figure 5.26c for all six ACS cases noted above. The points labelled 4, 8, 9, and 15 are the single ACS firings during the respective discharges. The data show a tendency above approximately 12 kV for the sphere currents to be larger than the Parker-Murphy predictions, and below approximately 15 kV for sphere currents to be at or somewhat below Parker-Murphy predictions. Therefore, it appears that the 12 to 15 kV range is the cross-over potential where plasma turbulence begins to dominate the current collection capabilities of high-voltage conductors. It is possible; however, that this plasma turbulence is greater than would be achieved in a truly unipolar experiment, due to the continuing expansion and contraction of the sphere and rocket body charge sheaths as the ACS jets fired off and on. Results from the CHARGE-2 experiment in which a conductor was biassed to potentials

up to 450 volts, showed that the current collected was also very closely predicted by the Parker-Murphy model [N. B. Myers at al., A comparison of current-voltage relationships of collectors in the Earth's ionosphere with and without electron beam emission, in press Geophys. Res. Lett., 1989].

In all six of these cases, the Linson parameter >> 1, assuming the ambient electron density is an accurate measurement of the density within the electron charge sheath. This indicates that plasma turbulence should provide significant cross magnetic field motion of electrons and provide a current significantly larger than the Parker-Murphy prediction at all potentials. The data clearly show this is not the case and that some parameterization of potential should also be included.

These data contain two possible sources of error that need to be addressed. First, as stated earlier, these examples are not truly unipolar since both spheres were biassed, except for discharges 4 and 8 where only sphere 1 was biassed. Secondly, the current spikes were all single measurement spikes, resulting in some uncertainty as to how accurate a representation of the true current they are. However, even considering these possible errors, the data is very consistent in its behavior above and below the 12 to 15 kV cross-over potential, indicating that these results are physically reasonable.

Numerical Model Results from SPEAR-1

Katz et al. [1989] studied the bipolar charge sheath on SPEAR-1 using both the NASCAP/LEO and the POLAR models. They confined their study to a single sphere biassed to potentials at high as 46 kV with the Earth's magnetic field perpendicular to the plane of the V-shaped booms. This potential and orientation corresponds to the configuration for discharge 12. The ionospheric plasma parameters used as input were: $N_e = 5 \times 10^{10}$ m$^{-3}$, $T_e = 1000^\circ$K, B = 0.4 gauss. Both model calculations showed that an ion collecting sheath was formed around the rocket body and an electron collecting

sheath surrounded the sphere. But, because the surface area of the rocket body was so much larger than that for the sphere, the ion sheath nearly cut off the electron sheath.

Based on the work of Dietz and Sheffield [1975], Katz et al. (1989) postulated that each incoming $O^+$ ion would produce over 10 secondary electrons upon striking the aluminum rocket body, because of the high negative voltages acquired by the rocket body. The secondary electrons would dominate the current flowing to the rocket body; however, due to the much greater mobility of electrons over ions, the secondary electrons would rapidly be accelerated out of the rocket body sheath and the $O^+$ ions would dominate the space charge. Secondary electrons were accelerated along magnetic field lines but acquired too much momentum to be collected by the spheres. All current calculations from the NASCAP/LEO and POLAR models took the ion and secondary electron currents into account.

Under these conditions, both NASCAP/LEO and POLAR computations derived a rocket body potential of -8.3 kV when the sphere was biassed to 46 kV. This is consistent with the conclusion based on the ion spectrometer data that the rocket body charged to several kilovolts negative during discharge 12, with an applied voltage of 45320 volts. Under these same conditions, the models predicted plasma currents of 45 to 50 mA for a 46 kV sphere bias, which again is reasonably consistent with the data.

Table 5.2 shows a comparison between the biassed voltage and the NASCAP/LEO calculated plasma current for the case when the plane of the V-shaped booms was perpendicular to the magnetic field. A straight line fit through the NASCAP/LEO data from Table 5.2 results in a sheath resistance of 985 k$\Omega$. This sheath resistance compares favorably with that calculated during discharges 2, 4, and 10, all of which had applied potentials of less than 26 kV. Discharges 6, 8, and 12 all showed sheath resistances of at least 100 k$\Omega$ less than the NASCAP/LEO calculation. Part of this discrepancy for discharge 8 could be a result of local ionization spikes seen in the data.

TABLE 5.2. NASCAP/LEO Calculated Plasma Currents
[Adapted from Katz et al., 1989]

| Bias voltage (kV) | NASCAP/LEO current (amps) |
|---|---|
| +46 | .045 |
| +24 | .027 |
| +12 | .013 |
| + 1 | .001 |

However, for discharges 6 and 12, the discrepancy is not so readily apparent. The flight data showed a sheath resistance of 825 k$\Omega$ and 713 k$\Omega$ respectively, both of which are within the estimated 30% uncertainty of the calculations. However, because these are right at the edge of the uncertainty in the calculations, one must speculate if some process is occurring at these 44 to 45 kV potentials that the NASCAP/LEO model cannot adequately treat. Since the NASCAP/LEO model does not take into account either plasma turbulence or waves, it is possible plasma turbulence is responsible for the additional cross-magnetic field motion of electrons toward the sphere, and should be considered when studying NASCAP/LEO calculations for this high of applied potentials.

In general, computed results from the NASCAP/LEO and POLAR models compared favorably with the flight data, showing that the models can adequately account for the physics involved in a high-voltage system such as SPEAR-1.
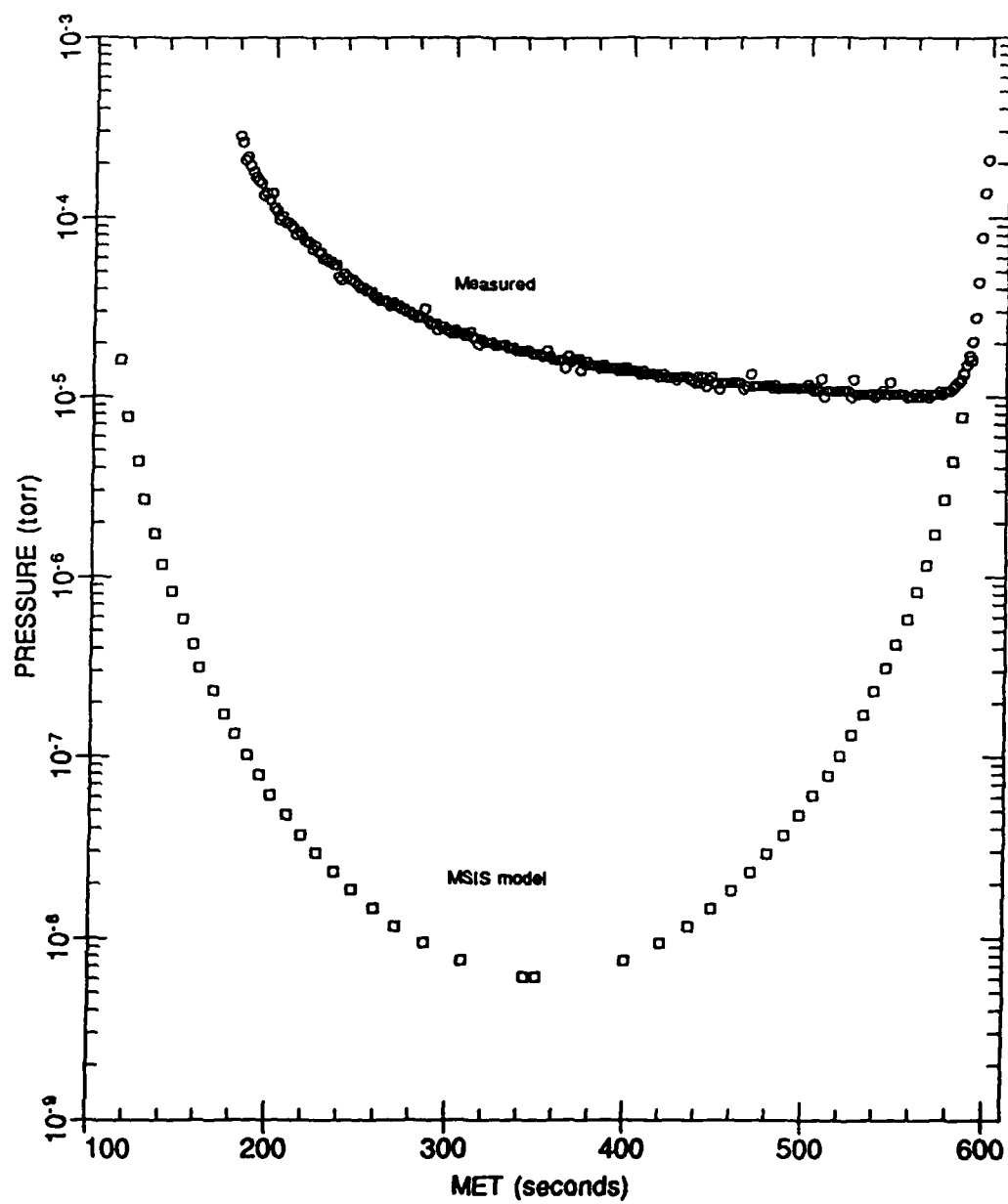
Fig. 5.1.  Comparison between the neutral pressure measured by the SPEAR-1 neutral pressure gauge and the MSIS-86 modelled pressures.
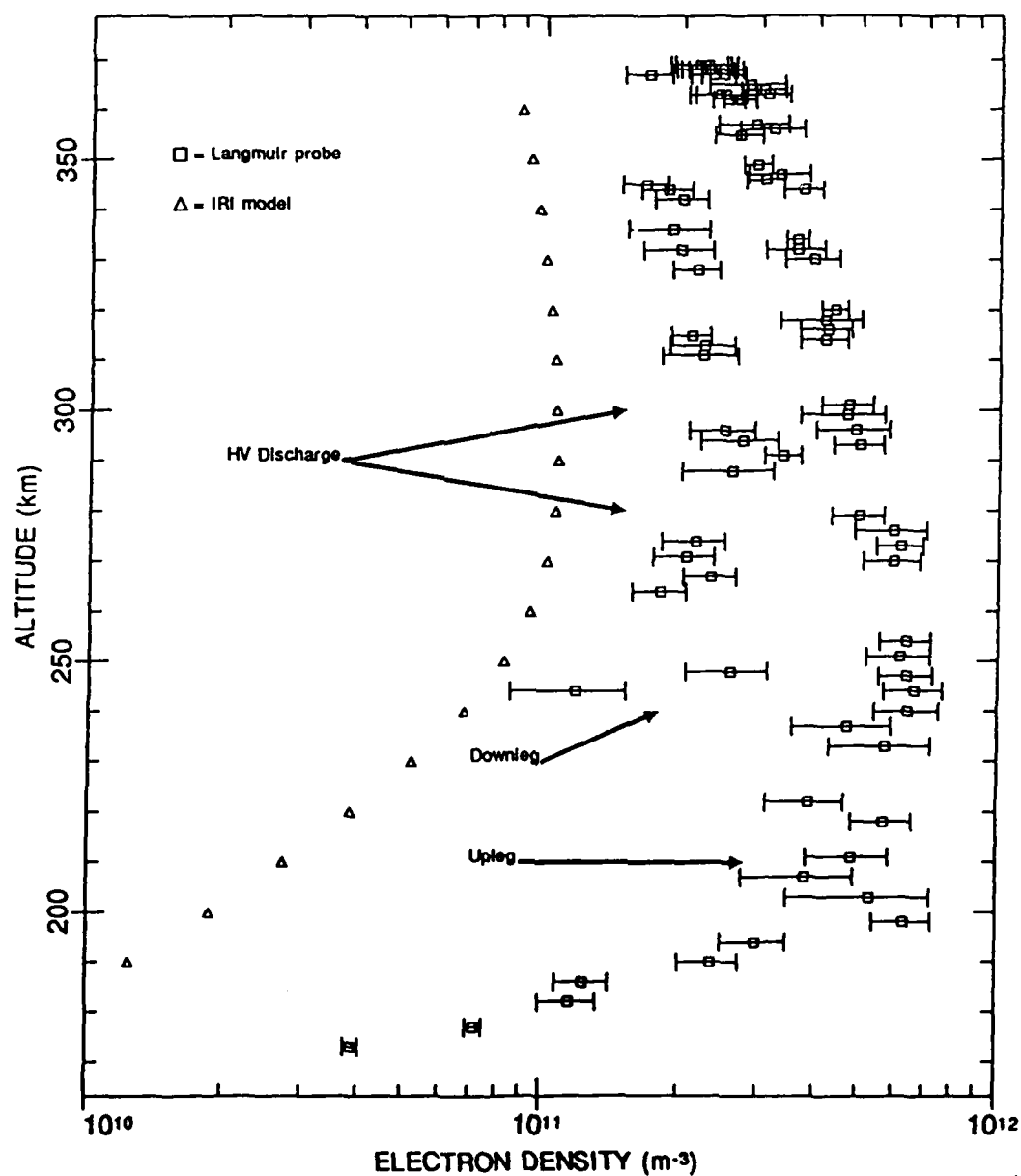
Fig. 5.2. Comparison between electron densities measured by the SPEAR-1 Langmuir probe and the IRI modelled densities.
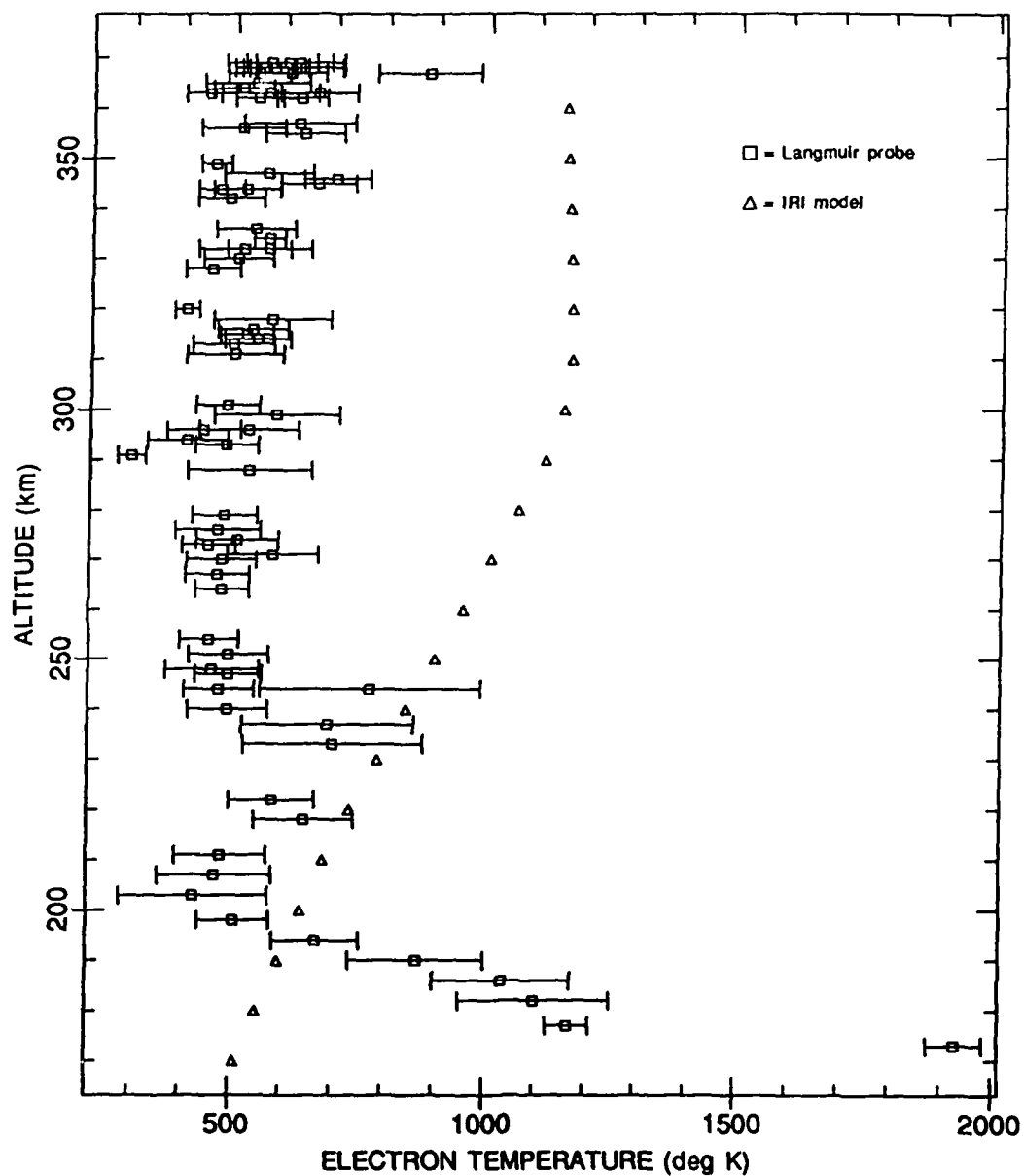
Fig. 5.3. Comparison between electron temperatures measured by the
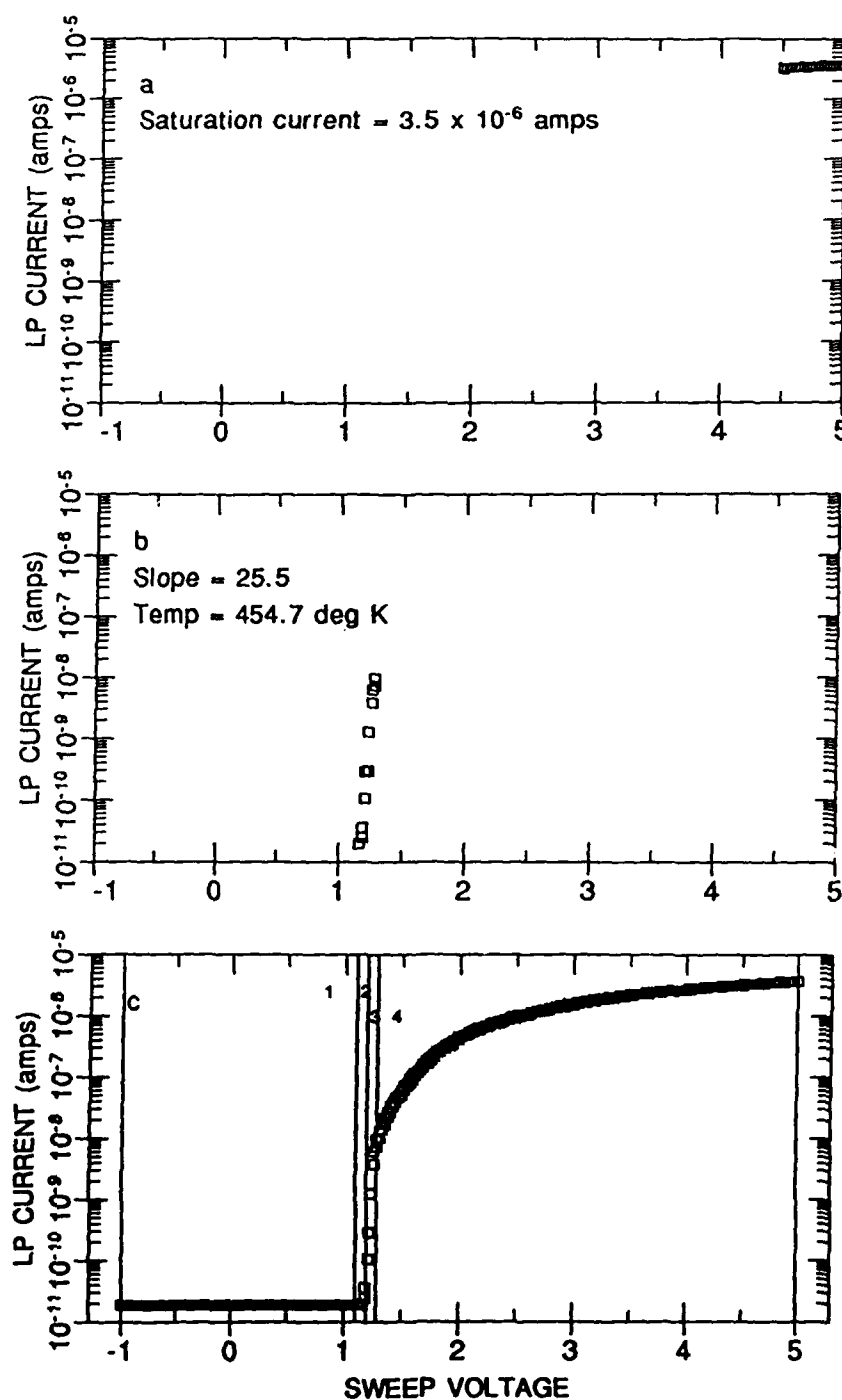SPEAR-1 Langmuir probe and the IRI modelled temperatures.

a

Saturation current = 3.5 x 10⁻⁶ amps

b

Slope = 25.5

Temp = 454.7 deg K

c

1 2 3 4

SWEEP VOLTAGE

Fig. 5.4. Langmuir probe data from sweep 22 (245 km) showing data used to calculate (a) electron density and (b) electron temperature. (c) shows the entire sweep, including the 4 regions typically seen in a Langmuir probe sweep.
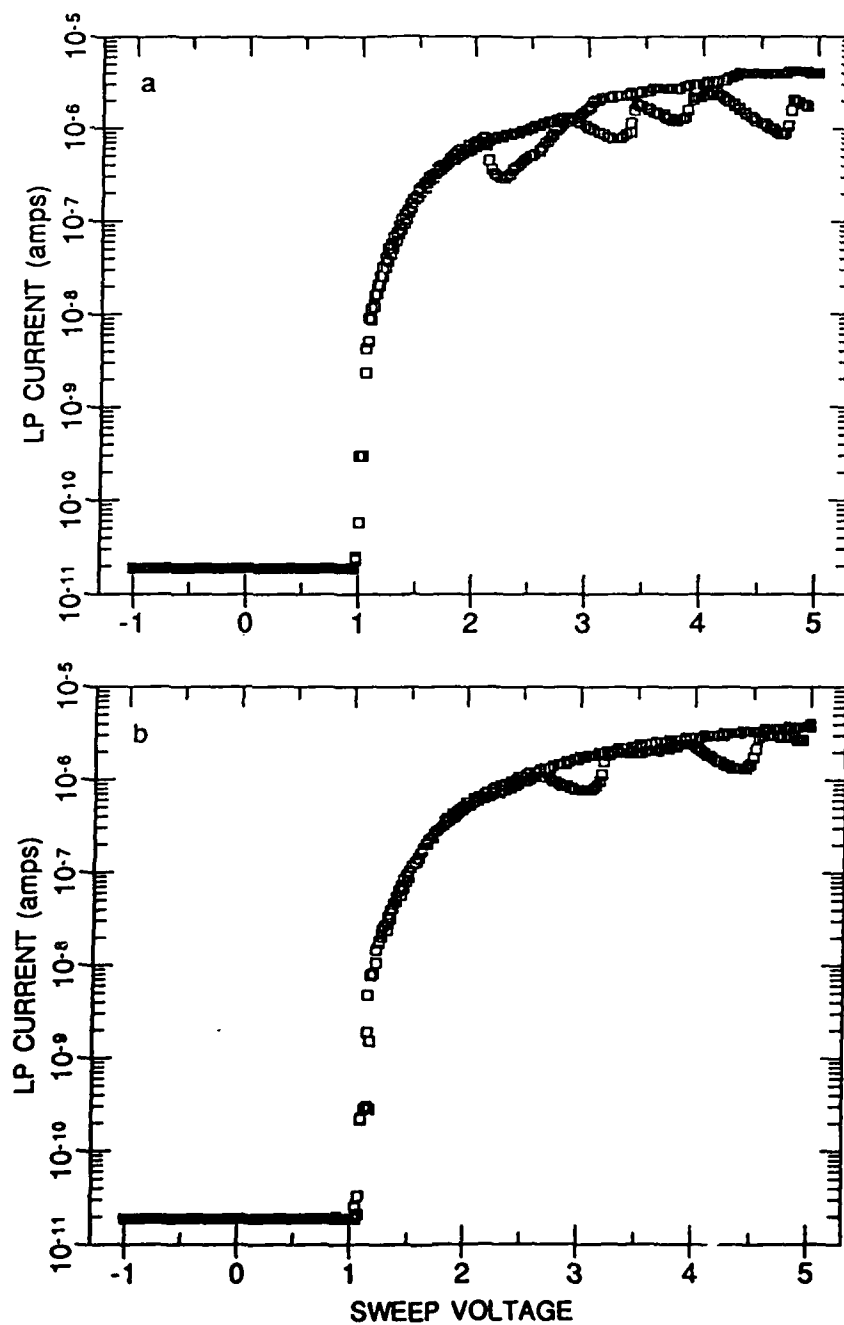
Fig. 5.5 Langmuir probe data showing two sweeps which resulted in larger temperature and density errors. (a) is from sweep 13 (222 km) and (b) is from sweep 17 (237 km).
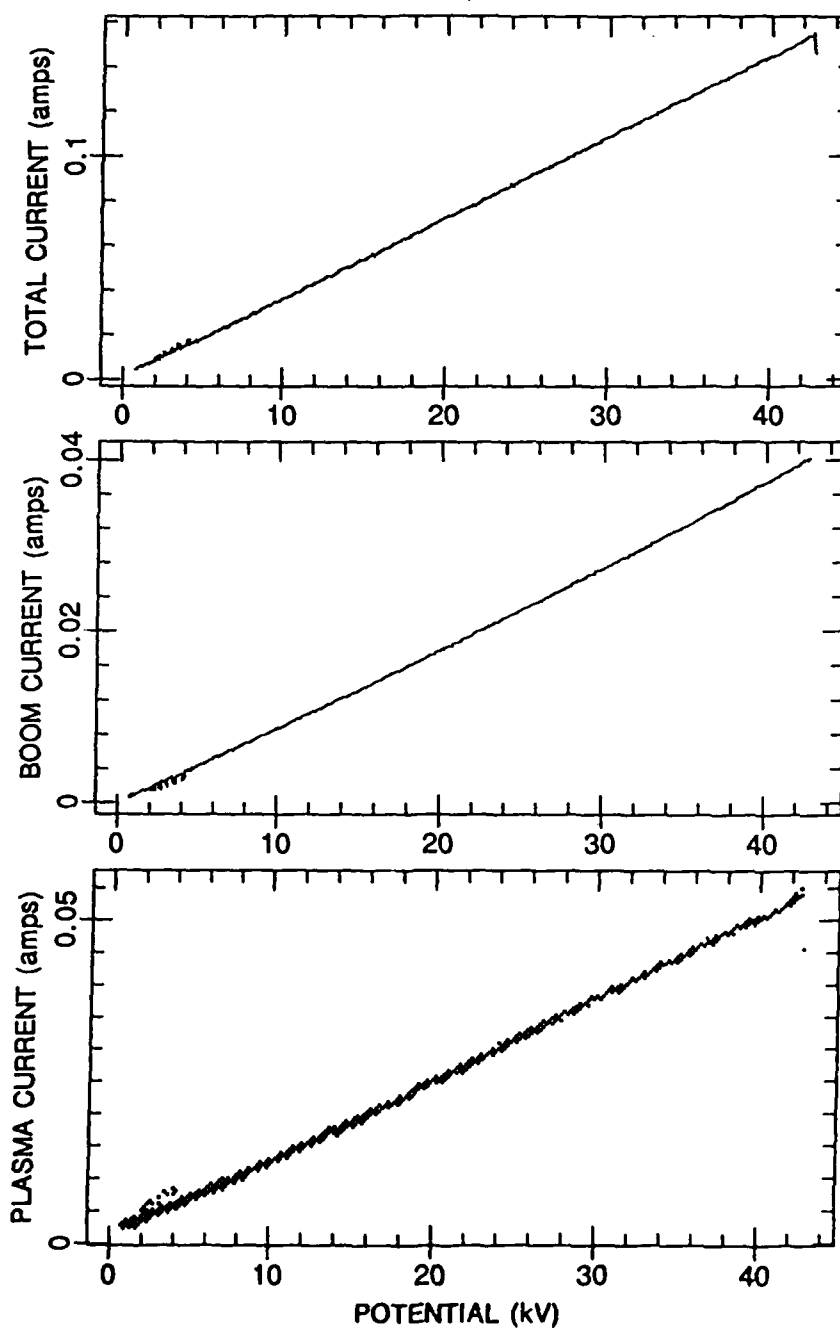
Fig. 5.6. Comparison between currents directly measured on SPEAR-1 (total current and boom current) and the derived plasma current.
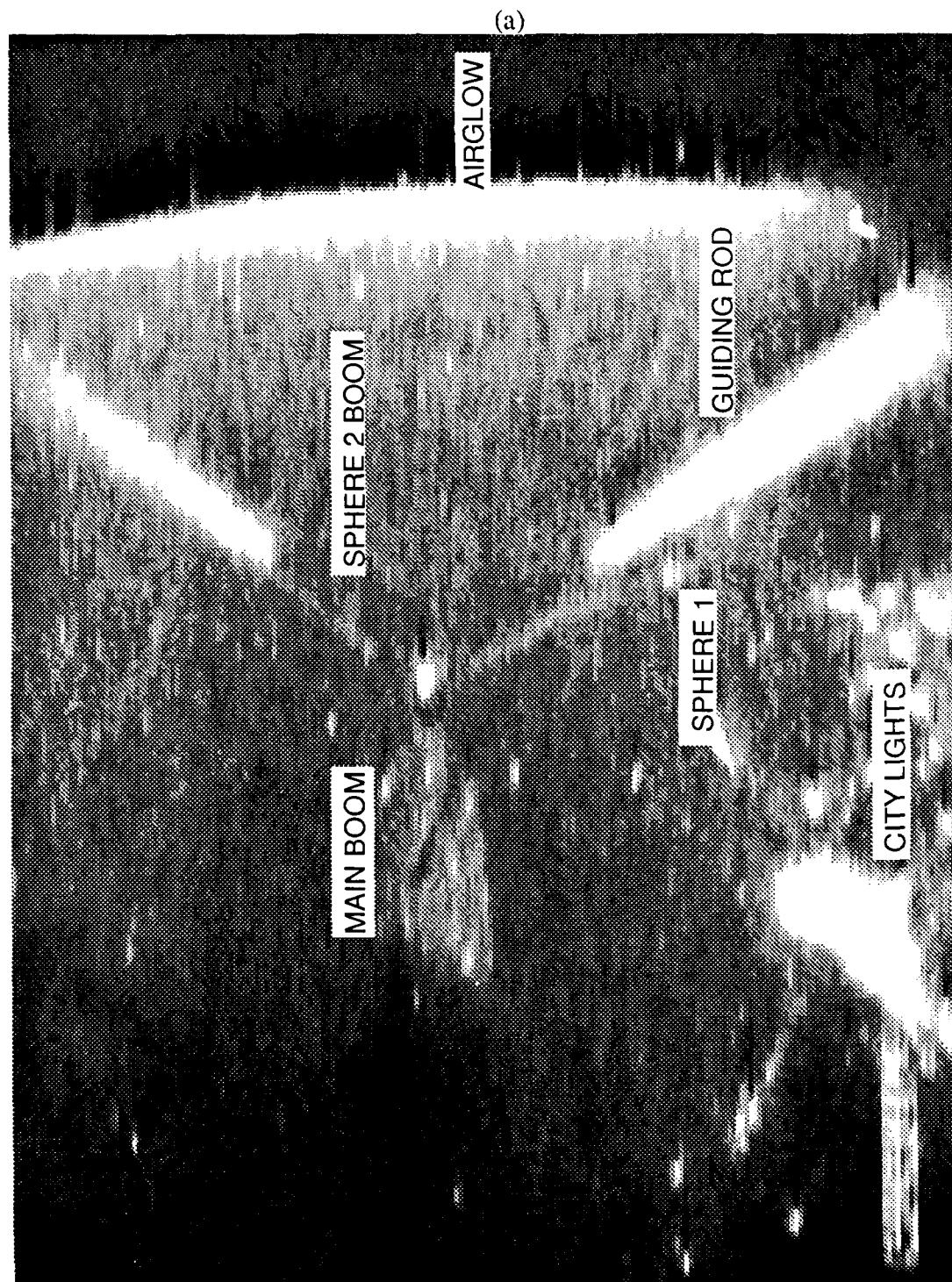
Fig. 5.7. SPEAR-1 low light level TV picture (a) just prior to discharge 3 with the scene illuminated by the LEDs, (b) just prior to discharge 3 with no LED illumination, and (c) during discharge 3. Glow around sphere 1 boom is readily visible.
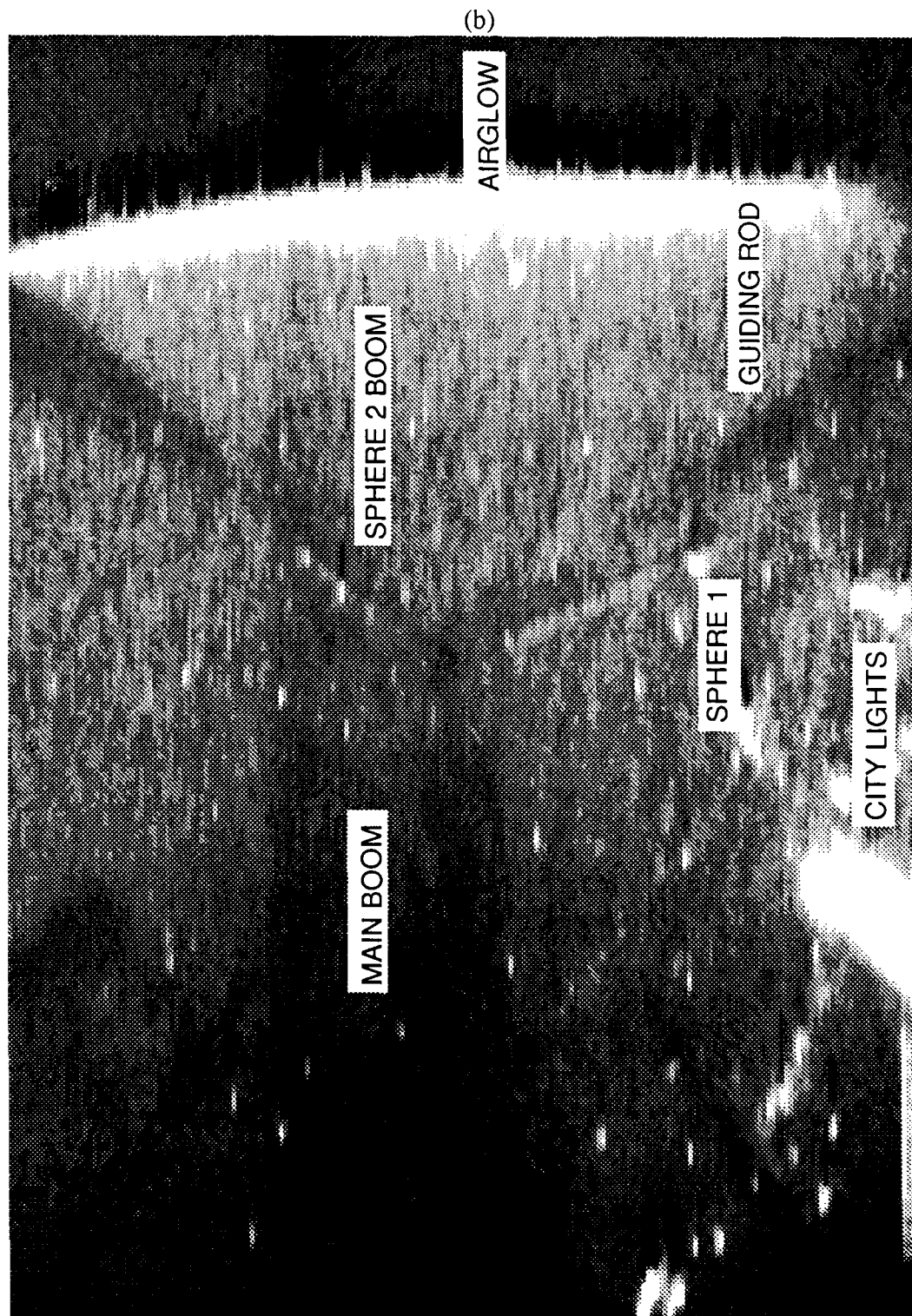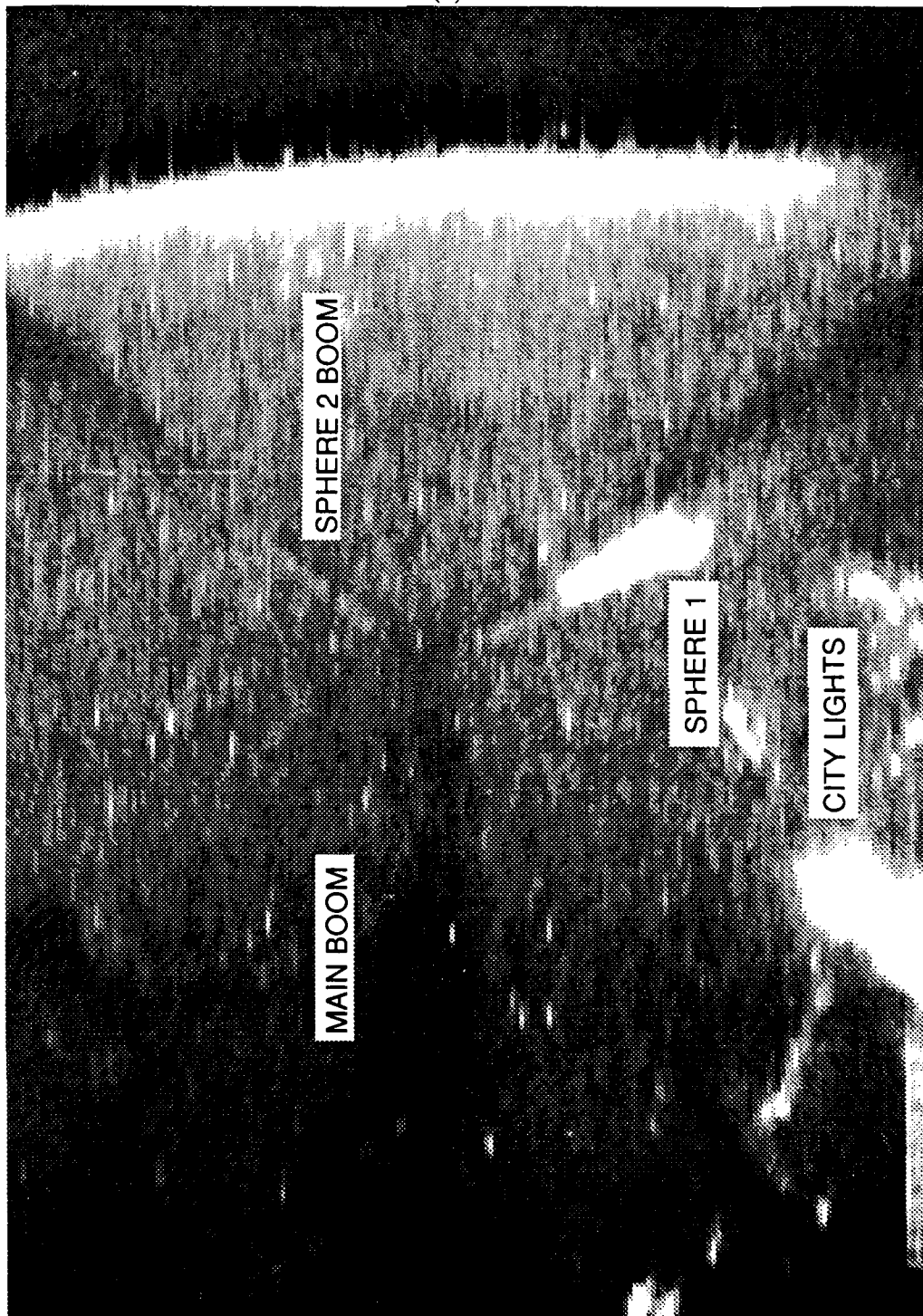
(b)



Fig. 5.7. Continued.

(c)



Fig. 5.7. Continued.

SPHERE 1

SPHERE 2

**a**

V(kV) = 2351I(A)

ALT = 257 km
MET = 192 s

**b**

V(kV) = 1922I(A)

**c**

V(kV) = 973I(A)

ALT = 285 km
MET = 211 s

SPHERE 2 UNBIASSED

**d**

V(kV) = 927I(A)

ALT = 303 km
MET = 230 s

**e**

V(kV) = 5915I(A)

PLASMA CURRENT (amps)
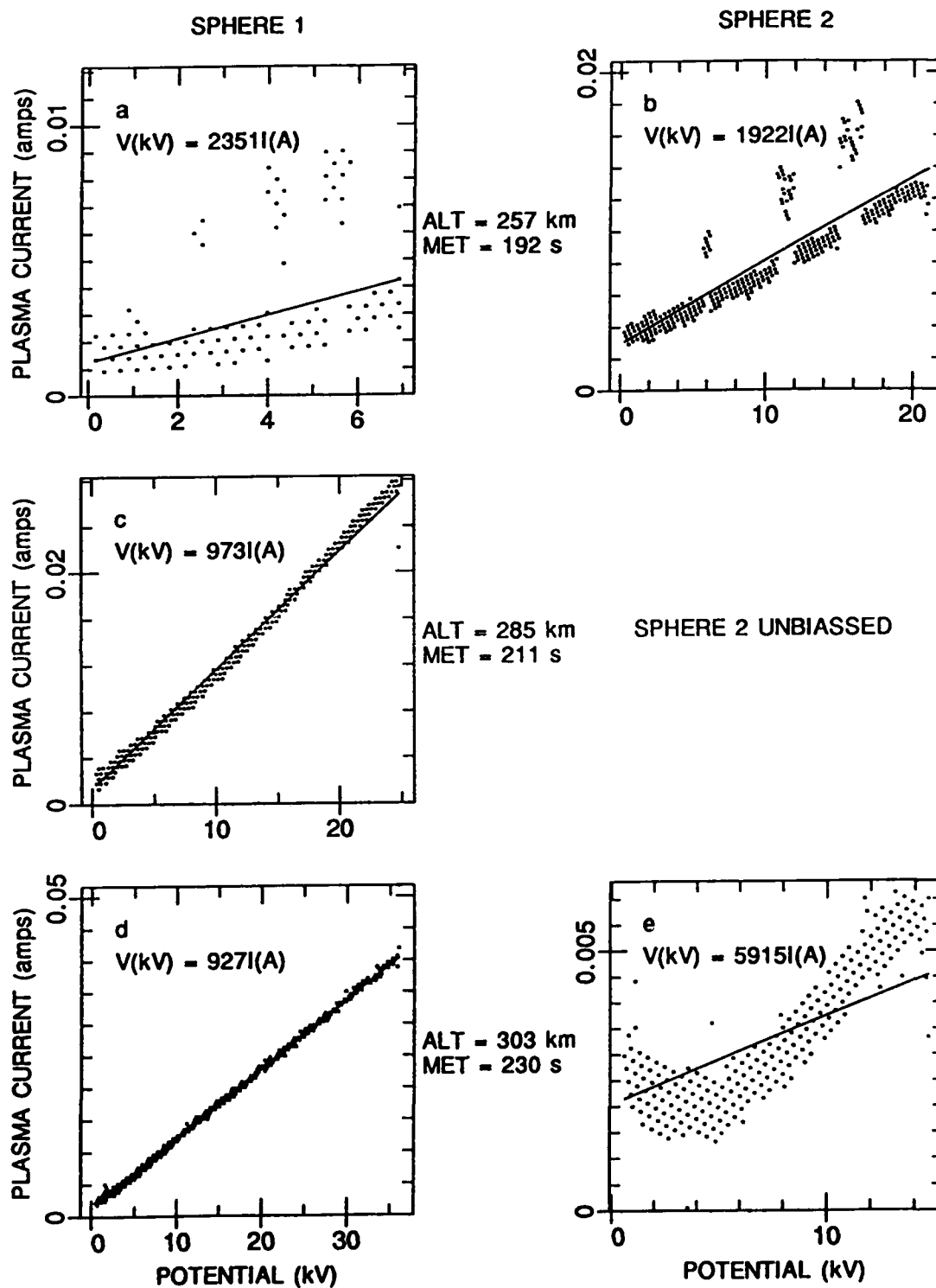
POTENTIAL (kV)

POTENTIAL (kV)

Fig. 5.8. Current-voltage plots for HV discharges 1(a and b), 2(c), and 3(d and e). Spheres are in the V-plane perpendicular orientation.
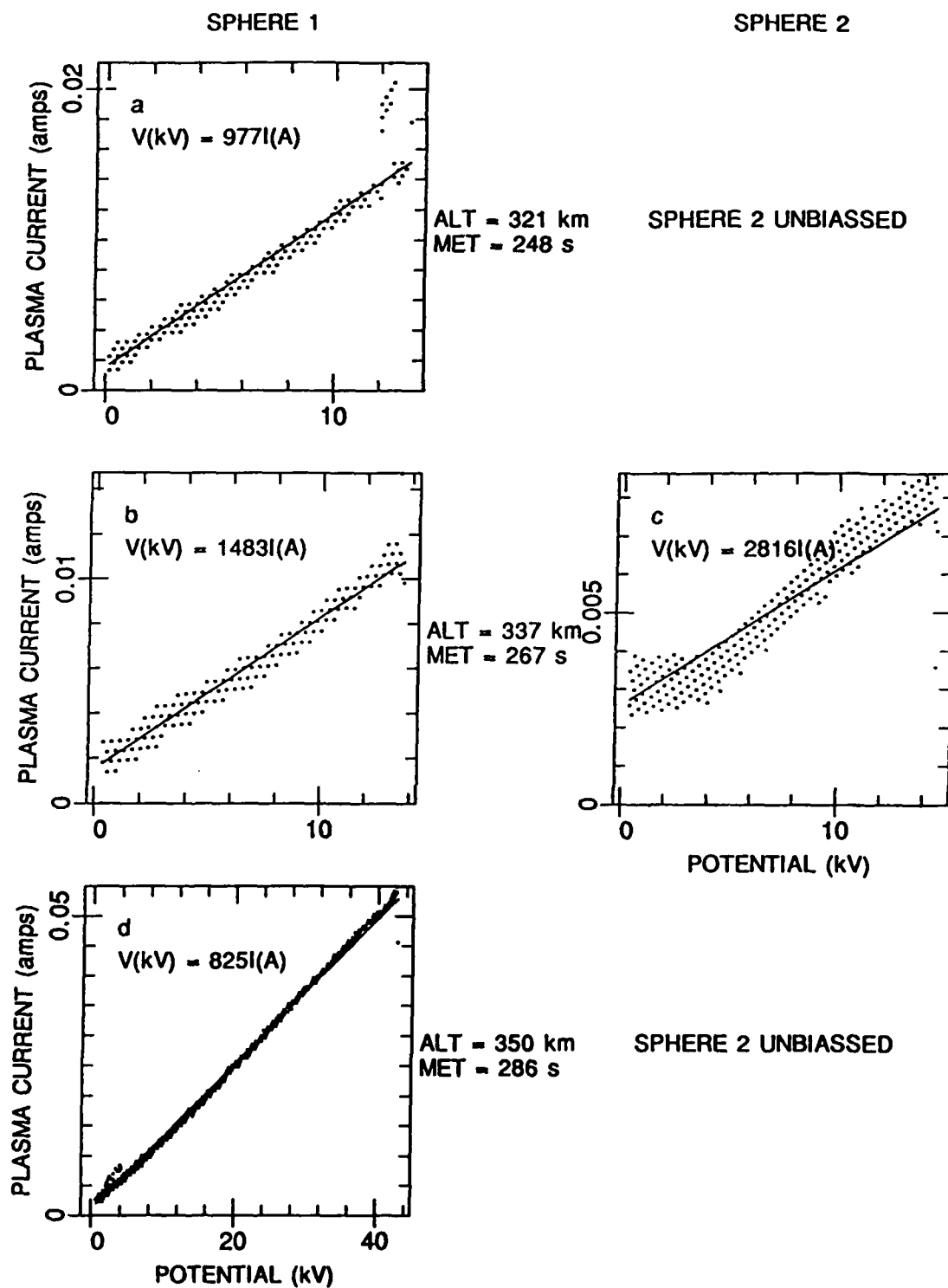
Fig. 5.9. Current - voltage plots for HV discharges 4(a), 5(b and c), and 6(c). Spheres are in the V-plane perpendicular orientation.
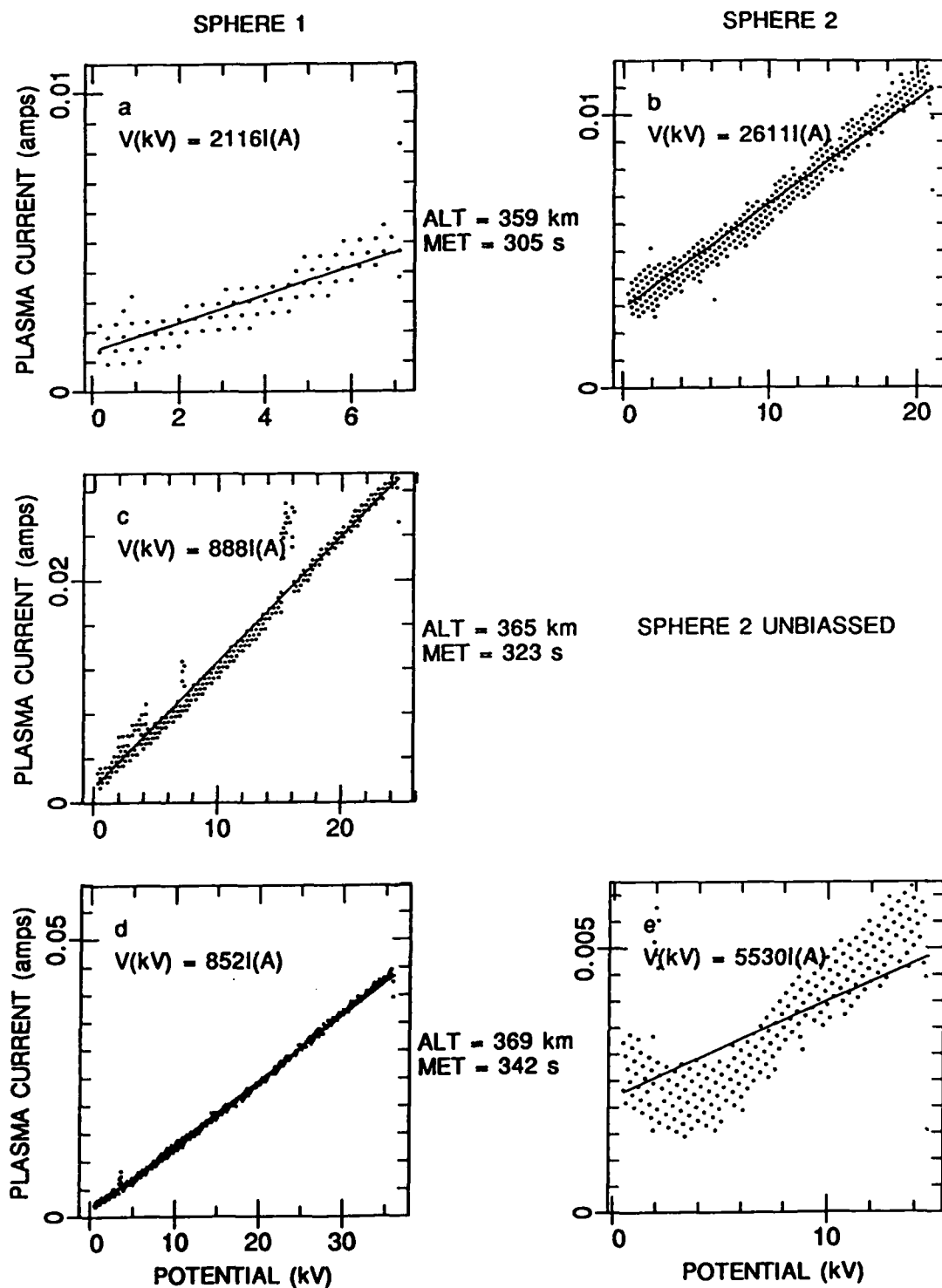
Fig. 5.10. Current - voltage plots for HV discharges 7(a and b), 8(c), and 9(d and e). Spheres are in the V-plane perpendicular orientation.

SPHERE 1                                    SPHERE 2

**a**
V(kV) = 937I(A)

ALT = 369 km     SPHERE 2 UNBIASSED
MET = 361 s

**b**
V(kV) = 1193I(A)

**c**
V(kV) = 3007I(A)

ALT = 366 km
MET = 380 s

POTENTIAL (kV)

**d**
V(kV) = 713I(A)

ALT = 361 km     SPHERE 2 UNBIASSED
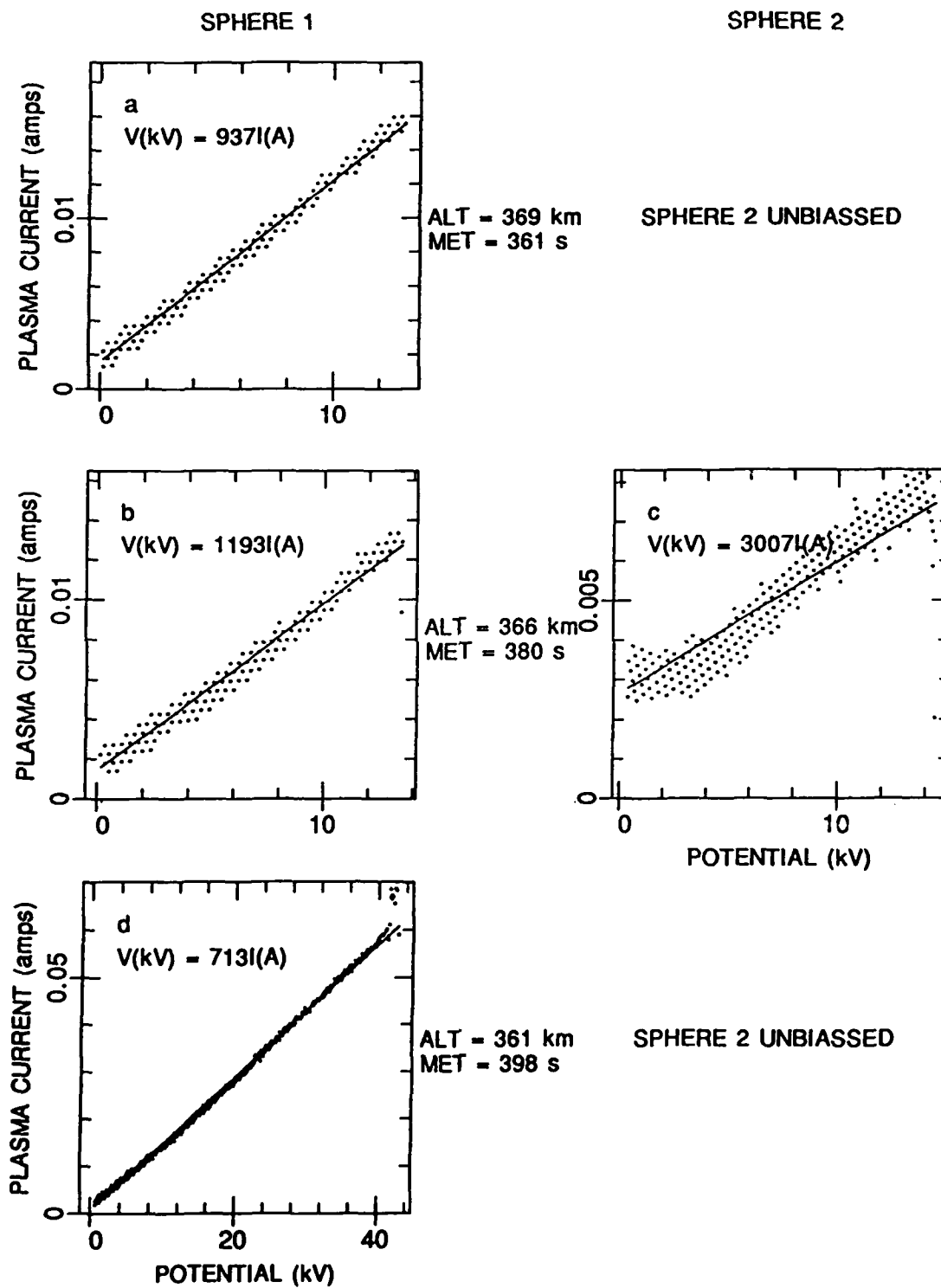MET = 398 s

POTENTIAL (kV)

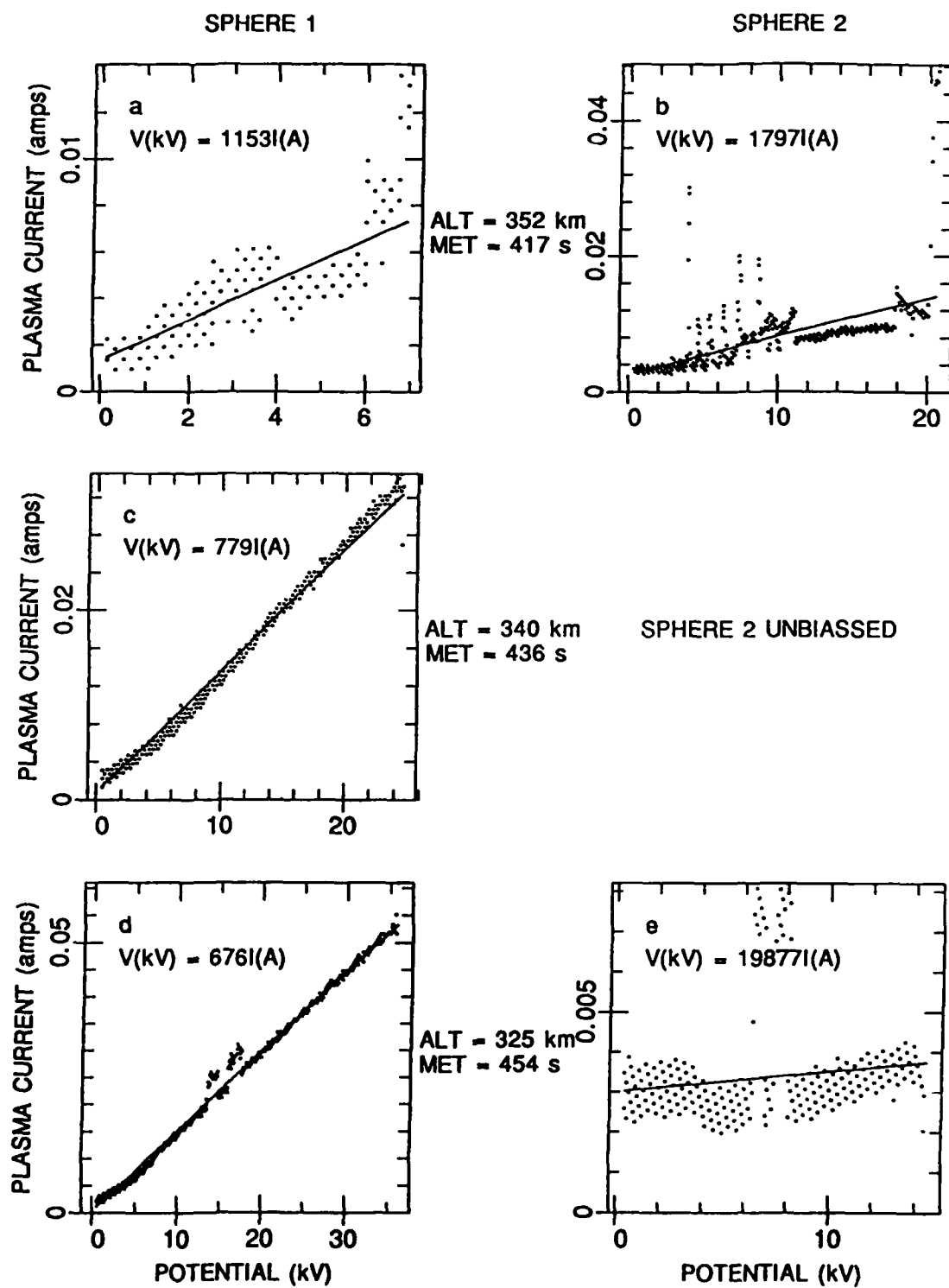Fig. 5.11. Current-voltage plots for HV discharges 10(a), 11(b and c), and 12(d). Spheres are in the V-plane perpendicular orientation.

Fig. 5.12. Current-voltage plots for HV discharges 13(a and b), 14(c), and 15(d and e). Spheres are in the V-plane parallel orientation.

SPHERE 1

SPHERE 2

a

V(kV) = 866I(A)

ALT = 307 km
MET = 473 s

SPHERE 2 UNBIASSED

b

V(kV) = 894I(A)

ALT = 287 km
MET = 492 s

c

V(kV) = 2317I(A)

POTENTIAL (kV)

d

V(kV) = 610I(A)

ALT = 263 km
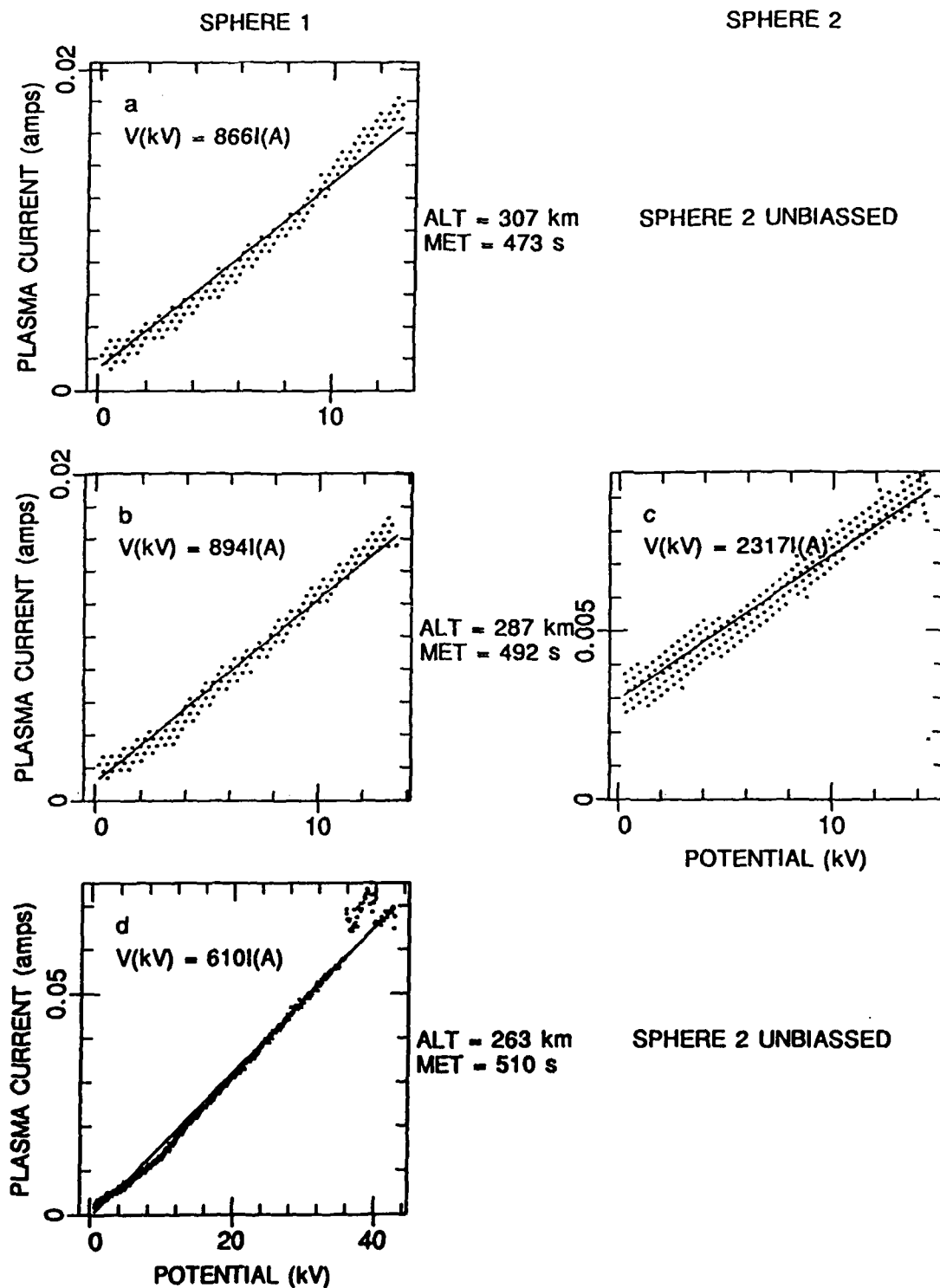MET = 510 s

SPHERE 2 UNBIASSED

POTENTIAL (kV)

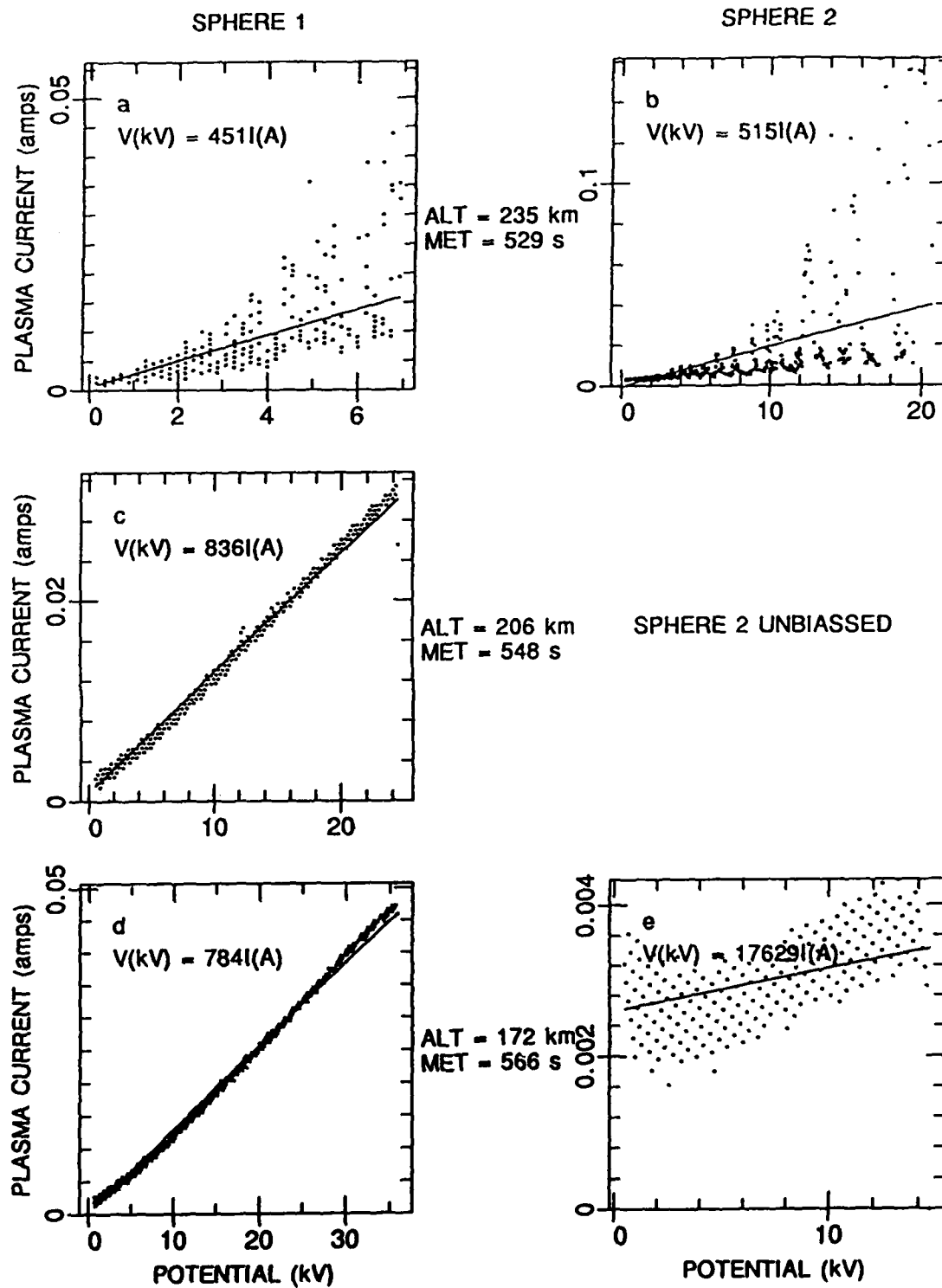Fig. 5.13. Current-voltage plots for HV discharges 16(a), 17(b and c), and 18(d). Spheres are in the V-plane parallel orientation.

Fig. 5.14. Current-voltage plots for HV discharges 19(a and b), 20(c), and 21(d and e). Sphere 1 boom is parallel to the magnetic field.

SPHERE 1                                          SPHERE 2

**a**

$V(kV) = 965I(A)$

PLASMA CURRENT (amps)

0.01

ALT = 137 km
MET = 585 s          SPHERE 2 UNBIASSED

0

0          10

**b**

$V(kV) = 1553I(A)$

PLASMA CURRENT (amps)

0.1

ALT = 98 km
MET = 604 s

0

0          0.5

**c**

0.2

0

0.2   0.4   0.6   0.8
POTENTIAL (kV)

**d**

$V(kV) = 299I(A)$

PLASMA CURRENT (amps)

0.1

ALT = 55 km
MET = 622 s          SPHERE 2 UNBIASSED
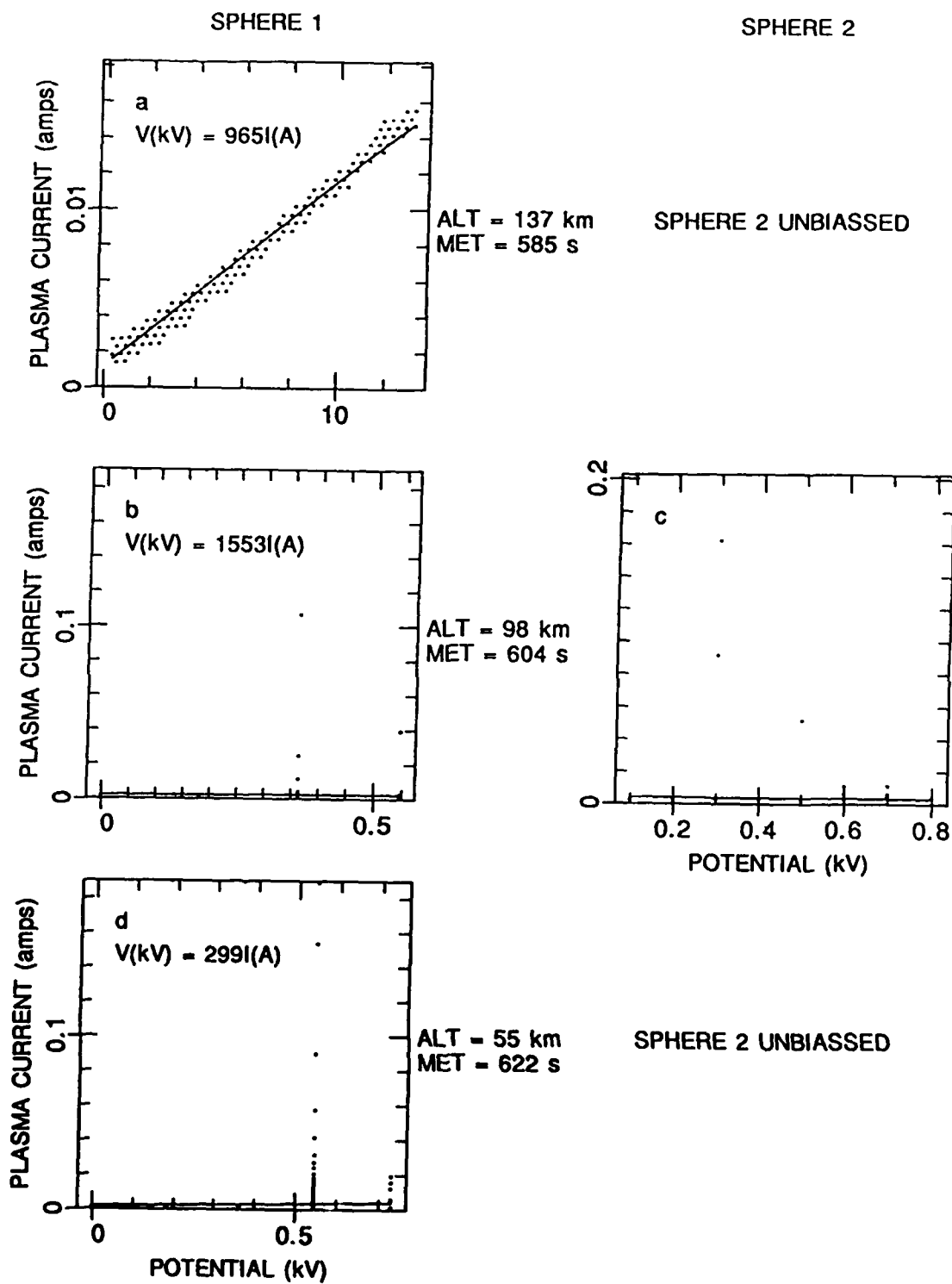
0

0          0.5
POTENTIAL (kV)

Fig. 5.15. Current-voltage plots for HV discharges 22(a), 23(b and c), and 24(d). Sphere 1 boom is parallel to the magnetic field.
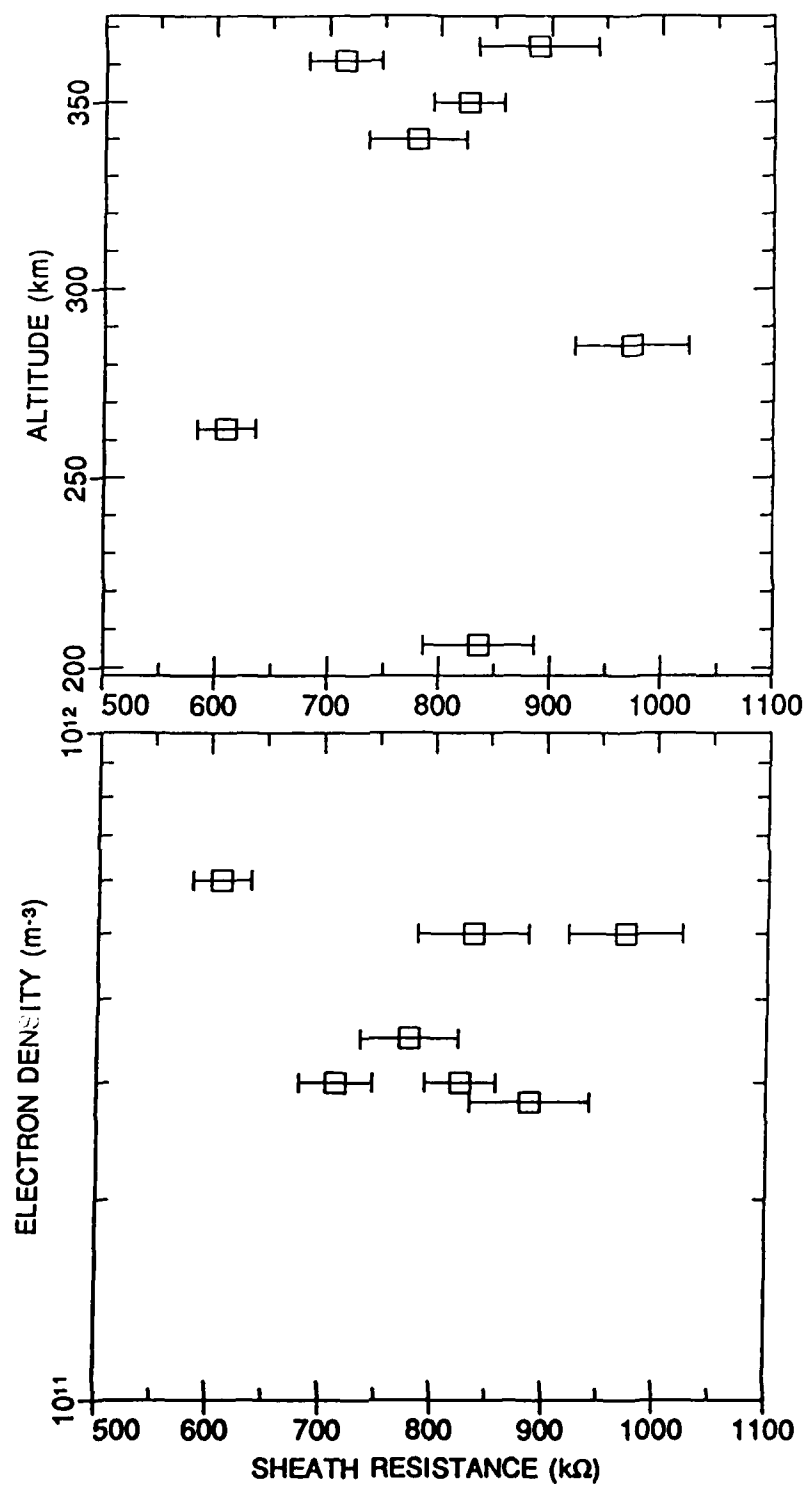
Fig. 5.16. Plot of SPEAR-1 total sheath resistance versus altitude (upper plot) and versus electron density (lower plot).
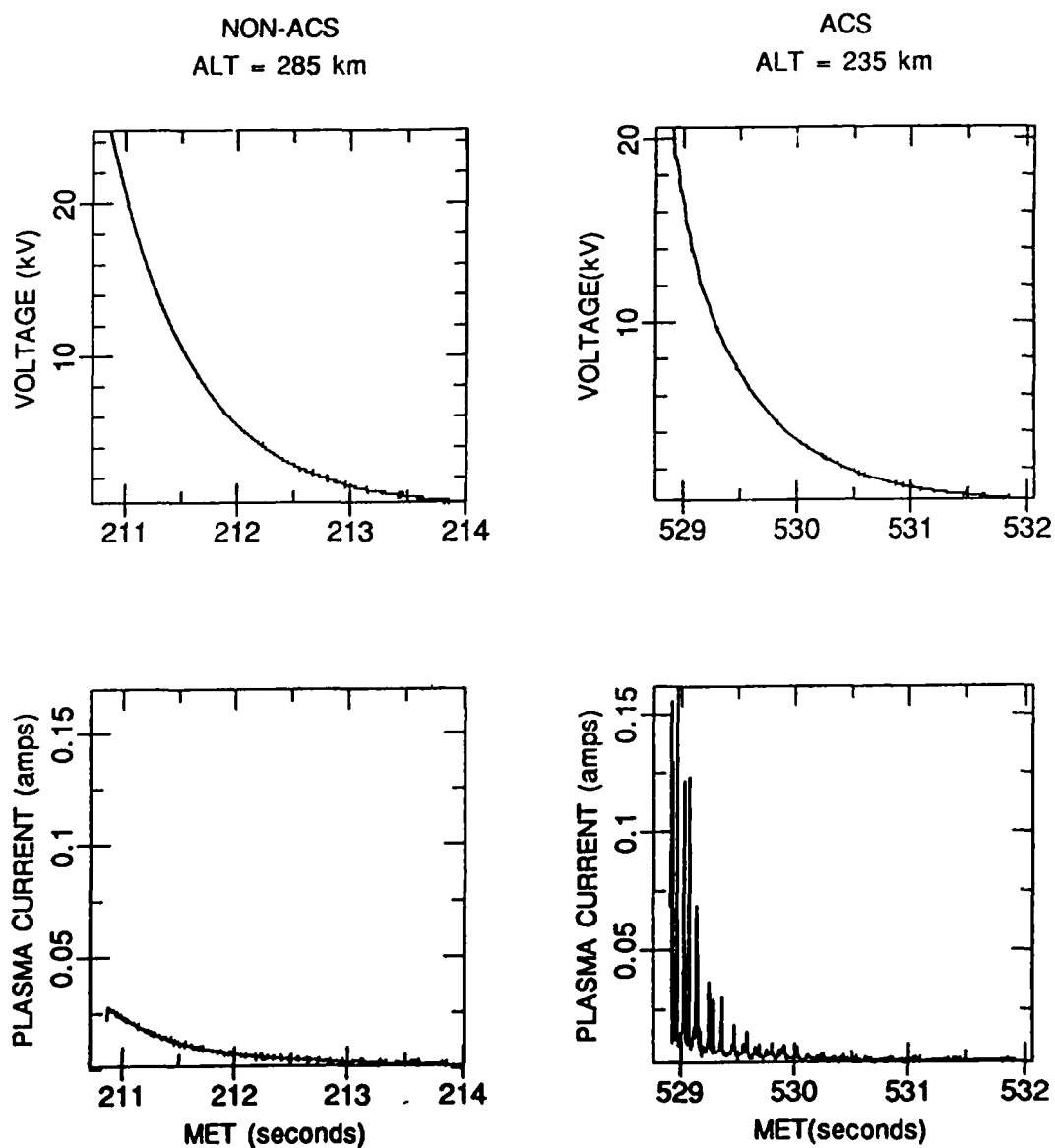
Fig. 5.17. Comparison of SPEAR-1 capacitor voltages and plasma currents for a non-ACS case and an ACS case. Non-ACS case is from discharge 2 and ACS case is from discharge 19.
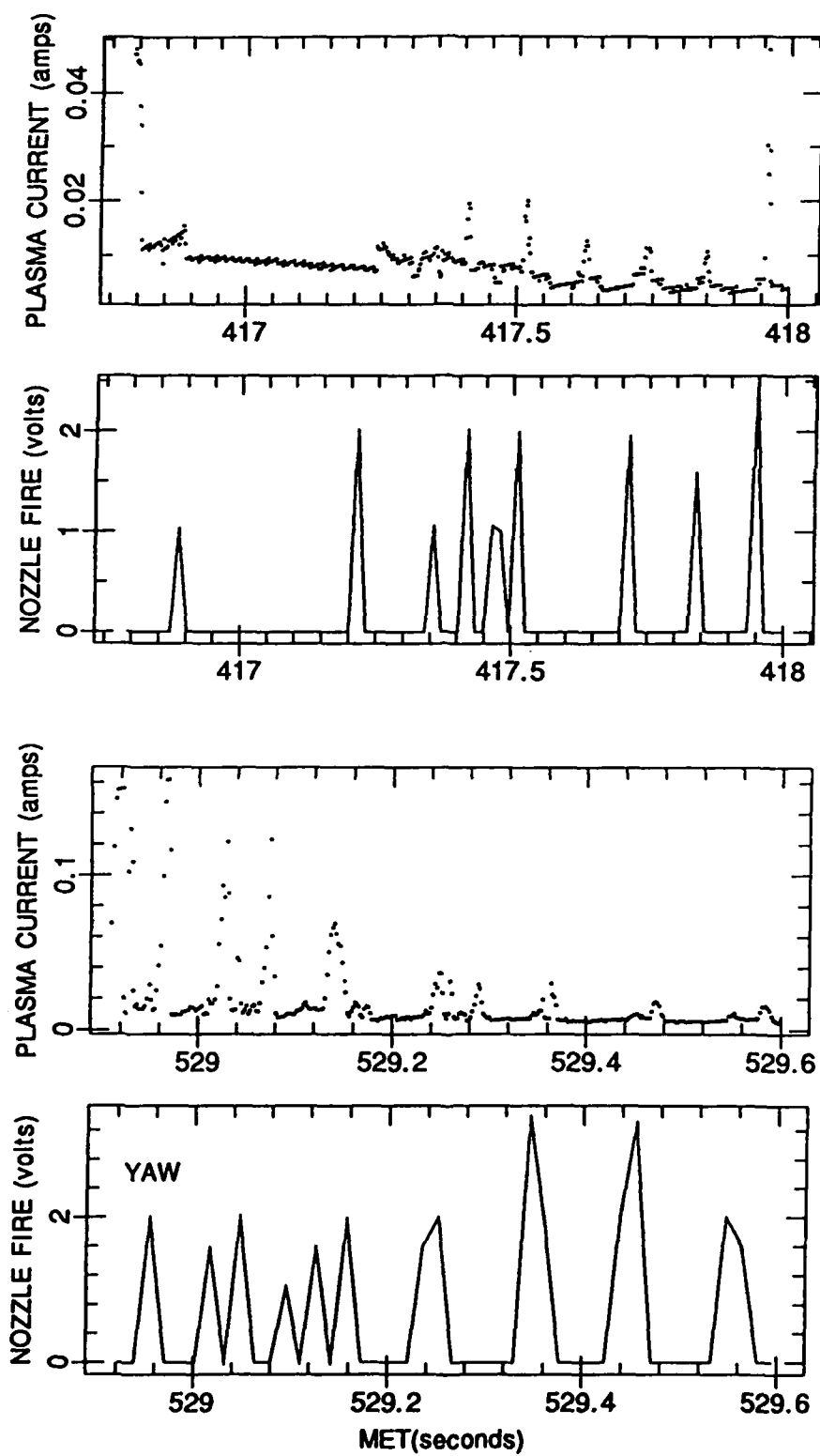
Fig. 5.18. Comparison between SPEAR-1 ACS activity and enhanced sphere currents. Upper plot is for discharge 13 and lower plot is for discharge 19.
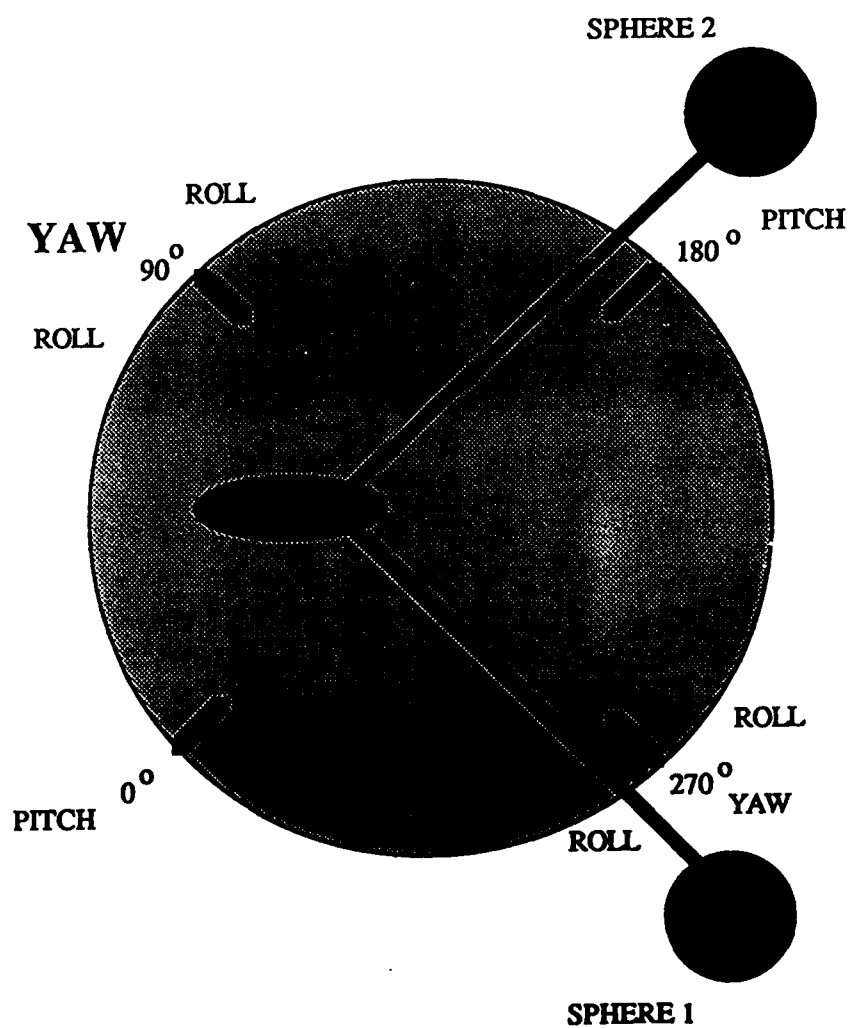
Fig. 5.19. Schematic SPEAR-1 cross section looking up the rocket body toward the spheres showing the orientation of the spheres with respect to the ACS jets.
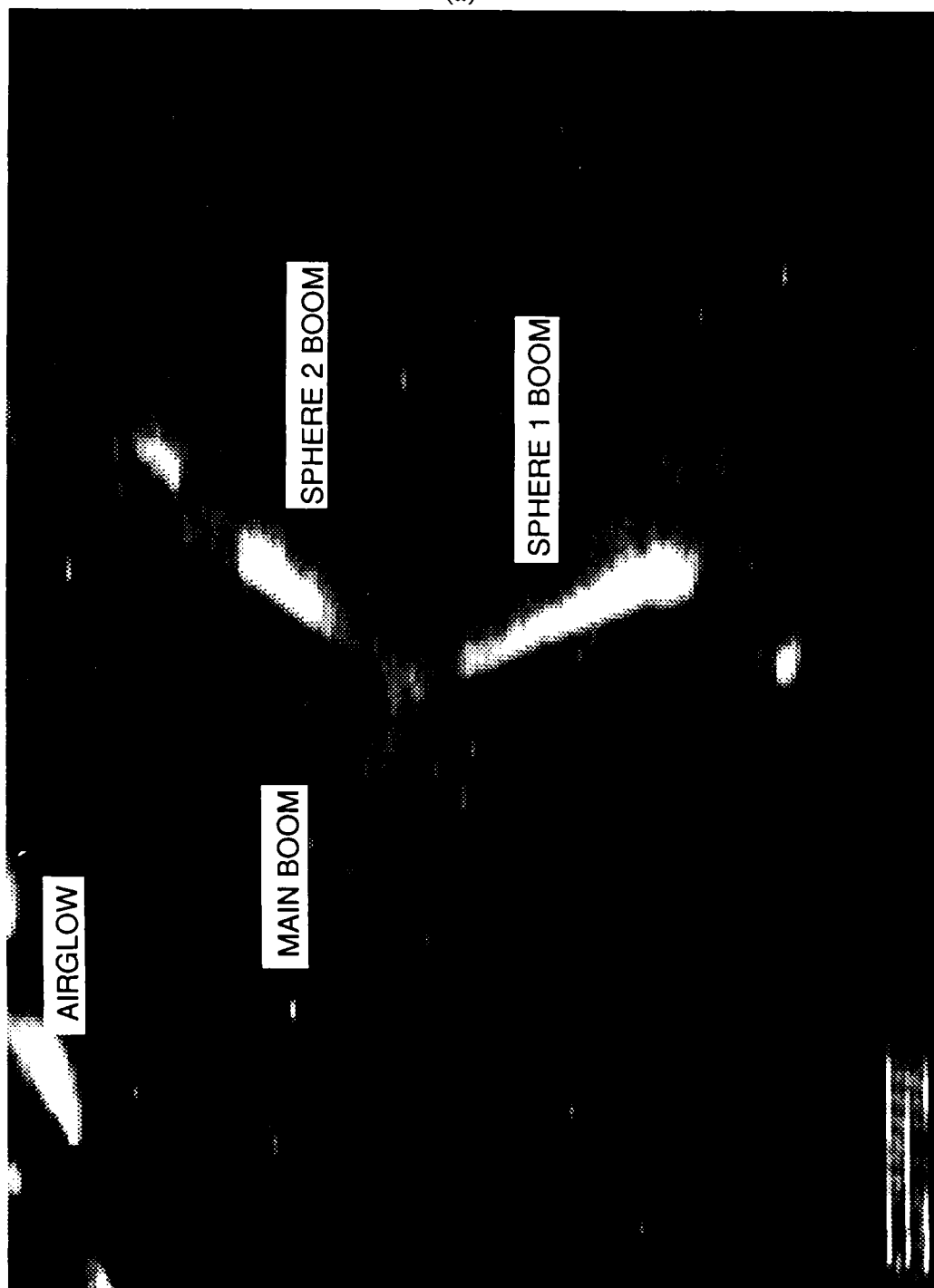
(a)



Fig 5.20. SPEAR-1 low light level TV picture (a) just prior to and (b) during the ACS gas release resulting in the 0.16 amp plasma current enhancement on discharge 19.

(b)



Fig. 5.20. Continued.

(a)
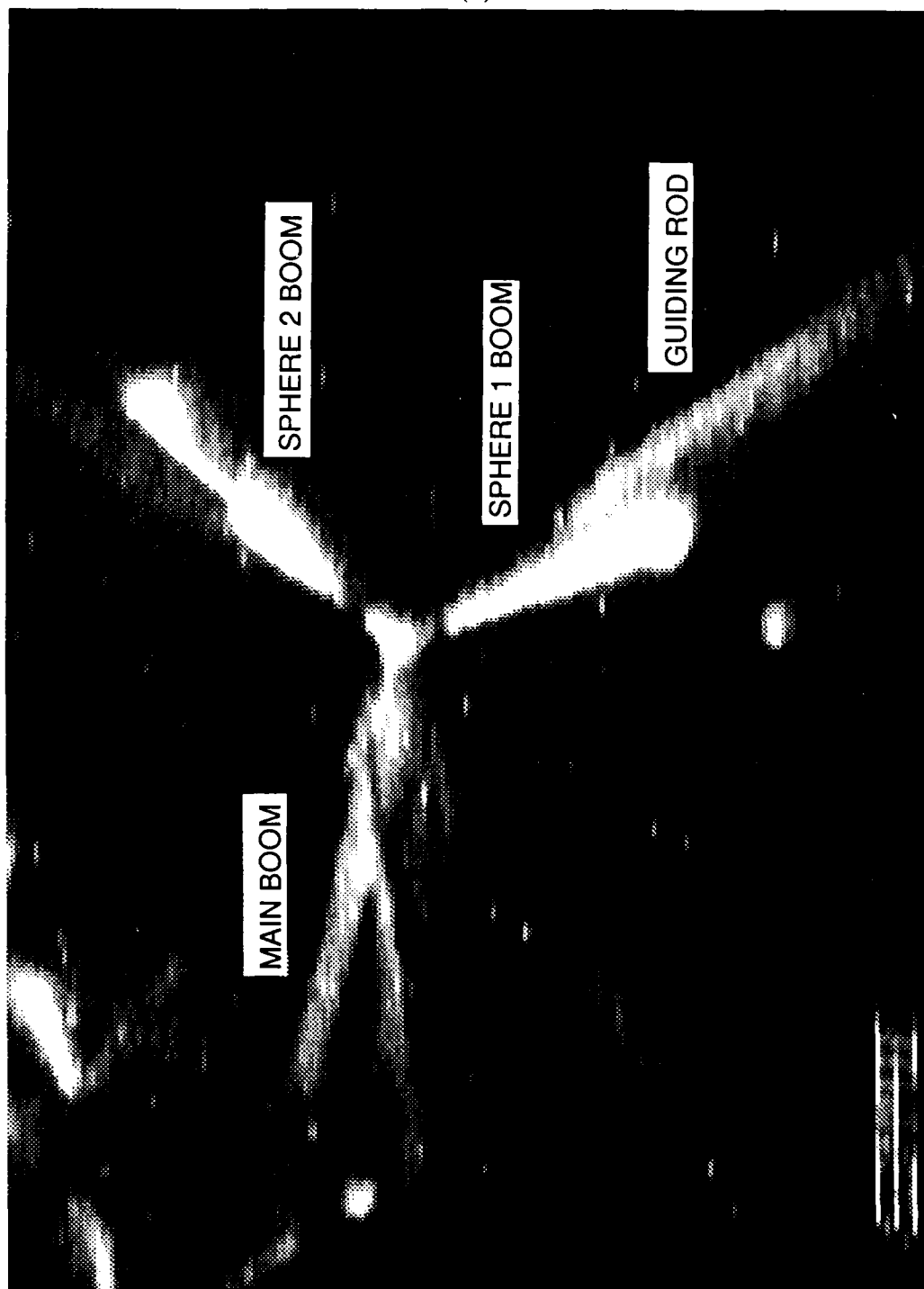


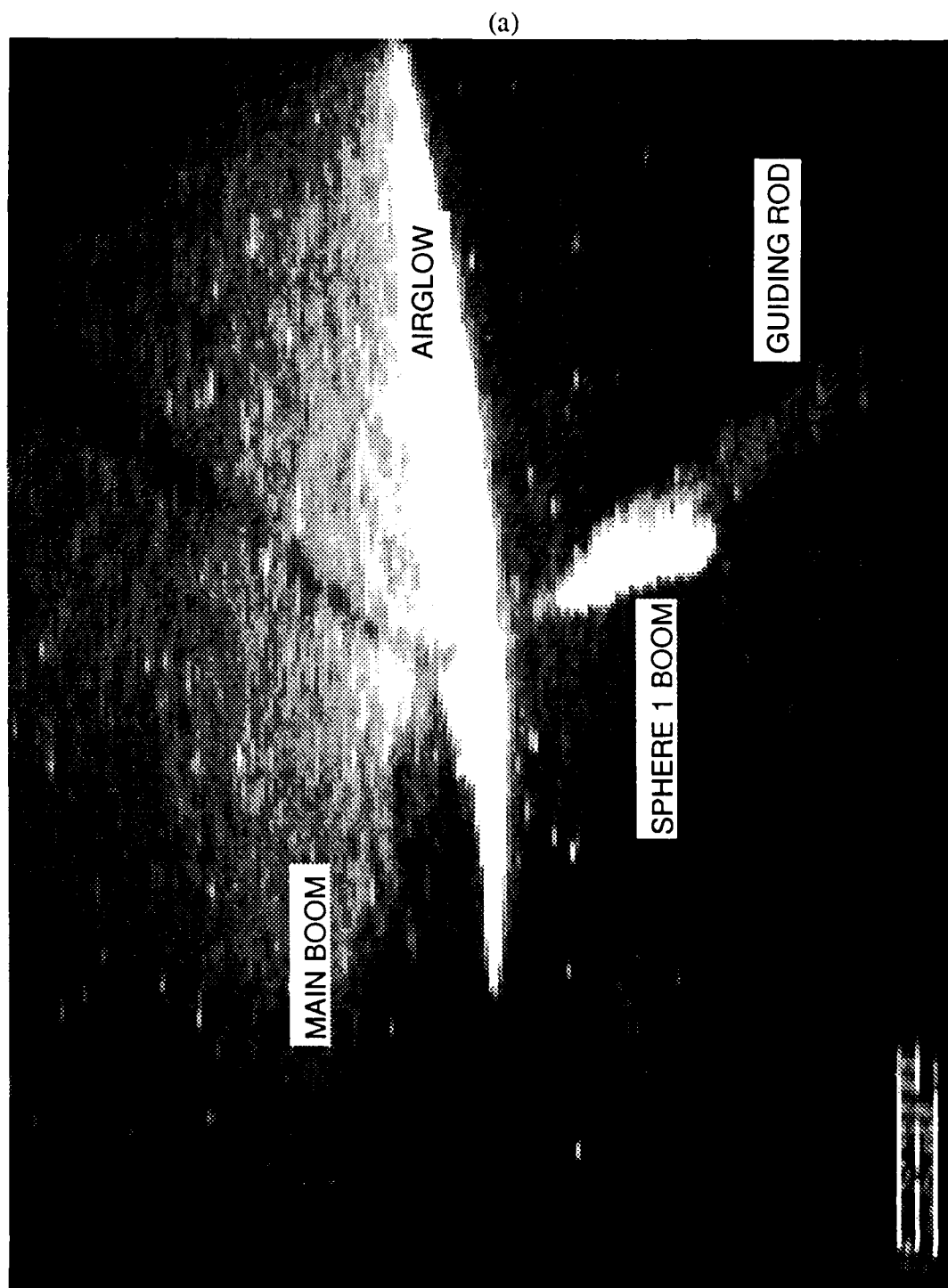Fig. 5.21. SPEAR-1 low light level TV picture during discharge 18 (a) just before the appearance of the glow indicating the start of a possible volume breakdown and (b) showing the glow near the connecting point between the main boom and the sphere booms indicating the start of a possible volume breakdown.

(b)
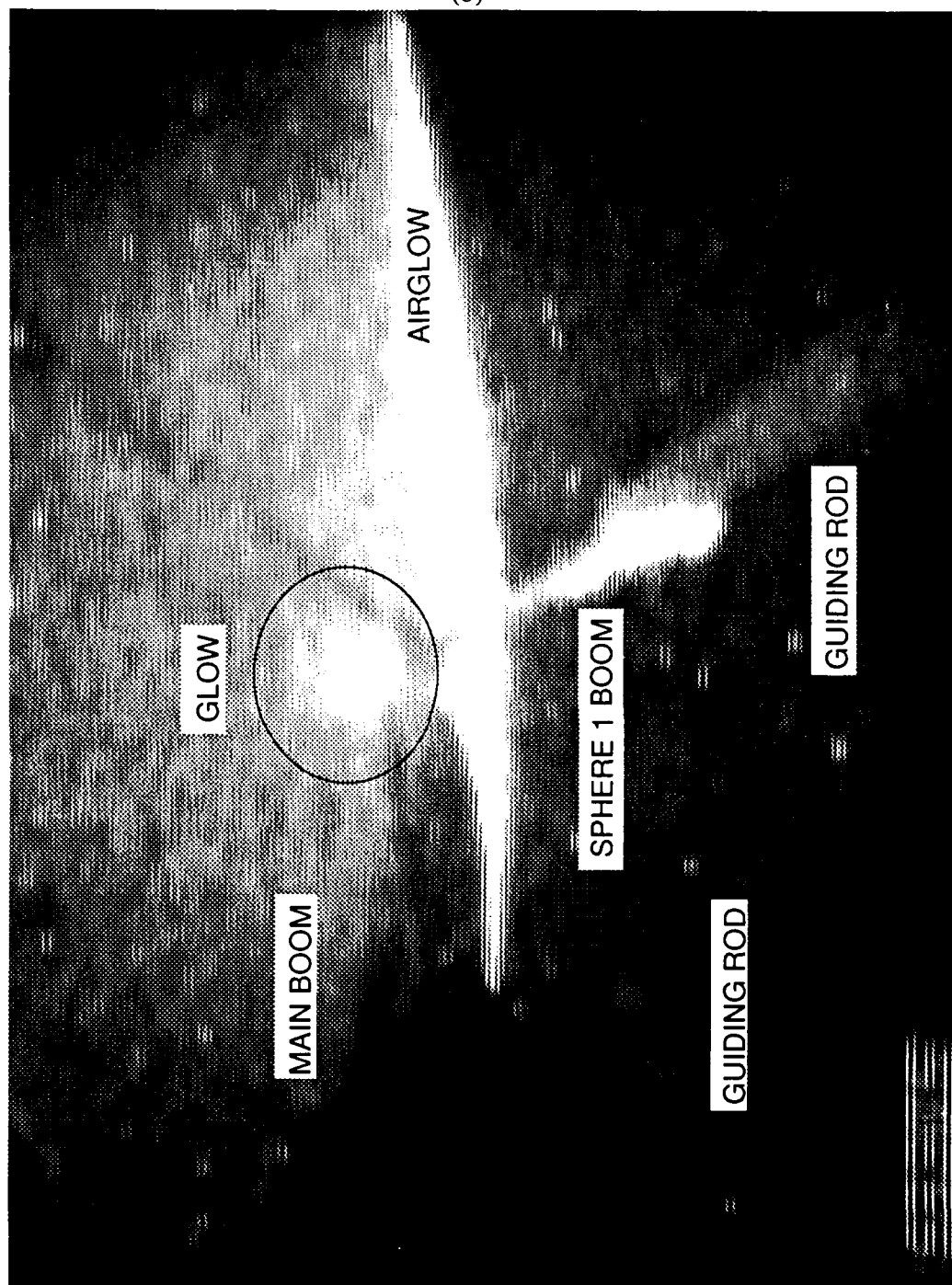


Fig. 5.21. Continued.
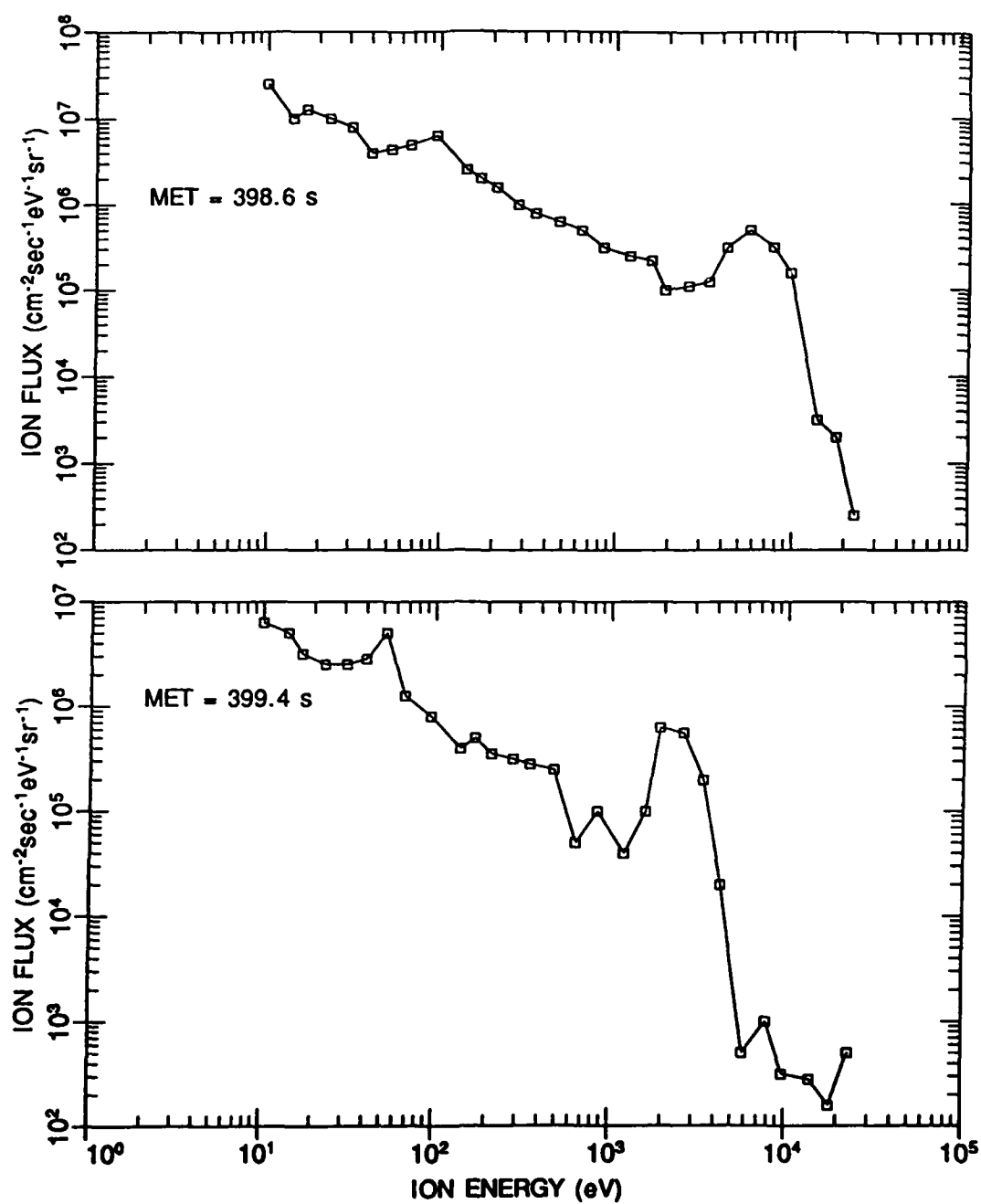
Fig. 5.22. Plot of ion energy versus ion flux for two times during discharge 12.
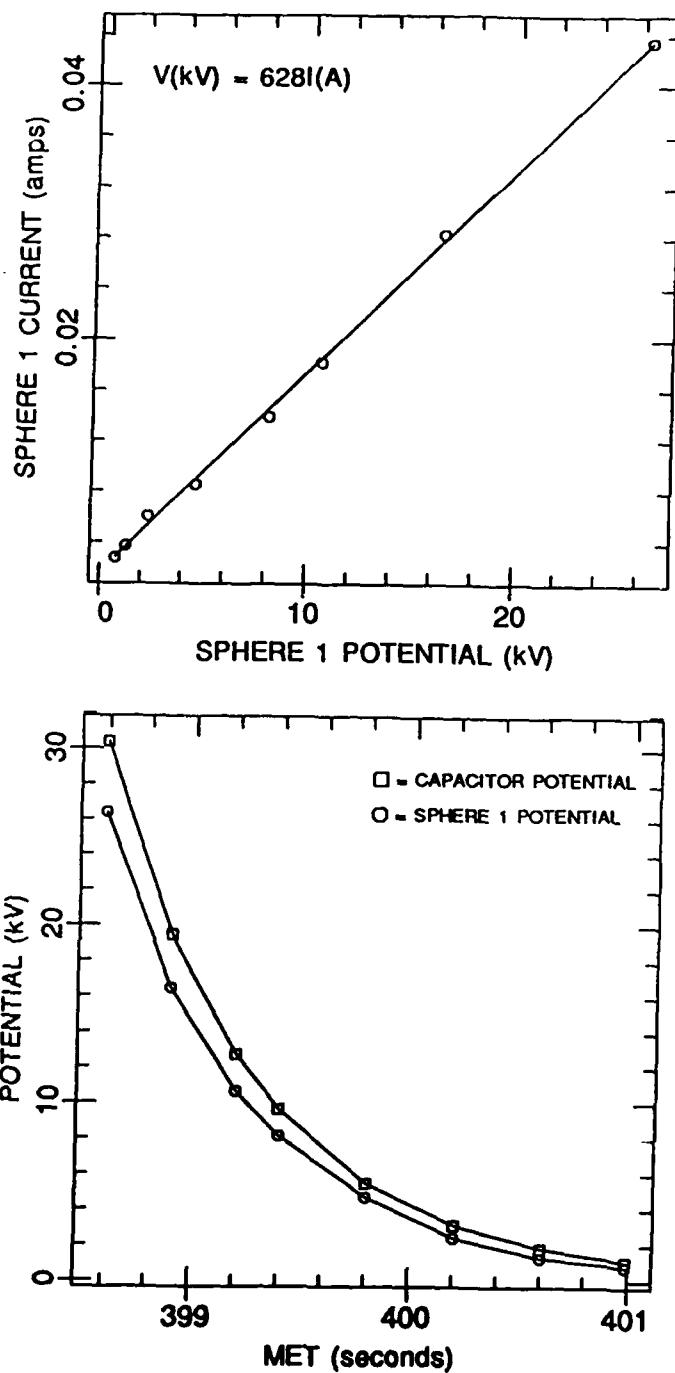
Fig. 5.23. Lower plot shows comparison between the capacitor potential and the calculated sphere potential for discharge 12. Upper plot shows the current-voltage plot for discharge 12 using the calculated sphere potential and sphere current.

T = 600°K

$N_e = 3 \times 10^{11}$ m$^{-3}$

PLASMA CURRENT (amps)

POTENTIAL (kV)
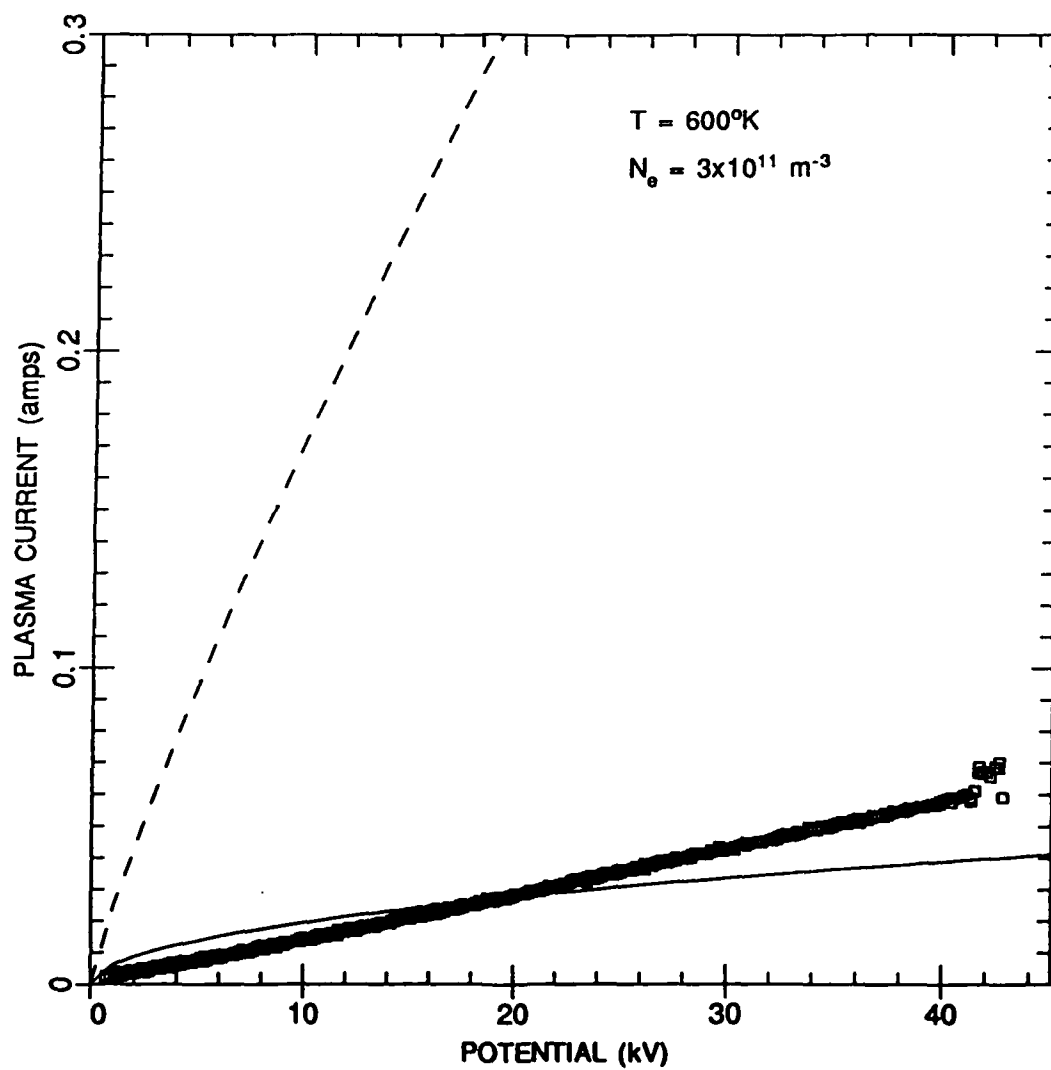
Fig. 5.24. Comparison of actual current-voltage data for discharge 12 with the Langmuir-Blodgett model (-----) and the Parker-Murphy model (———).
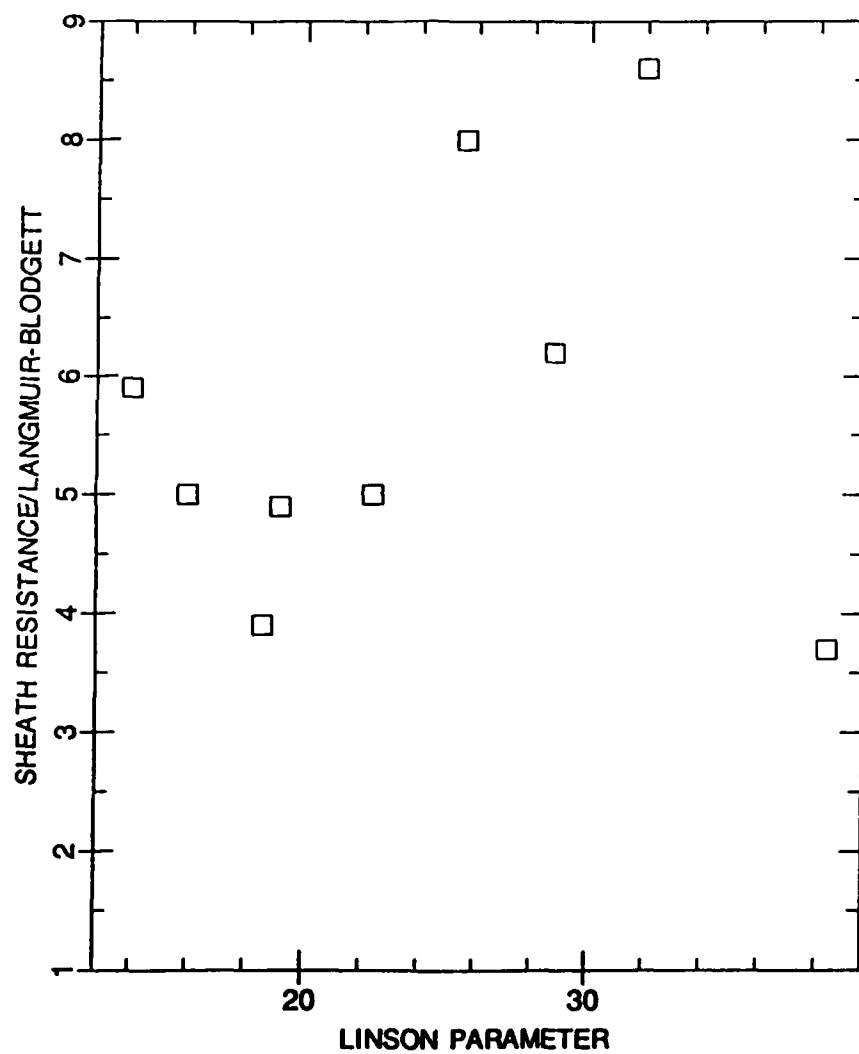
Fig. 5.25. Plot of the variation of the Linson parameter with the measured sheath resistance normalized by the calculated Langmuir-Blodgett sheath resistance for all single sphere biassing cases.
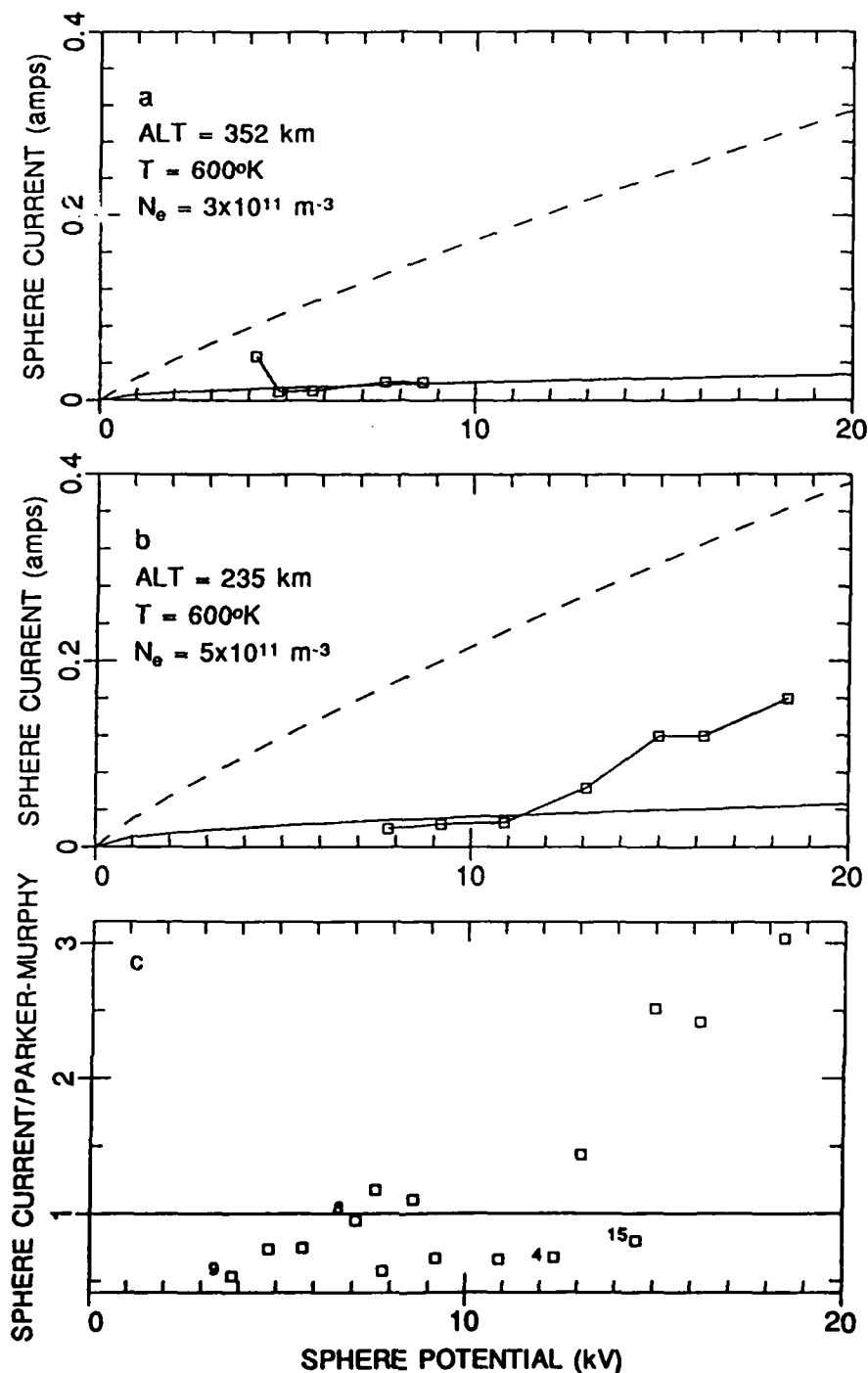
Fig. 5.26. Comparison of the ACS enhanced currents with the currents
predicted by the Parker-Murphy model. (a) compares the measured ACS
enhanced currents for discharge 13 with the Langmuir-Blodgett (-----) and
Parker-Murphy (———) models. (b) shows the same comparison for
discharge 19. (c) shows the comparison between sphere voltage and
sphere current normalized by the Parker-Murphy currents for all cases in
which ACS activity resulted in enhanced currents, including the single
enhancements for discharges 4, 8, 9, and 15.

# CHAPTER VI

## CONCLUSIONS

Several new results were found as a result of the data returned from SPEAR-1:

1. Potentials of up to 45 kV can be safely exposed to the LEO ionosphere with no significant local or volume breakdowns. However, the current-voltage characteristics for discharges 6, 12, and 18, coupled with data from the LLLTV, indicated that 45 kV may be an upper limit to the potentials that can be safely exposed to the LEO ionosphere.

2. Plasma currents collected by SPEAR-1 are space-charge-limited, and are very small when compared to any load currents which may be required.

3. ACS activity can drastically alter the current-voltage characteristics and result in current enhancements of up to 10 times over what would be collected if ACS activity was not occurring. The feasibility of using some type of gas release to act as a grounding mechanism for a high-voltage object was also demonstrated during the ACS gas releases.

4. There is a significant magnetic field dependence on the current-voltage characteristics for the complex SPEAR-1 sheath configuration. It was suggested that elongation of the total sphere charge sheath along magnetic field lines resulted in the reduced sheath resistances in the V-plane parallel orientation. However, the three dimensional shape of the spheres/rocket body charge sheaths is needed to determine precisely the reason for the reduced impedance in the V-plane parallel orientation.

5. Significant sheath interactions were seen. With the failure of the plasma contactor, there were up to three charge sheaths, rather than the expected two: the electron sheaths around both spheres, and a positive ion sheath around the rocket body. When the sphere 1 potential was greater than the sphere 2 potential, a possible decoupling of the sphere 2 charge sheath from the sphere 1 and rocket body charge sheaths was seen in the sphere 2 current-voltage plots below about 4000 volts. This decoupling was evidenced by a curvature in the otherwise linear plot indicating a slower decrease in the

current collected as voltage decreased. In one instance, the result was actually an increase in the current collected. The charge sheath coupling was evidenced by a sphere 2 sheath resistance of 1400 to 5000 k$\Omega$ larger than the sphere 1 resistance, indicating the sphere 1 and rocket body sheaths had partially encircled the sphere 2 sheath so that it was not as well exposed to the ionosphere. In the two cases where the sphere 2 potential was greater than the sphere 1 potential, the difference in the sheath resistances was only 400 to 500 k$\Omega$. Therefore, the three charge sheaths in this configuration were not as strongly coupled. During single sphere biassing, a pronounced curvature in the current-voltage plots was seen below about 10 kV. The curvature indicated a slower decrease in current collection as the potential decreased. This was the result of the decoupling of the sphere 1 and sphere 2/rocket body charge sheaths, allowing the sphere 1 sheath to be fully exposed to the ionosphere and collect the maximum amount of current possible.

6. In single sphere biassing operations up to 46 kV, both the NASCAP/LEO and POLAR models fairly accurately predicted the currents that would be collected by a high-voltage object with a complex charge sheath geometry such as SPEAR-1. These models also could accurately predict the negative charging of the rocket body due to the failure of the plasma contactor. The NASCAP/LEO model; however, appeared to have some problems in calculating the currents collected at the larger bias potentials due to an inability to adequately handle plasma turbulence. In general, both models appear to fairly accurately account for the physics involved in a complex system such as SPEAR-1.

7. Potentials up to several kilovolts negative could be exposed to the LEO environment with no adverse effects on the vehicle. This was the first time such high negative potentials had been exposed to the LEO environment.

8. There was no definitive altitude or plasma density dependence seen in the data. As expected, the lowest sheath resistances occurred near the peak electron density, but due to the limited range of plasma density over the SPEAR-1 altitude range, no definite trend could be seen in the data presented.

Suggestions for Future Research

Even though SPEAR-1 answered many questions about the interactions of high voltage conductors with the LEO ionosphere, the flight raised some new possibilities for future work:

1. Although no volume breakdown was seen for the potentials used, the possible beginnings of a volume breakdown was observed. Can potentials of more than 45 kV be exposed to the LEO environment without a volume breakdown? If not, what is the maximum possible potential that can be used?

2. If a neutral gas release can be used as a grounding mechanism, what is the minimum potential necessary for this gas release to act as a plasma contactor?

3. More results from numerical modelling should be studied to determine the exact three dimensional shape of the very complex SPEAR-1 charge sheaths. Since many of the results presented are critically dependent on the shape of the charge sheath, this work must be done to determine exactly what is happening in the interactions between the vehicle and the environment.

4. What would be the current-voltage characteristics if the rocket body potential was clamped at, or near, the ambient potential for the entire high-voltage discharge? Preliminary results from the ACS gas releases show that the Parker-Murphy model is an accurate predictor at potentials less than about 12 to 15 kV and the Linson model is a better predictor at higher potentials. Would this be the case if the rocket body potential is clamped through the entire discharge? If not, then why is it true for individual ACS gas releases? If so, then at what potential does the crossover from the Parker-Murphy model to the Linson model occur?

5. How will these results change during a period of significant solar activity? It is well known the LEO environment changes significantly during solar activity, but we must know if these same results will be obtained during times of high solar activity.

With man moving more and more into the LEO environment and planning large structures which will utilize high voltages, the interactions between these structures and the environment must be understood.  SPEAR-1 has provided a good start to such an understanding.

# REFERENCES

Banks, P. M. and G. Kockarts, Aeronomy (Parts A and B), 785 pp, Academic Press, New York, 1973.

Bauer, S. J., Physics of Planetary Ionospheres, 230 pp, Springer-Verlag, New York, 1973.

Beard, D. B. and F. S. Johnson, Charge and magnetic field interaction with satellites, J. Geophys. Res., 65, 1-7, 1960.

Beard, D. B., and F. S. Johnson, Ionospheric limitations on attainable satellite potential, J. Geophys. Res., 66, 4113-4122, 1961.

Bunshah, R. F., The history of electron beam technology, in Introduction to Electron Beam Technology, edited by R. Bakish, pp 1-20, John Wiley and Sons, New York, 1962.

Cauffman, D. P. and N. C. Maynard, Model of the effect of the satellite photosheath on a double floating probe system, J. Geophys. Res., 79, 2427-2438, 1974.

Coffey, H. E., Geomagnetic and solar data, J. Geophys. Res., 93, pp 1028, 2016, and 2768, 1988.

DeForest, S. E., Spacecraft charging at synchronous orbit, J. Geophys. Res., 77, 651-659, 1972.

Dietz, L. A. and J. C. Sheffield, Secondary electron emission induced by 5-30 keV monatomic ions striking thin oxide films, J. Appl. Phys., 46, 4361-4370, 1975.

Dunbar, W. G., Large space systems technology electronics-data and power distribution, in Large Space Systems Technology-1979, NASA CP-2118, pp 423-442, 1980.

Feuerbacher B. and B. Fitton, Experimental investigation of photoemission from satellite surface materials, J. Appl. Phys., 43, 1563-1572, 1972.

Finke, R. C., I. T. Myers, F. F. Terdan, and N. J. Stevens, Power management and control for space systems, in Future Orbital Power Systems Technology Requirements, NASA CP-2058, pp 195-207, 1978.

Garrett, H. B., Spacecraft charging: a review, Prog. Astronaut. Aeronaut., 71, 167-226, 1980.

Gussenhoven, M. S. and E. G. Mullen, Geosynchronous environment for severe spacecraft charging, J. Space. Rockets, 20, 26-31, 1983.

Halliday, D., and R. Resnick, Fundamentals of Physics, 827 pp, John Wiley and Sons, New York, 1974.

Hedin, A. E., MSIS-86 thermospheric model, J. Geophys. Res., 92, 4649-4662, 1987.

Hok, G., H. S. Sicinski, and N. W. Spencer, Temperature and electron density measurements in the ionosphere by a Langmuir probe, in Scientific Uses of Earth Satellites, edited by J. A. Van Allen, pp 263-267, Univ. of Michigan Press, Ann Arbor, 1956.

Katz, I., J. J. Cassidy, M. J. Mandel, G. W. Schnuelle, P. G. Steen, and J. C. Roche, The capabilities of the NASA charging analyzer program, in Spacecraft Charging Technology-1978, NASA CP-2071, AFGL-TR-79-0082, pp 101-108, 1979.

Katz, I., M. J. Mandell, G. W. Schnuelle, D. E. Parks, and P. G. Steen, Plasma collection by high voltage spacecraft at low earth orbit, J. Space. Rockets, 18, 79-82, 1981.

Katz, I. and D. L. Cooke, Preliminary documentation for the POLAR code, AFGL-TR-83-0194, 256pp, Air Force Geophys. Lab., Bedford, Mass., 1984.

Katz, I., G. A. Jongward, V. A. Davis, M. J. Mandell, R. A. Kuharski, J. R. Lilley, Jr., W. J. Raitt, D. L. Cooke, R. B. Torbet, G. Larson, and D. Rau, Structure of the bipolar plasma sheath generated by SPEAR-1, J. Geophys. Res., 94, 1450-1458, 1989.

Kawashima, N., S. Sasaki, K. Oyama, K. Akai, and Y. Nakai, Floating potential and return current measurements in a rocket-borne electron beam experiment, Geophys. Res. Lett., 9, 1061-1063, 1982.

Knott, K., The equilibrium potential of a magnetospheric satellite in an eclipse situation, Planet. Space Sci., 20, 1137-1146, 1972.

Laframboise, J. G. and L. W. Parker, Spacecraft charging in the auroral plasma: progress toward understanding the physical effects involved, in The Aerospace Environment at High Altitudes and its Implications for Spacecraft Charging and Communications, AGARD Conference Proceedings #406, pp 13.1-13.10, 1987.

Langmuir, I., The effect of space charge and residual gases on thermionic currents in high vacuum, Phys. Rev., 2, 450-486, 1913.

Langmuir, I. and K. Blodgett, Currents limited by space charge between coaxial cylinders, Phys. Rev., 22, 347-356, 1923.

Langmuir, I., and K. Blodgett, Currents limited by space charge between concentric spheres, Phys. Rev., 23, 49-59, 1924.

Leonard, L. H., Electron gun design, in Introduction to Electron Beam Technology, edited by R. Bakish, pp 70-95, John Wiley and Sons, New York, 1962.

Linson, L. M., Current-voltage characteristics of an electron-emitting satellite in the ionosphere, J. Geophys. Res., 74, 2368-2375, 1969.

McPherson, D. A., and W. R. Schober, Spacecraft charging at high altitudes: the SCATHA satellite program, Prog. Astronaut. Aeronaut., 47, 15-30, 1976.

Montgomery, M. D., J. R. Asbridge, S. J. Bane, and E. W. Hones, Jr., Low energy measurements and spacecraft potential: Vela 5 and Vela 6, in Photon and Particle Interactions with Surfaces in Space, D. Reidel, Dordrecht, Holland, 1973.

Mott-Smith, H. M., and I. Langmuir, The theory of collectors in gaseous discharges, Phys. Rev., 28, 727-763, 1926.

Mullen, E. G., M. S. Gussenhoven, D. A. Hardy, T. A. Aggson, and B. G. Ledley, SCATHA survey of high-level spacecraft charging in sunlight, J. Geophys. Res., 91, 1474-1490, 1986.

Olsen, R. C., Modification of spacecraft potentials by thermal electron emission on ATS-5, J. Space. Rockets, 18, 527-532, 1981.

Olsen, R. C., A threshold effect for spacecraft charging, J. Geophys. Res., 88, 493-503, 1983.

Olsen, R. C., Experiments in charge control at geosynchronous orbit - ATS-5 and ATS-6, J. Space. Rockets, 22, 254-264, 1985.

Olsen, R. C. and C. K. Purvis, Observations of charging dynamics, J. Geophys. Res., 88, 5657-5667, 1983.

Parker, L. W. and B. L. Murphy, Potential buildup on an electron emitting ionospheric satellite, J. Geophys. Res., 72, 1631-1636, 1967.

Parks, D. E. and I. Katz, Charging of a large object in low earth polar orbit, in Spacecraft Charging Technology-1980, NASA-CP-2182, AFGL-TR-81-0270, pp 979-986, 1981.

Purvis, C. K. and R. O. Bartlett, Active control of spacecraft charging, Prog. Astronaut. Aeronaut., 71, 299-317, 1980.

Raitt, W. J., SPEAR-1: Space Power Experiments Aboard Rockets, Final Report to the Defense Nuclear Agency, Utah State University, Center for Atmospheric and Space Sciences, 95pp., 1988.

Raitt, W. J., J. V. Eccles, N. B. Myers, D. C. Thompson, P. M. Banks, P. R. Williamson, R. I. Bush, J. Hawkins, S. Sasaki, K. I. Oyama, N. Kawashima, and W. F. Sharp, Active vehicle charging measurements in sounding rocket and space shuttle orbiter environments at low earth (LEO) altitude, in The Aerospace Environment at High Altitudes and its Implications for Spacecraft Charging and Communications, AGARD Conference Proceedings #406, pp 9.1-9.16, 1987.

Rawer, K., S. Ramakrishnan, and D. Bilitza, International reference ionosphere 1978, U.R.S.I. Brussels and World Data Center, Report UAG-82, Boulder, Colo., 1981.

Reagan, J. B., R. W. Nightingale, E. E. Gaines, R. E. Meyerott, and W. L. Imhof, Role of energetic particles in charging/discharging of spacecraft dielectrics, in Spacecraft Charging Technology-1980, NASA-CP-2182, AFGL-TR-81-0270, pp 74-82, 1981.

Redhead, P. A., The magnetron gauge: a cold cathode vacuum gauge, Canadian J. Phys., 37, 1260-1271, 1959.

Richmond, A. D., Thermospheric dynamics and electrodynamics, in Solar-Terrestrial Physics, edited by R. L. Carovillano and J. M. Forbes, pp 523-607, D. Reidel, Dordrecht, Holland, 1982.

Roche, J. C., and C. K. Purvis, Comparison of NASCAP predictions with experimental data, in Spacecraft Charging Technology, 1978, NASA CP-2071, AFGL-TR-79-0082, 144-151, 1979.

Sasaki, S., K. I. Oyama, N. Kawashima, Y. Watanabe, T. Obayashi, W. J. Raitt, A. B. White, P. M. Banks, P. R. Williamson, W. F. Sharp, T. Yokota, and K. Hirao, Results from a series of tethered rocket experiments, J. Space. Rockets, 24, 444-453, 1987.

Thiemann, I., R. W. Schunk, N. Singh, R. Grard, GIOTTO spacecraft charging due to impact generated plasma in the presence of dielectric materials, in The Aerospace Environment at High Altitudes and its Implications for Spacecraft Charging and Communications, AGARD Conference Proceedings #406, pp 11.1-11.7, 1987.

Whipple, E. C., Observation of photoelectrons and secondary electrons reflected from a potential barrier in the vicinity of ATS-6, J. Geophys. Res., 81, 715-719, 1976.

Whipple, E. C., Potential of surfaces in space, Rep. Prog. Phys., 44, 74-1250, 1981.

Winckler, J. R., The application of artificial electron beams to magnetospheric research, Rev. Geophys. Space Phys., 18, 659-682, 1980.